Defects Mechanics using Computational Dislocation Dynamics by Level Set Method

August, 2012

Jun Pan

Department of Precision Science & Technology and Applied Physics

OSAKA UNIVERSITY

Defects Mechanics using Computational Dislocation Dynamics by Level Set Method

August, 2012

Jun Pan

Department of Precision Science & Technology and Applied Physics

OSAKA UNIVERSITY

Contents

Chapter 1

Introduction

1.1 Introduction to Dislocation

The conception of dislocation appearing as an abstract mathematical concept was first given by an Italian mathematician named Volterra in the late 19th century when he examined properties of singularities produced by cutting and shifting matter in a continuous solid [1]. However, this conception remained unnoticed until three scientists, Taylor, Polanyi and Orowan in 1930s, independently proposed dislocations as the defects in crystalline material which may be responsible for a crystal's ability to deform plasticity [3-4]. Then under the observations from transmission electron microscopy (TEM), the numerous aspects of dislocations for crystal plasticity and the other defect behaviors have been confirmed [5] (see Fig. 1.1).

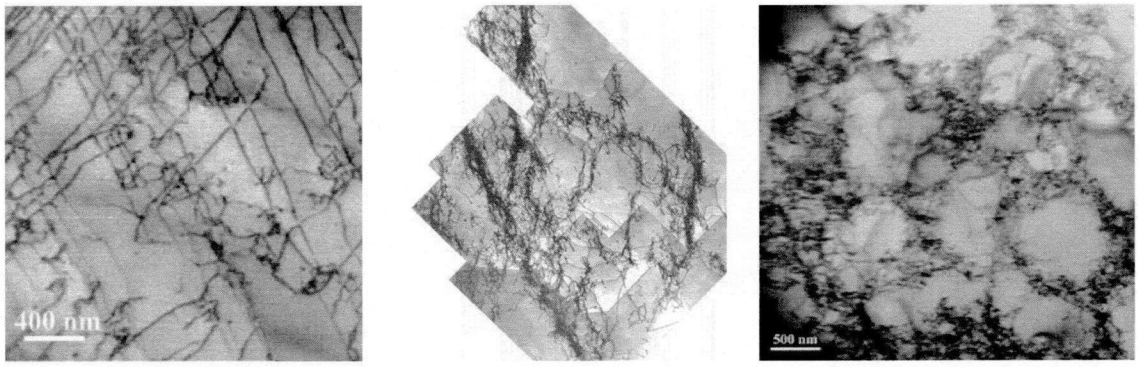

(a) (b) (c)

Fig. 1.1 TEM pictures of dislocations. (a) Dislocations in parallel slip planes in a single crystal bcc molybdenum deformed at 278K. (b) Dislocations formed bundles in single

crystal copper deformed at 77K. (c) In a single crystal bcc molybdenum deformed at 500K (the dark regions contain a high density of entangled dislocations) [5].

Dislocations define great properties of a crystalline material especially the plastic deformation. Stress-strain relations of bcc metal Molybdenum under uniaxial tension at a constant strain rate [6] are shown in Fig. 1.2.

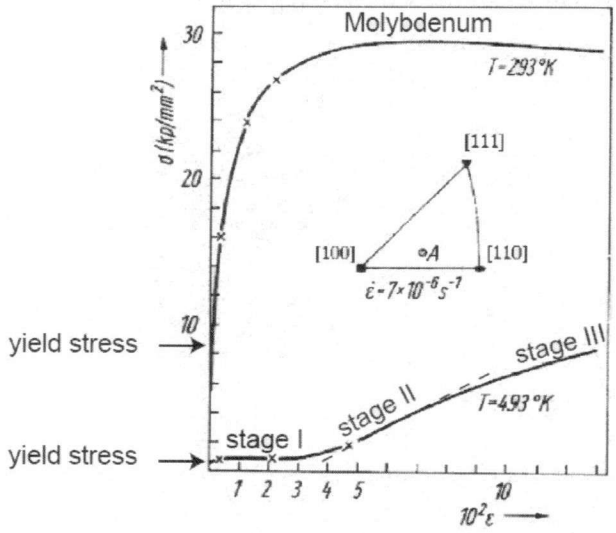

Fig. 1.2 Tensile stress-strain curve for Molybdenum at two temperatures [6].

At T = 493K, three typical stages can be observed. Stage I, called "easy glide region", happens immediately after the yield. During this stage, dislocations mostly glide on parallel slip planes and their mutual interactions are weak. Therefore, the plastic deformation proceeds without significant increase of applied stress. At stage II named as *work hardening region*, dislocations moving in non-parallel slip planes start to block each other's motions and cause intensive interactions. Frank-Read sources acting as representative phenomenas in this stage are the main reasons for dislocation multiplications. Besides, dislocations moving towards grain boundaries gain significant feedbacks, which also account for the higher deformation of this bcc metal. This stage has been studied a lot because of the variable and complex physical phenomena. Then, the crystal enters stage III in which hardening rate degenerates according to dislocation annihilation. This stage is called "parabolic hardening region" where the thermo-dynamic recovery should be key issue.

The onset of the second stage in the work hardening of a single crystal, where the curvature $\partial^2\sigma/\partial^2\varepsilon$ of a stress-strain curve becomes negative, is associated with the onset

of cross slip, as verified by experiments [7]. The cross-slip is seen by scanning-tunneling microscopy (STM) where a moving dislocation leaves a track slowly fading [8] (see Fig. 1.3).

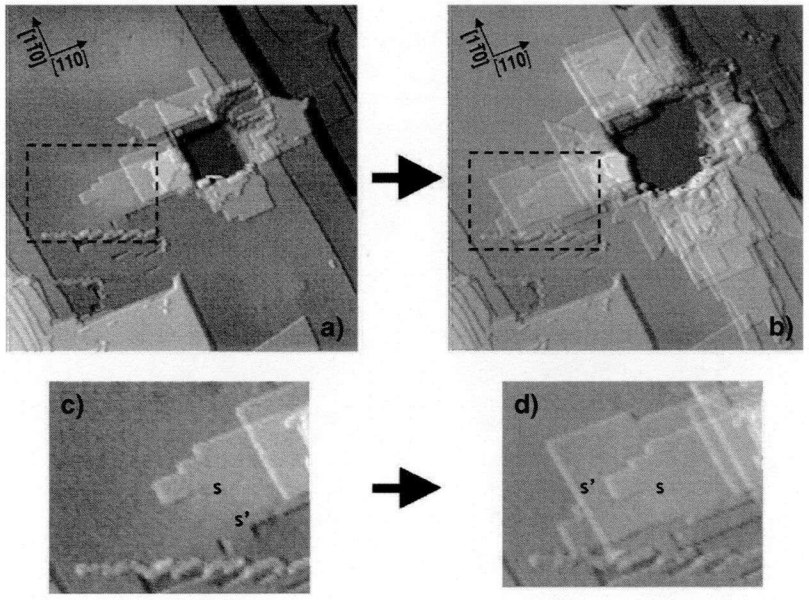

Fig. 1.3 A STM image of cross slip on Au(001) surface [8].

In stage II, there are some hardening mechanisms involved in the materials. Typical one is the well-known grain boundary hardening, so called Hall-Petch relationship [9, 10]. The other one is precipitate hardening which is often observed in aluminum alloy. The punching of coaxial prismatic dislocation loops (PDLs) in crystalline materials at precipitate-matrix interfaces without long-range applied stress is often observed by experiments [11-15] and can be exploited as the improvement of material strength [13, 14]. Precipitates employed in strengthening technique of quench-aging process [13] generate misfit strain in the vicinity and constitute nucleation sites for PDLs. These misfit stresses associated with internal stresses from PDLs can be the barriers for mobile dislocations in matrix phase and thus are the reasons for precipitation hardening (see Fig. 1.4).

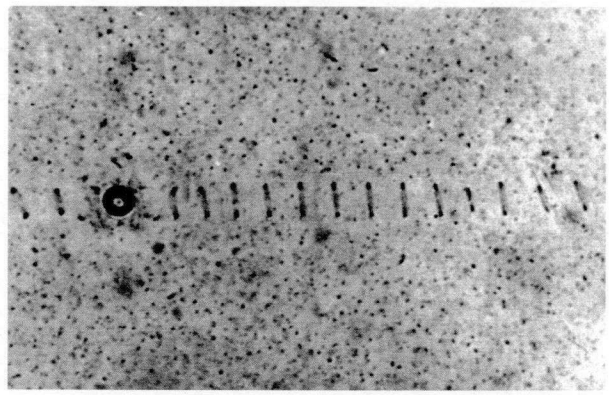

Fig. 1.4 System of PDLs produced in a silver chloride around a small glass sphere [16].

As we can see from the above discussions, dislocations play a very important role in plastic deformation of crystalline materials. In addition to a crystal's ability to yield, dislocations also control other mechanical behaviors such as creep, fatigue, indentation hardness and friction. The knowledge on such fundamental defects mechanics could give a big hint to design the practically important mechanical properties of ductility and brittleness.

1.2 Continuum Models for Dislocation Dynamics and Motivation of Research

The material modeling is a very fast growing area and attracts much attention in both academic and industrial fields [17]. Dislocation considered as a linear lattice imperfection in crystals [18] is very important phenomena in materials science and such a defect is the main reason why the practically measured yield stresses of crystals are much lower than those of theoretical values [19, 20] calculated from atomic theory based on perfect-lattice state. A wide range of resorts including atomistic and continuum processes are utilized to dislocation dynamics (DD) in order to study and analyze this sort of defect and plasmatic deformation in crystalline metals.

For the simple and ideal models of dislocations which behave endlessly extended or act perfectly symmetric, we may get the analytical equations of motion from the theoretical integral equations [18-20], but the analytical solutions become unavailable and inefficient when dislocations evolve and cannot preserve symmetry any more.

Nevertheless, dislocation simulations make it possible to model an arbitrary shaped dislocation and the collective behaviors of a bunch of dislocations.

We first introduce a series of continuum dislocation simulations for the superiority in both space range and time scale while atomistic models are restricted in relatively small material volumes, where each atom is individually resolved, and limited time scale compared with reality [5].

The continuity of a material breaks down when it meets a singularity supposed as the dislocation core in solid (denominator of strain adjacent to zero and the value becomes infinite) [21]. Peierls-Nabarro (PN) model is a continuum approach with atomistic achievement according to non-linear interatomic interactions around dislocation core. Fig. 1.5 shows the comparison of displacements between a Volterra and a PN model [22, 23].

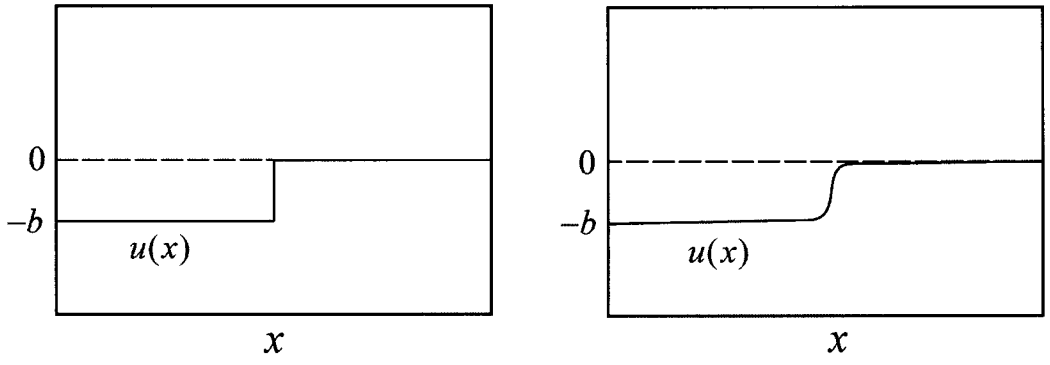

Fig. 1.5 Displacement distribution released by a dislocation.
(a)Volterra model. (b) PN model.

In the PN model (see Fig. 1.5(b)), the displacement is modified to a smooth curve instead of the pulse signal in Volterra model [7]. PN model gives a more realistic physical meaning than Volterra's mathematical hypothesis since displacement is more like continuum than discreteness. This model, as a sort of hybrid atomistic-continuum model, has been used extensively for studying dislocation core properties.

The kinetic Monte Carlo (kMC) model [24-26] is a mesoscale study that treats dislocation motions through the numerical sampling (Markovian) stochastic process. Dislocations are modeled as a system of pure screw and pure edge segments resisted in a fixed two-dimensional lattice (see Fig. 1.6).

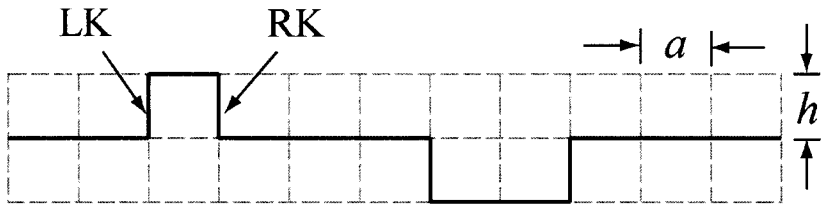

Fig. 1.6 The dislocation with kinks is represented as a collection of horizontal and vertical line segments on a regular grid. Notations *LK* and *RK* are used to differentiate between left and right kinks of the kink pair separated by a distance.

In kMC model, a dislocation is represented as a collection of horizontal and vertical line segments known as the kinks on a regular grid. The line moves upward through a sequence involving kink pair nucleation and the motion proceeds as a result of thermal fluctuation and applied stress causing double-kink nucleation/annihilation and lateral kink migration.

Discrete dislocation dynamics (DDD) separating a dislocation line into mathematical segments can demonstrate dislocation evolutions in three dimensions. This method is a typical front-tracking method that all the segments of the front are tracked at any time during the evolutions [27-30] (see Fig. 1.7).

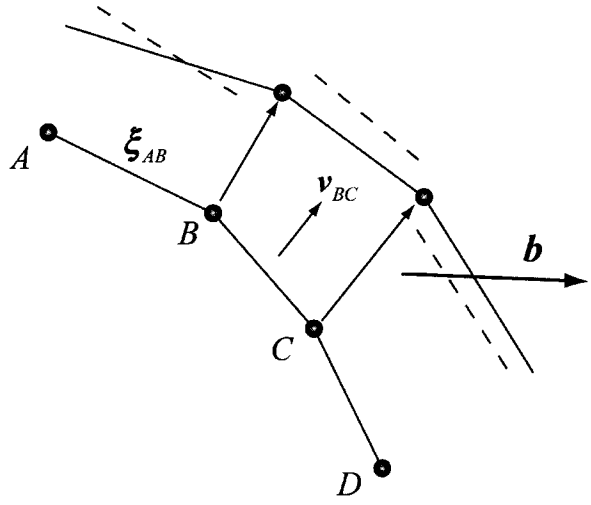

Fig. 1.7 Motion of dislocation segments.

Dislocations are represented by a set of nodes connected through straight segments. With the definition of Burgers vector $\boldsymbol{b}$, the Peach-Koehler force worked on individual segment is calculated, and then this force is transformed to a velocity $\boldsymbol{v}$ through mobility constant. Finally the segment moves according to the velocity $\boldsymbol{v}$.

DDD is much more complicated than the previous models because, for one thing, the number of segments is not fixed and should be adjusted to the length of dislocation line. For the other, all the topological processes have to be added to preserve dislocation's reactions. DDD makes tracking the evolution of a bunch of dislocations possible. Also, for a massive computation, this method is fitful for parallel computation and thus we can get well performed dislocation evolutions [31-34].

Instead of using discrete mathematical lines, phase field method (PFM) represents dislocations by a continuum field $\phi(\boldsymbol{x})$ smoothly occupying the entire simulation domain [35-37] (see Fig. 1.8). A dislocation is represented as the interface of a non-slipped region ($\phi(\boldsymbol{x})=0$) and a slipped region ($\phi(\boldsymbol{x})=1$).

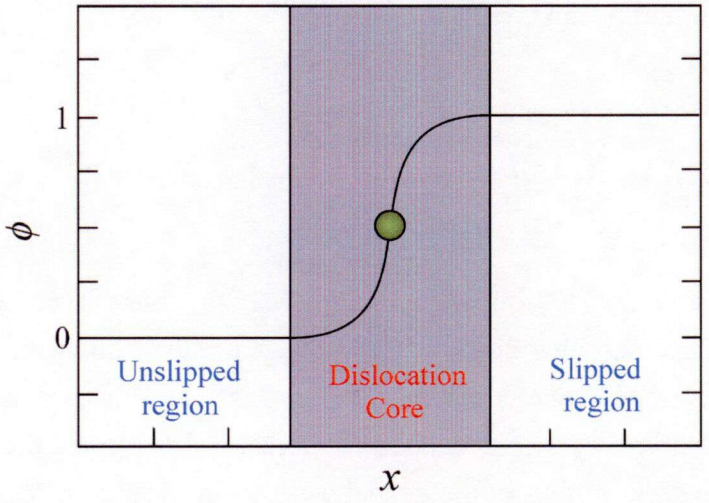

Fig. 1.8 Representing a dislocation by a phase field function [13].

During the dislocation modeling, the phase value evolves in a way that reduces the total free energy E and the dislocations are represented as a contour in two dimensions or iso-surface in three dimensions [36]. This method takes great advantage of well-developed numerical method for partial differential equations and displays well especially in modeling the evolution of dislocations.

DDD, PFM are two frequently used methods for dealing with dislocation dynamics while both of them take advantages and have limitations. We employ a new method called level set method (LSM) also using continuous functions like PFM to represent dislocations in a smooth and higher codimension way (detailed will be shown in chapters 2 and 3). More comparisons about DDD, PFM and LSM are discussed in the final chapter.

The present research endeavors to study micromechanics of line defect and manipulate dislocation evolutions by simulations. The motivation of this thesis is try to study and deliver the dislocation evolutions including dislocation/dislocation and dislocation/ inclusion interactions mainly during stage II of work hardening. And the mechanisms of some specific phenomenon (like cross-slip and double cross-slip) in that stage after elastic deformation are investigated by a computational method known as the LSM which is used as a powerful tool to deal with topological changes. This method also takes great advantages of well-developed and well-behaved numerical methods and can demonstrate physical phenomena through mathematical constructions of the higher codimension intersections in three dimensions.

1.3 Arrangement of Thesis

The content is arranged as follows. In chapter 2, the basic conception of the LSM associated with fast marching method (FMM) is generally introduced with applications. In chapter 3, several approaches have been executed accommodated to plastic deformation utilizing level set dislocation dynamics (LS-DD), and the results we obtain are well-performed according to theoretical aspects. In chapter 4, the double cross-slip of an expanding Orowan loop is modeled using LS-DD. We investigate the internal stress of the cross-slipped loop and the effects to other dislocations from the distorted dislocation loop. In chapter 5, the formation of PDLs is demonstrated. We explain the mechanism of this phenomenon and study the strain energy variation during evolution. In chapter 6, we list the conclusions of this thesis, discuss the conveniences and shortcomings of LSM and the spaces still needed to be improved.

Chapter 2

Level Set-Based Geometric Evolutions of Interfaces in Two and Three Dimensions

2.1 Abstract

The level set method (LSM) devised by Osher and Sethian [38] for the purpose of following the front propagations with curvature-dependent speed handles topological changes of implicit interface $\Gamma(t)=\{x|\phi(x,t)=0\}$ including merging and breaking in any number of space dimensions naturally. This method was original designed for modeling codimension-one objects while attempts have been made to enable level set technique to represent codimension-two geometry by the intersection of the zero level sets of a pair of level set functions. The fast marching method (FMM) with the numerical schemes for computing solutions to the nonlinear Eikonal equation is assembled together with the LSM when the speed function is defined only on the zero level set [39]. Based on entropy-satisfying upwind schemes and fast sorting techniques, FMM yields consistent and accurate extended velocities. Besides, since the powerful technique of computing distance from interfaces, FMM can create signed distance functions (SDFs) of arbitrary-shaped fronts as the initial level set functions [40].

This chapter is organized as follows. In Section 2.2, the conceptions of front propagation including implicit interface and SDFs are discussed for the preparation of understanding LSM and FMM. In Section 2.3, the general features of LSM representing codimension-two objects are explained. In Section 2.4, the detailed algorithms of FMM and the associated velocity extension are described. In Section 2.5, some selected numerical approximations and implementations of the methodology are introduced. In

Section 2.6, applications of FMM creating SDFs from fronts and demonstrations of level set-based front evolutions under normal and curvature motion are given. Finally, the differences between the evolution with and without and velocity extension are compared.

2.2 Formulations of Implicit Interface Propagation

Consider a closed front (curve in two dimensions or surface in three dimensions) dividing a region into two portions moves under a known speed function F (see Fig. 2.1). This given speed function $F(L, G, I)$ may depend on many aspects [41], where L, G and I represent:

- L: *Local properties* of the front are those determined by local geometric information, such as curvature and normal vector.
- G: *Global properties* of the front are those depending on global geometric information such as the shape and position of the front. For example, the speed might depend on integrals along the front and/or associated differential equations.
- I: *Independent properties* are those independent of local and global geometric information of the front. By which case, the physical meanings can be delivered into the front.

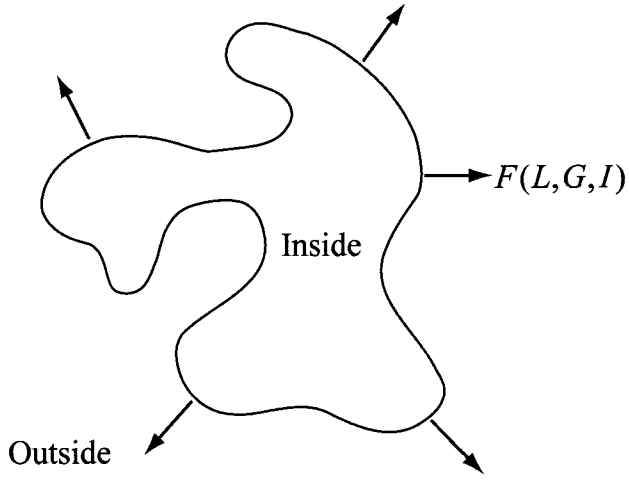

Fig. 2.1 A curve propagating with a known speed F.

The objective is to track the evolution of the interface under the given speed function F. Attempts including explicit and implicit interface representations have been made to solve this problem. Since the implicit interface propagation shows that the topological changes happen naturally, our task is to formulate this evolution problem in an Eulerian framework.

2.2.1 Implicit Representation of Interface

A standard approach to model the front propagations is to represent the interface explicitly by a set of marker particles (MPs) (see Fig. 2.2(a)). For this front-tracking method, the position of each MP is tracked to reconstruct the front at any time as the velocity on each MP is given [42, 43].

While for the implicit representation, the interface $\partial\Omega$ is stored in a set of mesh points, typically in a uniform Cartesian grid set, and is defined on the locations where the higher-dimensional implicit function ϕ is equal to zero (see Fig. 2.2(b)). The velocity is not directly defined on the interface but on all of the grid points, in which case the front propagates only when the ϕ evolves [44].

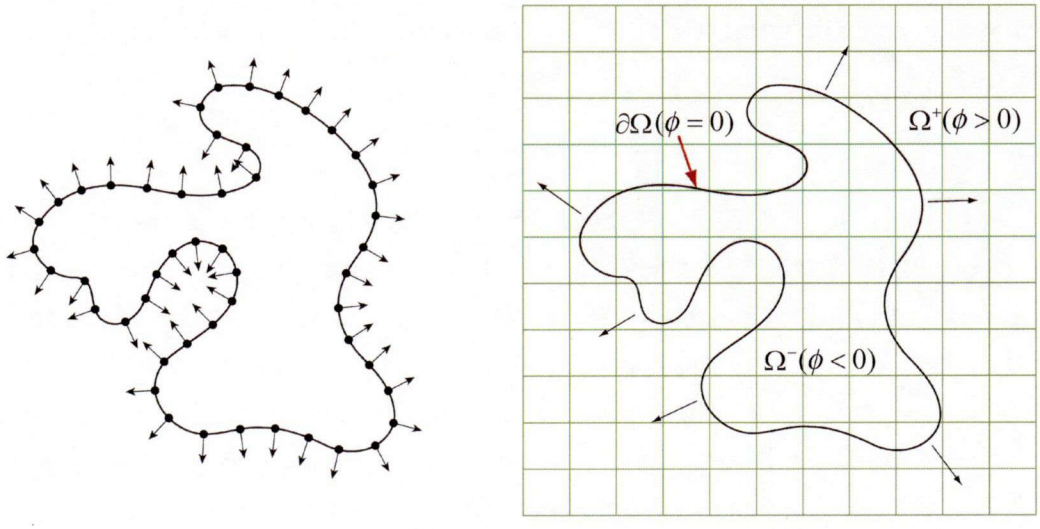

(a) (b)

Fig. 2.2 Two approaches to represent an interface. (a) Explicit representation. (b) Implicit representation.

Both the explicit and implicit representations give us the information of the front. However, we choose implicit representation for two reasons. First, the computational

time for the explicit representation depends on the number the MPs, which means a longer curve normally needs more MPs and consequently takes a longer time. While for the implicit representation, the computational time depends only on the number of mesh points no matter how long and how many curves exist in the region. Second, the explicit representation represents the interface in a direct and simple way, but needs artificial local rules to describe the topological changes especially when the merging and breaking of interface occur. While for the implicit representation, all the topological changes can be handled naturally.

2.2.2 Signed Distance Function

The interface is embedded in an implicit function ϕ with negative values in the interior region Ω^-, positive values in the exterior region Ω^+ and zero on the boundary $\partial\Omega$ (see Fig. 2.2(b)). The values in the interior and exterior regions except the interface where ϕ equals to zero are also concerned since they are involved in numerical calculations. Therefore, a smooth function is desired to make sure the front propagates smoothly.

Distance Function

Firstly, a distance function (DF) is defined as the minimum distance from $\boldsymbol{x}$ to interface [45],

$$d(\boldsymbol{x}) = \min(|\boldsymbol{x} - \boldsymbol{x}_I|) \quad , \tag{2.1}$$

where $\boldsymbol{x}_I \in \partial\Omega$. Geometrically, distance function d can be constructed as follows. If $\boldsymbol{x}$ is the point on the interface then $d(\boldsymbol{x}) = 0$. Otherwise, for any point $\boldsymbol{x}$, find the correspondent point $\boldsymbol{x}_{CI}$ on the interface which is the closest point on $\partial\Omega$ to the given point $\boldsymbol{x}$ (see Fig. 2.3), and the distance is $d(\boldsymbol{x}) = |\boldsymbol{x} - \boldsymbol{x}_{CI}|$. Noticing that the point $\boldsymbol{x}_{CI}$ is the closest point on the interface to $\boldsymbol{x}$, no other point on the interface $\partial\Omega$ can be found in the large green circle. Besides, for any other point $\boldsymbol{x}'$ on the line connecting $\boldsymbol{x}$ and $\boldsymbol{x}_{CI}$, $\boldsymbol{x}_{CI}$ is also the closest point on the interface to $\boldsymbol{x}'$.

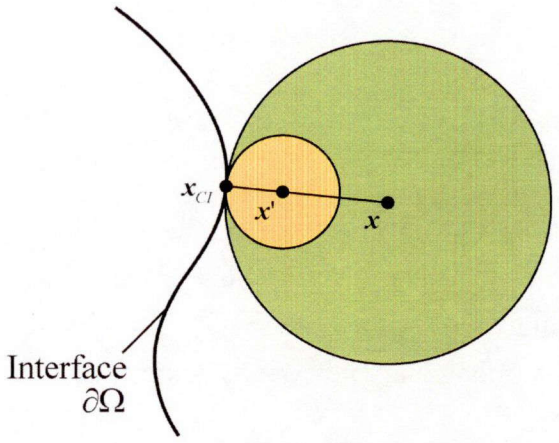

Fig. 2.3 Finding the closest point $\boldsymbol{x}_{CI}$ on the interface $\partial\Omega$ for a given point $\boldsymbol{x}$.

The line connecting $\boldsymbol{x}$ and $\boldsymbol{x}_{CI}$ is the shortest path from $\boldsymbol{x}$ to the interface, which means that this path is the one of steepest decent for function d known as the Euclidean distance function,

$$|\nabla d| = 1 \quad . \tag{2.2}$$

That is, any local deviation of path from the interface point $\boldsymbol{x}_{CI}$ to $\boldsymbol{x}$ increases a unit distance from the interface.

Signed Distance Function

A signed distance function (SDF) $\phi(\boldsymbol{x})$ is a kind of distance function with positive values outside the interface and negative values inside the interface [40],

$$\begin{cases} \phi(\boldsymbol{x}) = -d(\boldsymbol{x}) & \text{for } \boldsymbol{x} \in \Omega^- \\ \phi(\boldsymbol{x}) = 0 & \text{for } \boldsymbol{x} \in \partial\Omega \\ \phi(\boldsymbol{x}) = d(\boldsymbol{x}) & \text{for } \boldsymbol{x} \in \Omega^+ \end{cases} . \tag{2.3}$$

As we can see from Eq. (2.3), the SDF satisfies $|\phi(\boldsymbol{x})| = d(\boldsymbol{x})$ and thus shares the properties of the DF $d(\boldsymbol{x})$. It suggests that the derivative of any point from the implicit function ϕ equals to one according to of Eq. (2.2),

$$|\nabla \phi| = |\nabla d| = 1 \quad . \tag{2.4}$$

The arguments above implies that Eqs. (2.2) and (2.4) are true for any $\boldsymbol{x}$ assuming that only one unique closest interface point $\boldsymbol{x}_{CI}$ exists. However, there exist points that are equidistant from more than one distinct interface points. Besides, for an implicit function, the interface may not be analytical as a written equation, which makes it hard to find the closest interface points. Thus solving the SDF can be treated as a boundary

value problem and we induce a numerical approximation as a triumph to solve this problem.

Boundary Value Formulation

Assuming that the front always moves outward under a positive speed F in the direction normal to the front, as shown in Fig. 2.2(b), one efficient way is to parametrize the position of the expanding front with the arriving time $T(\boldsymbol{x})$ as the front crosses each point $\boldsymbol{x}$ [46]. Since ∇T is orthogonal to the front, its magnitude is inversely proportional to the speed,

$$|\nabla T| F = 1 \ , \tag{2.5}$$

where $T(\boldsymbol{x}) = 0$ for all the $\boldsymbol{x}$ on the initial location of interface Γ. According to the assumption above, this front motion can be characterized as the solution to a boundary value problem. If the speed F depends only on position $\boldsymbol{x}$, the Eq. (2.5) reduces to what is known as the Eikonal equation. Furthermore, if the front propagates with a unit speed $F = 1$, we have the relationship $|\nabla T| = 1$. That is, the arriving time function $T(\boldsymbol{x})$ for the boundary value problem can be treated as a SDF $\phi(\boldsymbol{x})$. Fig. 2.4 shows an arrival surface $T(\boldsymbol{x})$ of a circular front expanding with unit speed $F = 1$.

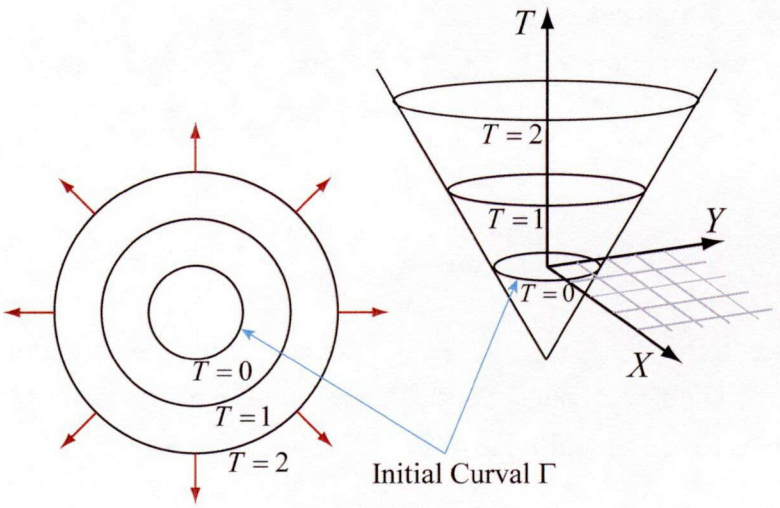

Fig. 2.4 Arrival surface T of a circle front propagating with a unit speed $F = 1$.

The distances between two neighboring circular contours are equal. Thus, the arriving time function $T(\boldsymbol{x})$ satisfying $|\nabla T| = 1$ can be considered as an implicit SDF.

2.2.3 Initial Value Formulation

Now we consider the case that the front moves with a speed F that is neither strictly positive nor negative, which means the front can move forward and backward (see Fig. 2.5). Under a given Speed, the initial curve (solid line) evolves in a normal direction that partly outward and partly inward (dashed line). In this case, the front can sweep a point $\boldsymbol{x}$ several times and a multi-valued function is required. The arriving time function $T(\boldsymbol{x})$ which is a single-valued and stationary function becomes invalid in this situation.

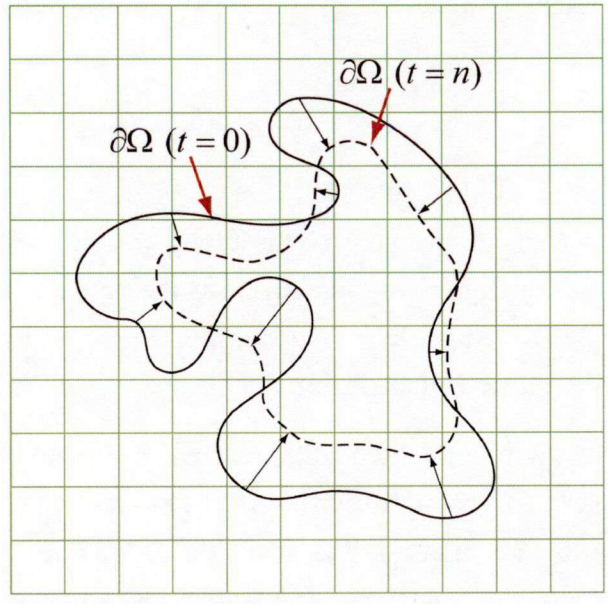

Fig. 2.5 Front propagating forward and backward.

Level Set Equation

Our way of solving problems like this is to embed the initial position of the front as the zero level set of a higher-dimensional function ϕ [47-49]. The time-dependent initial value problem treats the front propagation problem by evolving the higher-dimensional function ϕ. We first set the level set function ϕ of which the zero level set matches the original front $\phi(\gamma(\boldsymbol{s},0),0) = 0$ where $\gamma(\boldsymbol{s},t)$ denotes the interface. During the propagation, the front $\gamma(\boldsymbol{s},t)$ is always represented by the zero level set of the level set function,

$$\phi(\gamma(\boldsymbol{s},t),t) = 0 \quad . \tag{2.6}$$

Take the derivative of the equation above with respect to t according to chain rule we can get,

$$\phi_t + \nabla\phi(\gamma(s,t),t)\cdot\gamma_t(s,t) = 0 \quad . \tag{2.7}$$

where ϕ_t denotes the derivative of ϕ with respect to time, that is , $\phi_t = \partial\phi/\partial t$. Note that the derivative of γ with respect to time is the velocity of the interface $\gamma_t(s,t) = v$, Eq. (2.7) can be written as

$$\phi_t + v\cdot\nabla\phi = 0 \quad . \tag{2.8}$$

Since F is a scalar function representing the speed in the outward normal direction, we project the velocity of the front to the local normal vector n and have $\gamma_t \cdot n = F$, where $n = \nabla\phi/|\nabla\phi|$. This yields the level set evolution equation given by Osher and Sethian [38],

$$\phi_t + F|\nabla\phi| = 0 \quad , \tag{2.9}$$

as a given initial function $\phi(x,t=0)$. This time-dependent level set equation describes the multi-valued initial value problem as the time evolution of a level set function ϕ with the zero level set which is always identified as the propagating interface.

Properties of Initial Value Formulation

- It can deal with not only two dimensional but multi-dimensional interface propagation problem, for example, hypersurfaces propagating in three dimensions.
- The implicit function $\phi(x,t)$ doesn't have to be a single interface, thus the topological changes in evolving the front, especially breaking and merging, can be handled naturally.
- It relies on the viscosity solution of the associated partial differential equation in order to guarantee that the entropy-satisfying weak solution can be obtained (the details are explained in Ref. [38, 46]).
- If ϕ is a smooth well-behaved function, geometric properties including normal vector N and curvature κ of the interface can be calculated using the nodes of our Cartesian mesh:

$$N = \frac{\nabla\phi}{|\nabla\phi|} \quad ; \tag{2.10}$$

$$\kappa = \nabla\cdot N = \nabla\cdot\left(\frac{\nabla\phi}{|\nabla\phi|}\right) \quad , \tag{2.11}$$

where the curvature is defined as

$$\kappa = \frac{\phi_{xx}\phi_y^2 - 2\phi_x\phi_y\phi_{xy} + \phi_{yy}\phi_x^2}{(\phi_x^2 + \phi_y^2)^{3/2}} \quad , \tag{2.12}$$

as in two dimensions and

$$\begin{aligned}\kappa = (&\phi_x^2\phi_{yy} - 2\phi_x\phi_y\phi_{xy} + \phi_y^2\phi_{xx} + \phi_x^2\phi_{zz} - 2\phi_x\phi_z\phi_{xz} + \phi_z^2\phi_{xx} \\ &+ \phi_y^2\phi_{zz} - 2\phi_y\phi_z\phi_{yz} + \phi_z^2\phi_{yy}) / (\phi_x^2 + \phi_y^2 + \phi_z^2)^{3/2}\end{aligned} \quad , \tag{2.13}$$

as in three dimensions, respectively.

2.3 Level Set Method Representing Curves in Three Spatial Dimensions

The level set method is typically used to model codimension-one objects such as points in one dimension, curves in two dimensions and surfaces in three dimensions while Osher and coworkers extended level set technique to treat codimension-two objects using the intersection of the zero level sets of two level set functions [50]. That is, instead of implicitly representing codimension-one geometry by zero contour of one level set function ϕ, this approach represents codimension-two geometry as the intersection of the zero iso-surfaces of level set functions ϕ and ψ. Normally, a curve can only be represented in two dimensions, while by using this technique, a three dimensional curve can be represented as the intersection of two zero level set surfaces (see Fig. 2.6).

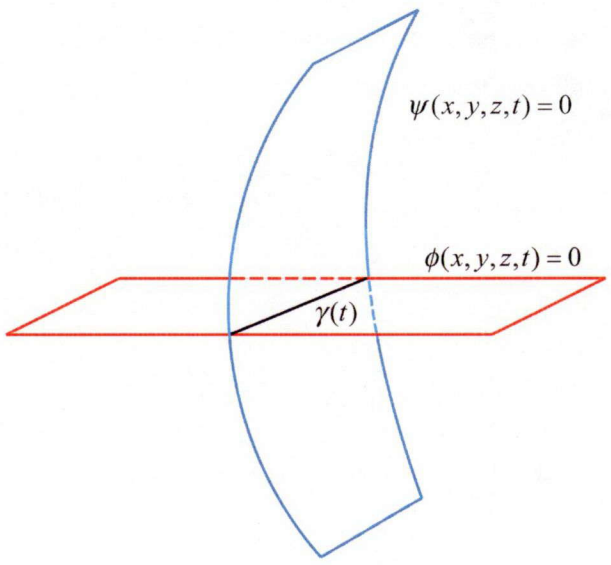

Fig. 2.6 Representing a curve as the intersection of two zero level set surfaces.

The procedure for extracting a curve in three dimensions from two hypersurfaces is as follows: first create two level set functions both of which are SDFs, then output their zero level sets ($\phi=\psi=0$) (perpendicular to each other by preference), finally extract the intersection of these zero level surfaces as the object we intend to deal with. One should be noted that the set of points satisfying $\phi = C_1$ and $\psi = C_2$ (C_1 and C_2 are constants) are also curves, however, we only concentrate on zero level sets for convenience.

2.3.1 Geometric Quantities

In order to move a curve by a geometrically based motion, a number of relevant geometric quantities of the curve need to be derived in terms of the given two level set functions ϕ and ψ. Noticing that the $\nabla\phi\times\nabla\psi$ taken on curve is tangential to it, we normalize this and get the tangent vector $\boldsymbol{T}$,

$$\boldsymbol{T} = \frac{\nabla\phi\times\nabla\psi}{\left|\nabla\phi\times\nabla\psi\right|} \quad . \tag{2.14}$$

If we replace ϕ with $-\phi$, the direction of the tangent vector will be reversed. The curvature times normal vector $\kappa\boldsymbol{N}$ is the derivative of the tangent vector along the direction of the curve $\boldsymbol{s}$,

$$\kappa\boldsymbol{N} = \frac{d\boldsymbol{T}}{d\boldsymbol{s}} = \nabla\boldsymbol{T}\cdot\boldsymbol{T} = \begin{pmatrix} \nabla T_1\cdot\boldsymbol{T} \\ \nabla T_2\cdot\boldsymbol{T} \\ \nabla T_3\cdot\boldsymbol{T} \end{pmatrix} , \tag{2.15}$$

where T_1, T_2, T_3 are the components of tangent vector $\boldsymbol{T}$. Then the normal vector $\boldsymbol{N}$ can be calculated by normalizing the curvature times normal vector $\kappa\boldsymbol{N}$,

$$\boldsymbol{N} = \frac{\kappa\boldsymbol{N}}{\left|\kappa\boldsymbol{N}\right|} \quad . \tag{2.16}$$

The binormal vector $\boldsymbol{B}$ is defined as

$$\boldsymbol{B} = \frac{\boldsymbol{T}\times\boldsymbol{N}}{\left|\boldsymbol{T}\times\boldsymbol{N}\right|} \quad . \tag{2.17}$$

And the torsion times normal vector $\tau\boldsymbol{N}$ is defined as

$$\tau\boldsymbol{N} = -\nabla\boldsymbol{B}\cdot\boldsymbol{T} \quad . \tag{2.18}$$

As we can see from Eqs. (2.14)-(2.18), all these geometric quantities of the curve can be written in terms of ϕ and ψ. And these geometric quantities can also be used for an arbitrary point in three dimensions of the curve $\{\phi = C_1, \psi = C_2\}$. One should be mentioned that not all the curves of the normal and binormal motions evolve as nicely as curvature motions [46].

2.3.2 Evolution Equations

Moving a curve in three dimensions is actually evolving two level set functions ϕ and ψ. The velocity field $\boldsymbol{v}$ under which the curve moves is first investigated, then both ϕ and ψ undergo the same partial differential equation known as the level set equations:

$$\begin{aligned} \phi_t + \boldsymbol{v} \cdot \nabla \phi = 0 \\ \psi_t + \boldsymbol{v} \cdot \nabla \psi = 0 \end{aligned} \quad . \tag{2.19}$$

Eq. (2.19) shows the level set evolution equations in terms of ϕ and ψ of which the intersection is the very curve we want to deal with and investigate. In fact, a viscosity coefficient could be added on the right-hand for a parabolic problem in order to get a better accuracy but may cause diffusion and oscillatory [19]. $\phi_t(\partial\phi(\boldsymbol{x},t)/\partial t)$ and $\psi_t(\partial\psi(\boldsymbol{x},t)/\partial t)$ are time interval derivatives while $\nabla\phi(\partial\phi(\boldsymbol{x},t)/\partial x_i)$and $\nabla\psi(\partial\psi(\boldsymbol{x},t)/\partial x_i)$ are spatial derivatives with respect to x, y, and z coordinates. One should be noticed that the velocity field $\boldsymbol{v}$ for evolving ϕ and ψ are exactly the same. Let $\gamma(\boldsymbol{s},t)$ denotes an arbitrary curve in three dimensions, then this intersection can be represented by ϕ and ψ as

$$\begin{aligned} \phi(\gamma(\boldsymbol{s},t),t) = C_1 \\ \psi(\gamma(\boldsymbol{s},t),t) = C_2 \end{aligned} \quad . \tag{2.20}$$

Taking a derivative of Eq. (2.20) with respect to t gives

$$\begin{aligned} \nabla\phi(\gamma(\boldsymbol{s},t),t) \cdot \gamma_t(\boldsymbol{s},t) + \phi_t(\gamma(\boldsymbol{s},t),t) = 0 \\ \nabla\psi(\gamma(\boldsymbol{s},t),t) \cdot \gamma_t(\boldsymbol{s},t) + \psi_t(\gamma(\boldsymbol{s},t),t) = 0 \end{aligned} \quad , \tag{2.21}$$

with making a comparison with Eq. (2.19), we have $\gamma_t(\boldsymbol{s},t) = \boldsymbol{v}$. Since C_1 and C_2 are arbitrary constants, the evolution equation (2.19) is valid for all of the points in three spatial dimensions.

2.4 Fast Marching Method and Velocity Extension

Fast Marching Method (FMM) is a numerical scheme for computing solutions to the nonlinear Eikonal equation known as the boundary problem [51-53]. Based on entropy-satisfying upwind schemes, causality relationship and fast sorting techniques, FMM yields consistent, accurate and efficient algorithms computing distances from complex curves and surfaces. The reconstructed SDFs can be used as the initial and reinitialized functions during propagating the fronts of level set functions. FMM can also construct a velocity extended to the whole computational region when only a localized velocity on the front is determined to make sure that all the non-zero level sets evolve smoothly according to the front.

2.4.1 Approximation Schemes to Eikonal Equation

Fast marching method is a computational technique approximating the solution to Eikonal equation which is a first order hyperbolic partial differential equation with the form:

$$|\nabla T(\boldsymbol{x})| = F(\boldsymbol{x}),\ \boldsymbol{x} \in R^n \tag{2.22}$$

where $F(x) > 0$ and the boundary condition, $T(\boldsymbol{x}) = \phi(\boldsymbol{x}),\ \boldsymbol{x} \in \Gamma \subset R^n$. The $F(\boldsymbol{x})$ on the right side is typically supplied as given input to the equation while the boundary information that $T(\boldsymbol{x})$ equals to a known function according to the prescribed curve or surface Γ in n-dimensions.

Due to the nonlinearity, the equation may be non-differentiable even with smooth boundary. Thus, beyond the formation of the discontinuity in the derivative that yields 'shocks' against entropy condition in the hyperbolic conservation law, the numerical technique called FMM that naturally accounts for the non-differentiability and admits physically corrected non-smooth solutions is devised. This consistent, accurate and efficient technique known as a stationary boundary value problem first calls upwind viscosity schemes and thus automatically selects solutions including non-differentiability. On the other hand, by coupling the causality of the schemes to fast sorting methods borrowed from discrete network problems, FMM gives a high efficiency: the complexity is $O(N\log_2(N))$, where N is the total number of grid points in the whole domain.

A one-sided upwind scheme for solving Eq. (2.22) in three dimensions is constructed as:

$$\begin{bmatrix} \max(D^{-x}_{i,j,k}T,0)^2 + \min(D^{+x}_{i,j,k}T,0)^2 \\ + \max(D^{-y}_{i,j,k}T,0)^2 + \min(D^{+y}_{i,j,k}T,0)^2 \\ + \max(D^{-z}_{i,j,k}T,0)^2 + \min(D^{+z}_{i,j,k}T,0)^2 \end{bmatrix}^{1/2} = F_{i,j,k} \quad . \tag{2.23}$$

While a slightly revised scheme given in [54] turns out to be more convenient

$$\begin{bmatrix} \max(D^{-x}_{i,j,k}T,-D^{+x}_{i,j,k}T,0)^2 \\ + \max(D^{-y}_{i,j,k}T,-D^{+y}_{i,j,k}T,0)^2 \\ + \max(D^{-z}_{i,j,k}T,-D^{+z}_{i,j,k}T,0)^2 \end{bmatrix}^{1/2} = F_{i,j,k} \quad , \tag{2.24}$$

where D^{-x}, D^{+x}, D^{-y}, D^{+y}, D^{-z} and D^{+z} are backward and forward finite difference operators in x, y and z coordinate directions defined as:

$$\begin{aligned} D^{-x}_{i,j,k}u &= \frac{T_{i,j,k} - T_{i-1,j,k}}{h}, \quad D^{+x}_{i,j,k}u = \frac{T_{i+1,j,k} - T_{i,j,k}}{h} \\ D^{-y}_{i,j,k}u &= \frac{T_{i,j,k} - T_{i,j-1,k}}{h}, \quad D^{+y}_{i,j,k}u = \frac{T_{i,j+1,k} - T_{i,j,k}}{h} \\ D^{-z}_{i,j,k}u &= \frac{T_{i,j,k} - T_{i,j,k-1}}{h}, \quad D^{+z}_{i,j,k}u = \frac{T_{i,j,k+1} - T_{i,j,k}}{h} \end{aligned} \quad . \tag{2.25}$$

2.4.2 The Algorithm of Fast Marching Method

Iteration

One way to solve Eq. (2.24), given by Rouy and Tourin in [54], is through iteration. Consider a stencil of a grid point with its six neighbors in three dimensions, as shown in Fig. 2.7.

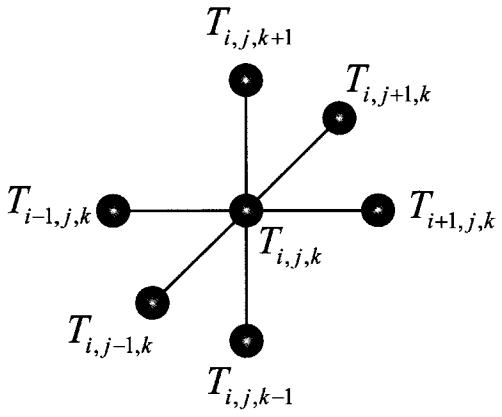

Fig. 2.7 Updating a grid point.

Assuming each neighboring grid value for $T_{i,j,k}$ is given, Eq. (2.24) is a quadratic equation for T. The solution is by updating the value of T at each grid point according to this quadratic equation until a solution is reached:

For iter = 1:n
  For i,j,k = 1:dim
    Solve Quadratic for $T_{i,j,k}$ of the (m+1)-th iteration, given
      $T_{i\text{-}1,j,k}$, $T_{i+1,j,k}$, $T_{i,j\text{-}1,k}$, $T_{i,j+1,k}$, $T_{i,j,k\text{-}1}$, $T_{i,j,k+1}$ of the m-th iteration
  End
End

Given N elements in each direction for a three-dimensional grid, the computations yields at least $O(N^4)$ labors.

Causality

The central idea behind the FMM is to systematically construct the solution T using only upwind values, that is, the information propagates from smaller values of T to larger values according to the upwind difference structure of Eq. (2.24). During the procedure, we march the narrow band forward from the front, freeze the values of existing points and bring new ones into the thin zone.

Consider a two-dimensional version of solving Eikonal equation with the boundary value known as the origin (the black sphere in Fig. 2.8(a)) and light gray spheres are grid points with unknown solutions. We start the algorithm by solving the Eq. (2.24) from the target point downwind to its four neighboring grid points (shown as the green spheres in Fig. 2.8(b)), then freeze the green sphere with the smallest value and proceed with the downwind progressing algorithm. Noticing that recomputing the T values at

downwind neighboring points can't yield smaller values than any of the known points, we can systematically move forward. Besides, we will never go back and revisit a grid point with a known value.

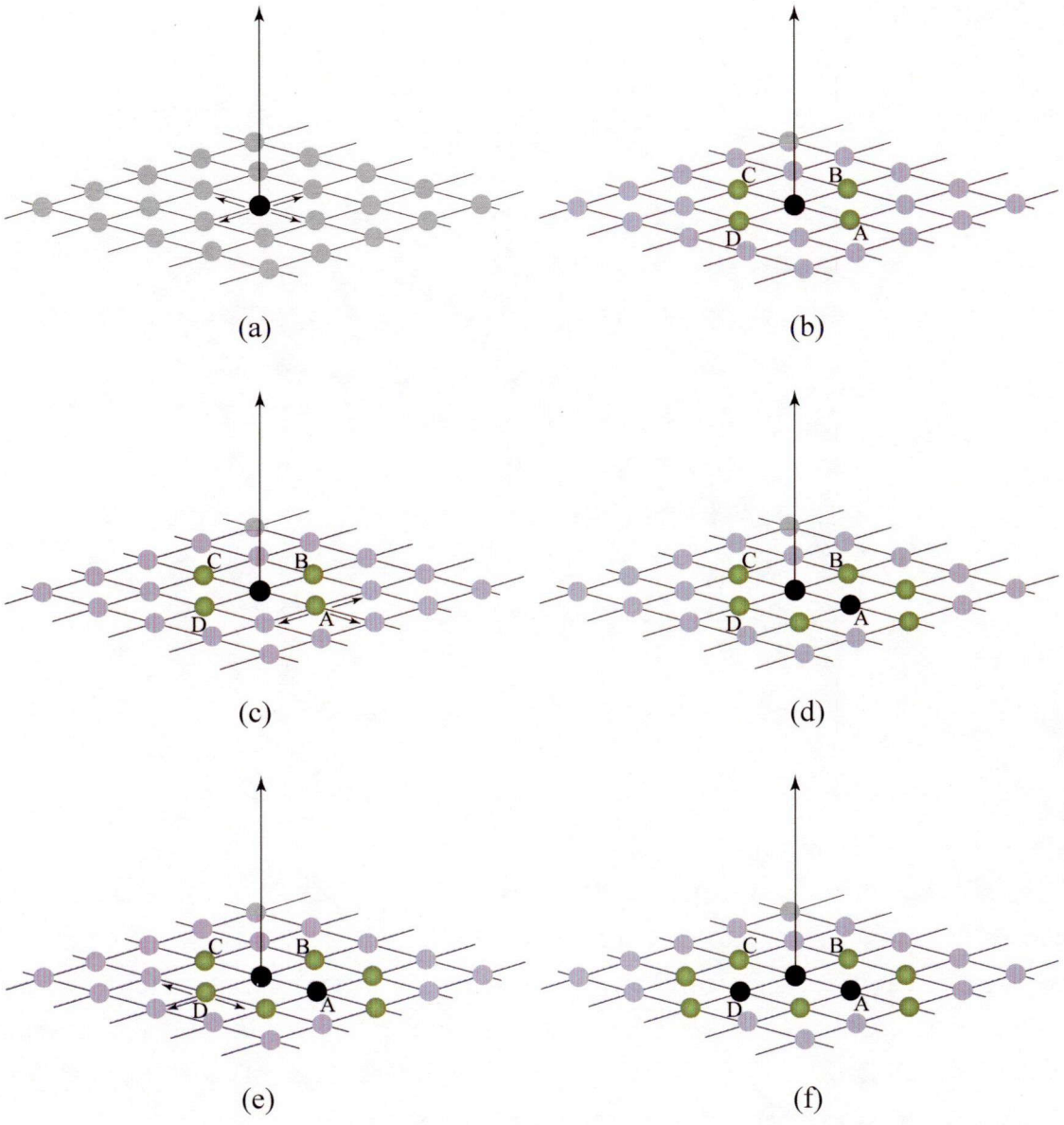

Fig. 2.8 Update procedure of FMM.

Points are divided into three species (see Fig. 2.9): Accepted (black points), Neighbor (green points in the narrow band) and Far Away points (light gray points). Then the update procedure for FMM is as follows:

(a) Begin loop: Let A be the *Trial* Point with the smallest T value.

(b) Add the point A to *Known*; remove it from *Trial*.

(c) Tag all neighbors of A that are not *known* as *Trial*. If the neighbor is in *Far*, remove from *Far* add to the set *Trial*.

(d) Recompute the values of T at all *Trial* neighbors of A according to Eq. (2.24) by solving the quadratic equation.

(e) Return to the top of the loop.

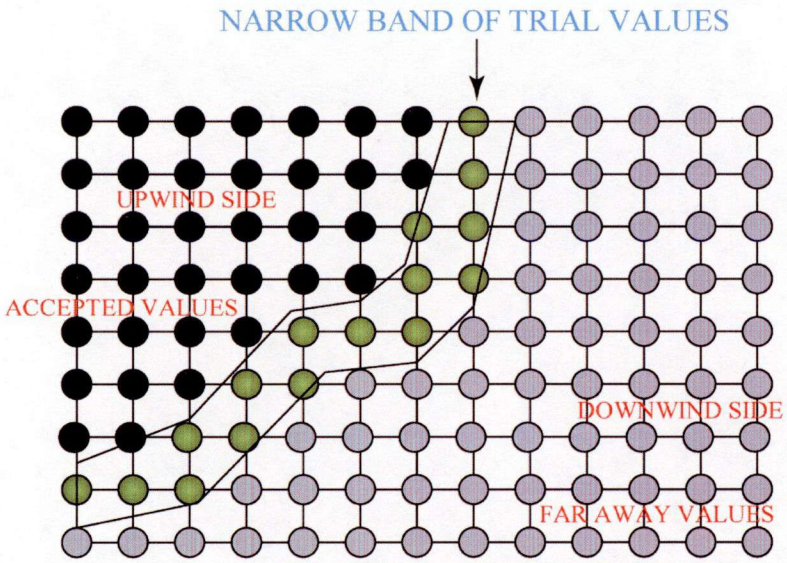

Fig. 2.9 Upwind construction of *Accepted* value.

Heap Sort and Computational Efficiency

The efficiency of the marching technique largely lies on locating the grid point in the narrow band with the smallest value for T. We introduce the heap sort which is a comparison-based sorting algorithm. All the grid points including the values of T and indices in the narrow band are stored in the min-heap data structure (see the complete binary tree of Fig. 2.10). The algorithm starts with finding the smallest element with the location in the narrow band and the loop is as follows [55]:

Step I (*DownHeap*): Eliminate the root and use one sweep of *DownHeap* to ensure the remaining elements satisfying the min-heap structure.

Step II (*Insert*): The *Far Away* neighbors (gray points in the downwind side of Fig. 2.9) are added to the heap using an *Insert* operation, and remaining neighbors in the heap are updated according Eq. (2.24).

Step III (*UpHeap*): Use the *UpHeap* operation for all the updated elements upward to the correct locations in the heap.

Step IV: Return to the top of the loop.

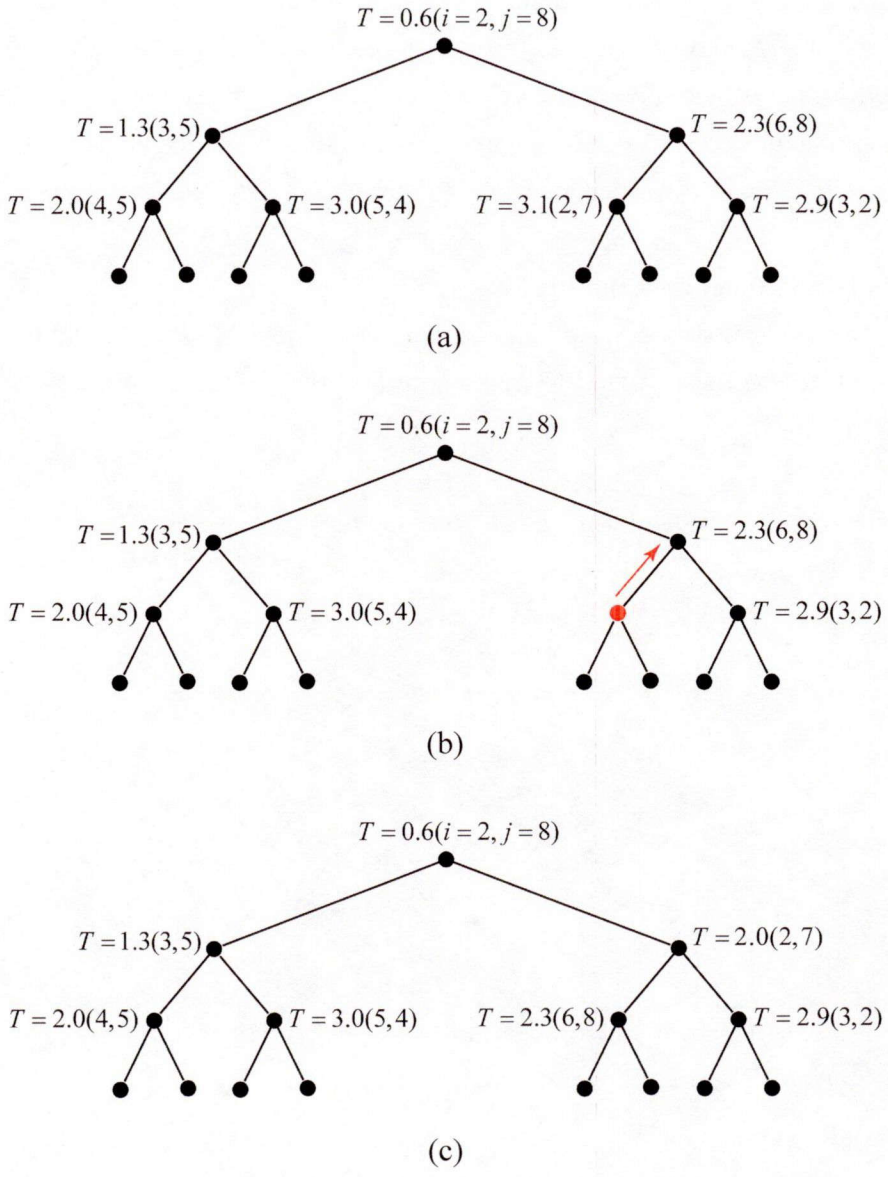

Fig. 2.10 Heap structure and *UpHeap*+ operator.

The *DownHeap* and *UpHeap* operations carry an element from root to bottom and from bottom to root (in the worst case), respectively. Each array access takes $O(1)$ time, thus this algorithm has the complexity of $O(\log_2(M))$, assuming M elements in the heap. Suppose a three-dimensional grid with N points in each direction, the FMM reduces the total operations count to $O(N^3\log_2(N))$.

2.4.3 The Fast Construction of Extension Velocities

The velocities are available for all the level sets throughout the whole computational domain if the interface moves under the self geometric quantities [56-58]. However, in many applications, we can define the velocity only on interfaces which have the realistic meanings (for example, physical meaning). Thus, the velocities need to be extended from the interface to all the other level sets to maintain a nice level set representation.

Equations for Extension Velocities

There are various approaches to extension velocities [59-61] while a technique calling the algorithm of FMM is utilized to make sure that the velocities are created in such a way that SDF is always preserved (see Fig. 2.11).

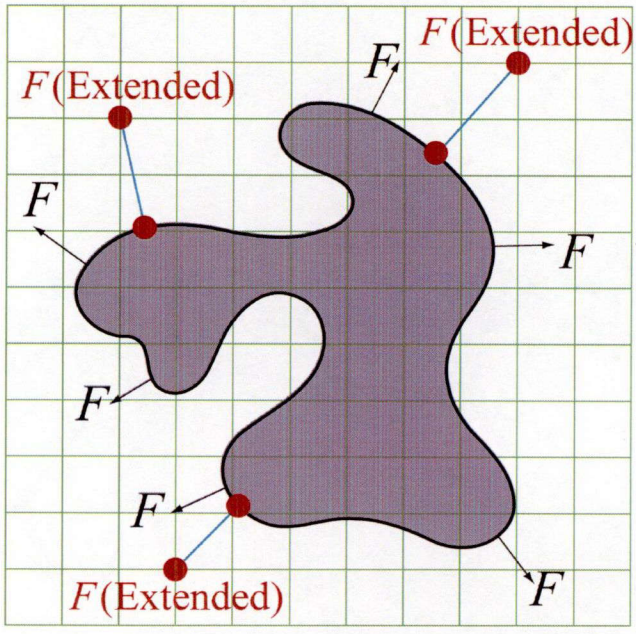

Fig. 2.11 Building extension velocities.

Considering for a moment the level set function is an initial SDF $\phi(\boldsymbol{x},t=0)$, we build an extension velocity which satisfies

$$\nabla F_{\text{ext}} \cdot \nabla \phi = 0 \quad . \tag{2.26}$$

Suppose that both F_{ext} and ϕ are smooth, Since the initial function satisfies $|\nabla \phi(\boldsymbol{x}, t=0)| = 1$ and the function evolves under the level set equation $\phi_t + F_{\text{ext}}|\nabla \phi| = 0$. Then, we notice that

$$\frac{d|\nabla\phi|^2}{dt} = \frac{d}{dt}(\nabla\phi\cdot\nabla\phi) = 2\nabla\phi\cdot\frac{d}{dt}\nabla\phi \quad . \qquad (2.27)$$
$$= -2\nabla\phi\cdot\nabla F_{\text{ext}}|\nabla\phi| - 2\nabla\phi\cdot\nabla|\nabla\phi|F_{\text{ext}}$$

The first term on the right-side is zero because the extension velocity is constructed according to Eq. (2.26) and the second term is also zero because $|\nabla\phi(\boldsymbol{x},t=0)|=1$. Thus, the solution satisfies $|\nabla\phi(\boldsymbol{x},t)|=1$, which means that the level set function ϕ is always a SDF.

Constructing the Velocity Extension

Once the values for both the signed distance and extension velocities are established at *Trial* points[62-64], the routine of updating extension values can be started. As the distance value is updated using FMM, the extension value is calculated according to Eq. (2.24).

Consider a case that the new distance value at (i, j) is found by solving Eq. (2.24). Suppose that $(i+1, j)$ and $(i, j-1)$ are the points that are used for updating the distance and the v is the new extension value. In order to satisfy the upwind scheme, we have

$$\left(\frac{\phi^{\text{temp}}_{i+1,j}-\phi^{\text{temp}}_{i,j}}{h}, \frac{\phi^{\text{temp}}_{i,j}-\phi^{\text{temp}}_{i,j-1}}{h}\right)\cdot\left(\frac{F_{i+1,j}-v}{h}, \frac{v-F_{i,j-1}}{h}\right)=0 \quad , \qquad (2.28)$$

which can be written with respect to v as

$$v = \frac{F_{i+1,j}(\phi^{\text{temp}}_{i,j}-\phi^{\text{temp}}_{i+1,j}) + F_{i,j-1}(\phi^{\text{temp}}_{i,j}-\phi^{\text{temp}}_{i,j-1})}{(\phi^{\text{temp}}_{i,j}-\phi^{\text{temp}}_{i+1,j}) + (\phi^{\text{temp}}_{i,j}-\phi^{\text{temp}}_{i,j-1})} \quad . \qquad (2.29)$$

In this case, during the evolution, Eq. (2.26) is always satisfied for all the points on the computational region except the points along the front itself of which the values are already defined.

2.5 Numerical Approximations and Implementations

In this section, we explain some numerical approximations for solving level set equations including terms of spatial derivatives and time interval derivatives from partial differential equations (PDEs). Reinitializations are utilized after several

evolution steps to reduce the numerical errors. Finally, we introduce the visualization of curves from two level set functions in three dimensions.

2.5.1 Weighted Essentially Non-oscillatory (WENO)

Numerical calculation, because of its discretization and way of approximation, cannot be totally trusted. Lots of mathematicians in applied mathematics are committing themselves to deliver more stable and accurate approximations of numerical partial differential equations and try to explain them [65-67]. These are widely used in computational science which could get different aspects with different choices of partial differential methods. The next example shows the stability and convergence of weighted essentially non-oscillatory (WENO) [68, 69] for PDEs compared with central differential method.

We suppose an initial function with a "V" formed by rays meeting at the middle of a coordinate ($x = 0$), see the nethermost curve in Fig. 2.12. When the front undergoes the evolution as

$$\psi_t = F(1+\psi_x^2)^{1/2} \quad , \tag{2.30}$$

as we can see, this front becomes severely oscillatory using central differential method (see Fig. 2.12),

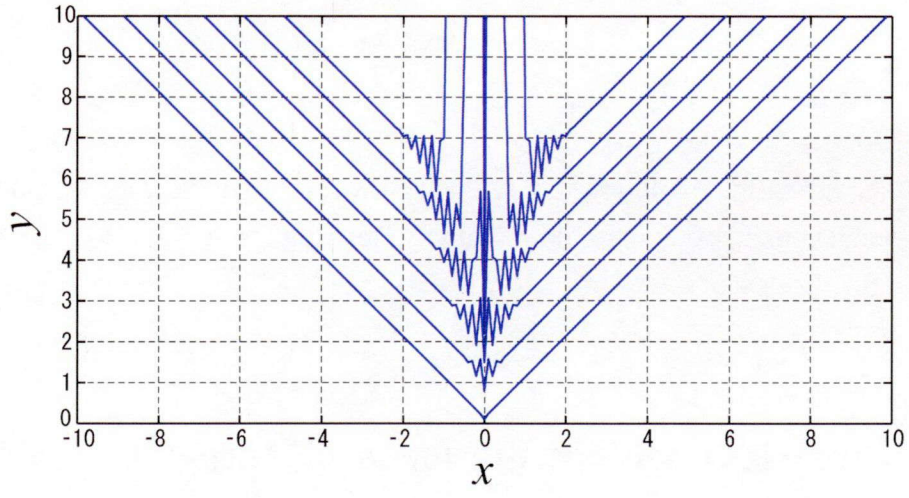

Fig. 2.12 Central differences for PDEs with $\Delta t = 0.1$.

and oscillatory becomes even more severe when Δt becomes smaller (as shown in Fig. 2.13).

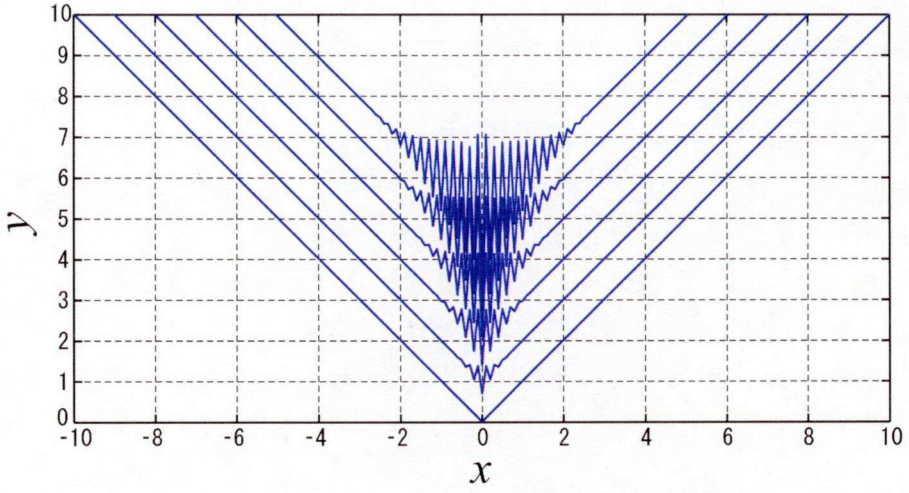

Fig. 2.13 Central differences for PDEs with $\Delta t = 0.01$.

The oscillation happens because in the middle of the front where $x = 0$, the gradient of this point is always zero no matter how fine the mesh grids could be and how small the increment of time is chosen, we could never get a proper gradient. Not only symmetric but also unsymmetric shape, if peak point like this (here in $x = 0$) appeared, the evolution will not be presented appropriately.

Osher and coworkers [68-71] thought about a way that can solve this problem, as we can see from Fig. 2.14.

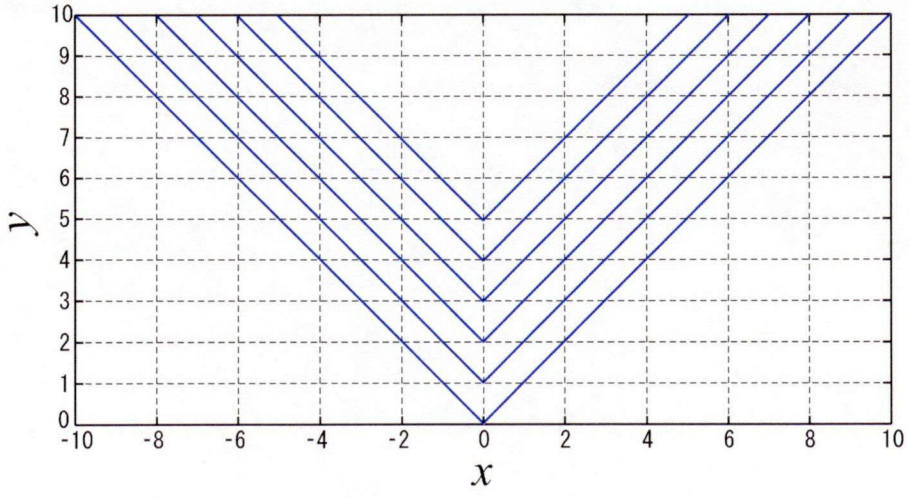

Fig. 2.14 WENO differences for PDEs with Δt=0.01.

They use WENO which is a kind of upwind differential method when solving the spatial differential part of the evolution equation and gives the result almost like exact solution. It is very useful method not only in 2D but also in 3D where topological changes are dramatic and computations get hard.

For a simple LSM, central differential method can represent the spatial derivatives good enough. But for dislocation lines, the evolution may oscillatory dramatically unless using WENO methods [70] which are not only stable and convergent but also can provide smaller truncations and global errors.

Firstly, backward WENO be induced (while forward WENO not essentially changes) by using six points $\{\phi_{i-3}, \phi_{i-2}, \phi_{i-1}, \phi_i, \phi_{i+1}, \phi_{i+2}\}$
Then define five derivatives using backward difference are defined as,

$$v_1 = D^{-1}\phi_{i-2},\ v_2 = D^{-1}\phi_{i-1},\ v_3 = D^{-1}\phi_i,\ v_4 = D^{-1}\phi_{i+1},\ v_5 = D^{-1}\phi_{i+2} \tag{2.31}$$

A set of approximations can be deduced

$$\begin{aligned}
\nabla\phi^1 &= \frac{v_1}{3} - \frac{7v_2}{6} + \frac{11v_3}{6} \\
\nabla\phi^2 &= -\frac{v_2}{6} + \frac{5v_3}{6} + \frac{v_4}{3} \\
\nabla\phi^3 &= \frac{v_3}{3} + \frac{5v_4}{6} - \frac{v_5}{6}
\end{aligned} \tag{2.32}$$

The Hamiltonian-Jacobi (HJ) WENO approximation of $(\nabla\phi^-)_i$ is a convex combination of these three equations. Then weight function using the set of approximations turns to be

$$\nabla\phi = \omega_1\nabla\phi^1 + \omega_2\nabla\phi^2 + \omega_3\nabla\phi^3 \ . \tag{2.33}$$

In order to define the weights, we estimate the smoothness of the stencils:

$$\begin{aligned}
S_1 &= \frac{13}{12}(v_1 - 2v_2 + v_3)^2 + \frac{1}{4}(v_1 - 4v_2 + 3v_3)^2 \\
S_2 &= \frac{13}{12}(v_2 - 2v_3 + v_4)^2 + \frac{1}{4}(v_2 - v_4)^2 \\
S_3 &= \frac{13}{12}(v_3 - 2v_4 + v_5)^2 + \frac{1}{4}(3v_3 - 4v_4 + v_5)^2
\end{aligned} \tag{2.34}$$

Intermediary parameters for weights can be like

$$\alpha_1 = \frac{0.1}{(S_1 + \varepsilon)^2}$$
$$\alpha_2 = \frac{0.6}{(S_2 + \varepsilon)^2} \quad . \tag{2.35}$$
$$\alpha_3 = \frac{0.3}{(S_3 + \varepsilon)^2}$$

Finally, we obtain the weights ω_1, ω_2 and ω_3 from intermediary parameters

$$\omega_1 = \frac{\alpha_1}{\alpha_1 + \alpha_2 + \alpha_3}$$
$$\omega_2 = \frac{\alpha_2}{\alpha_1 + \alpha_2 + \alpha_3} \quad . \tag{2.36}$$
$$\omega_3 = \frac{\alpha_3}{\alpha_1 + \alpha_2 + \alpha_3}$$

For this method is one-sided, we should calculate the other side (forward WENO) alternately for several evolution steps.

2.5.2 Total Variation Diminishing Runge-Kutta (TVD-RK)

We tried several numerical methods for solving time differential problem. The simplest way is Euler equation which is a forward evolution [65, 66],

$$y^{n+1} = y^n + h \cdot f(x, y, z, t) \quad , \tag{2.37}$$

while $f(x, y, z, t) = y'$ is at the n-th time step. For this is explicit method, a better method of approximation: total variation diminishing (TVD) Runge-Kutta should be introduced:

$$\begin{cases} y^{n+1} = y^n + h \cdot f^n(x, y, z, t) \\ y^{n+2} = y^{n+1} + h \cdot f^{n+1}(x, y, z, t) \\ y^{n+1/2} = 3y^n / 4 + y^{n+2} / 4 \\ y^{n+3/2} = y^{n+1/2} + h \cdot f^{n+1/2}(x, y, z, t) \\ y^{n+1} = y^n / 3 + 2y^{n+3/2} / 3 \end{cases} \quad . \tag{2.38}$$

Eq. (2.38) is a third-order accurate TVD Runge-Kutta equation, while higher order accurate TVD Runge-Kutta also exists but does not make a significance improvement for accuracy. The associated Courant-Friedrichs-Lewy (CFL) condition should be

considered to decide the interval step while an algorithm adaptive may be smart to be used (see Ref. [5], Page 216).

2.5.3 Reinitialization

Reinitialization for Signed Distance Function

During evolution, a level set function may not always be a SDF, so we have to modify the function after each or several iterations and run the PDE for ϕ below until it gets steady state:

$$\begin{aligned} &\tilde{\phi}_t + \text{sign}(\phi)(|\nabla\tilde{\phi}| - 1) = 0 \\ &\tilde{\phi}(t=0) = \phi \end{aligned}, \tag{2.39}$$

where the function sign(x) is defined as

$$\text{sign}(x) = \begin{cases} -1, & x < 0 \\ 0, & x = 0 \\ 1, & x > 0 \end{cases}. \tag{2.40}$$

Similarly, the renewed signed distance function $\tilde{\psi}$ from level set function ψ,

$$\begin{aligned} &\tilde{\psi}_t + \text{sign}(\psi)(|\nabla\tilde{\psi}| - 1) = 0 \\ &\tilde{\psi}(t=0) = \psi \end{aligned}. \tag{2.41}$$

This was also solved for the steady state using third order TVD Runge-Kutta in time combined with fifth order WENO in space. Noticing that fast marching method and fast sweeping method can also do this reinitialization for making a non-SDF to be a SDF while after each iteration but the computations cost too much.

Reinitialization for Perpendicular Zero Level Sets

According to Osher [40], the initial plane of zero levels should better be perpendicular to each other. To realize this, we also run a PDE for ϕ,

$$\begin{aligned} &\tilde{\phi}_t + \text{sign}(\psi)\frac{\nabla\psi}{|\nabla\psi|}\cdot\nabla\tilde{\phi} = 0 \\ &\tilde{\phi}(t=0) = \phi \end{aligned}, \tag{2.42}$$

and similarly, we have the form for the other level set function

$$\begin{aligned} &\tilde{\psi}_t + \text{sign}(\phi)\frac{\nabla\phi}{|\nabla\phi|}\cdot\nabla\tilde{\psi} = 0 \\ &\tilde{\psi}(t=0) = \psi \end{aligned} \quad . \tag{2.43}$$

This could be used once after several time steps of evolution equations.

2.5.4 Three-dimensional Visualization

The following explanation is how we can get the intersection from two implicit level set functions while Refs. [72] and [73] give us another consideration for finding points of interest.

For each grid-cube:

i. Split the grid-cube into 6 tetrahedron (5 is possible as well). Suppose we map the grid-cube to the unit cube with corner at the origin. Thus the corners of the cube are (x_1, x_2, x_3), where x_i are 0 or 1. Take a permutation of (1, 2, 3), and call it (i_1, i_2, i_3). Consider the points (x_1, x_2, x_3) such that x_i ether be 0 or be 1 and $0 \le x_{i_1} \le x_{i_2} \le x_{i_3} \le 1$ is satisfied. These points are the corners of one tetrahedron. Since there are 6 permutations of (1, 2, 3), we get 6 tetrahedron out of this technique, and these are the ones that make up the cube.

ii. For each tetrahedron, we have level set function values at the 4 corners. Find the unique plane that interpolates these values for each level set function. Thus each level set function is now approximated linearly by $Ax+By+Cz+D$. Now solve for (x, y, z) such that $Ax+By+Cz+D = 0$ (two equations here, one for each level set function). This is 2 equations, 3 unknowns linear system and we can solve for the line satisfying the system.

Fig. 2.15 explains how we obtain the zero level set planes from the implicit function. The intersection of the plane point in the edge connecting two grid points is calculated by once order linear approximation. This sounds to be less implicit as we use an explicit approximation, but in fact, this could not change the implicit function in all the grid points and the real zero level set embedded in the space.

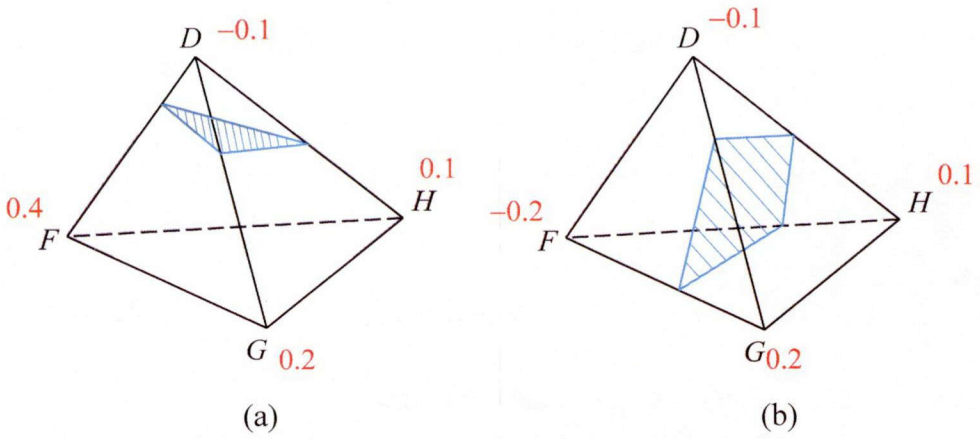

Fig. 2.15 Zero level set from the implicit function.

2.6 Numerical Results

In this section, examples of FMM and LSM are presented. Noticing that the FMM can create SDFs and also can be used for extending velocities, the LSM needs to be coupled with FMM for the cases that initial SDFs and/or the extended velocities are not available.

During the level set evolutions, we lay down a uniform grid over a two or three dimensional space and use the fifth order WENO finite difference scheme for all the spatial discretizations, while use the TVD-RK of third order for the time discretizations and set the associated CFL condition to be less than 0.5. We plot the zero-contour considered as the front of a level set function for codimension-one objects while call the three-dimensional visualization technique (introduced in Sec. 2.5.4) for codimension-two objects.

2.6.1 Creating Signed Distance Functions using Fast Marching Method

Creating Distance Functions from Target Points

We first consider a simple example: calculate the distance from any position $\boldsymbol{x}$ in two dimensions to a single target point arbitrarily distributed. The DF can be analytical represented by creating concentric circles with a uniform space in between. While for

the cases that more than one target point are distributed in space, the DF can only be obtained by numerical techniques of which we use FMM to get consistent and accurate results (see Fig. 2.16).

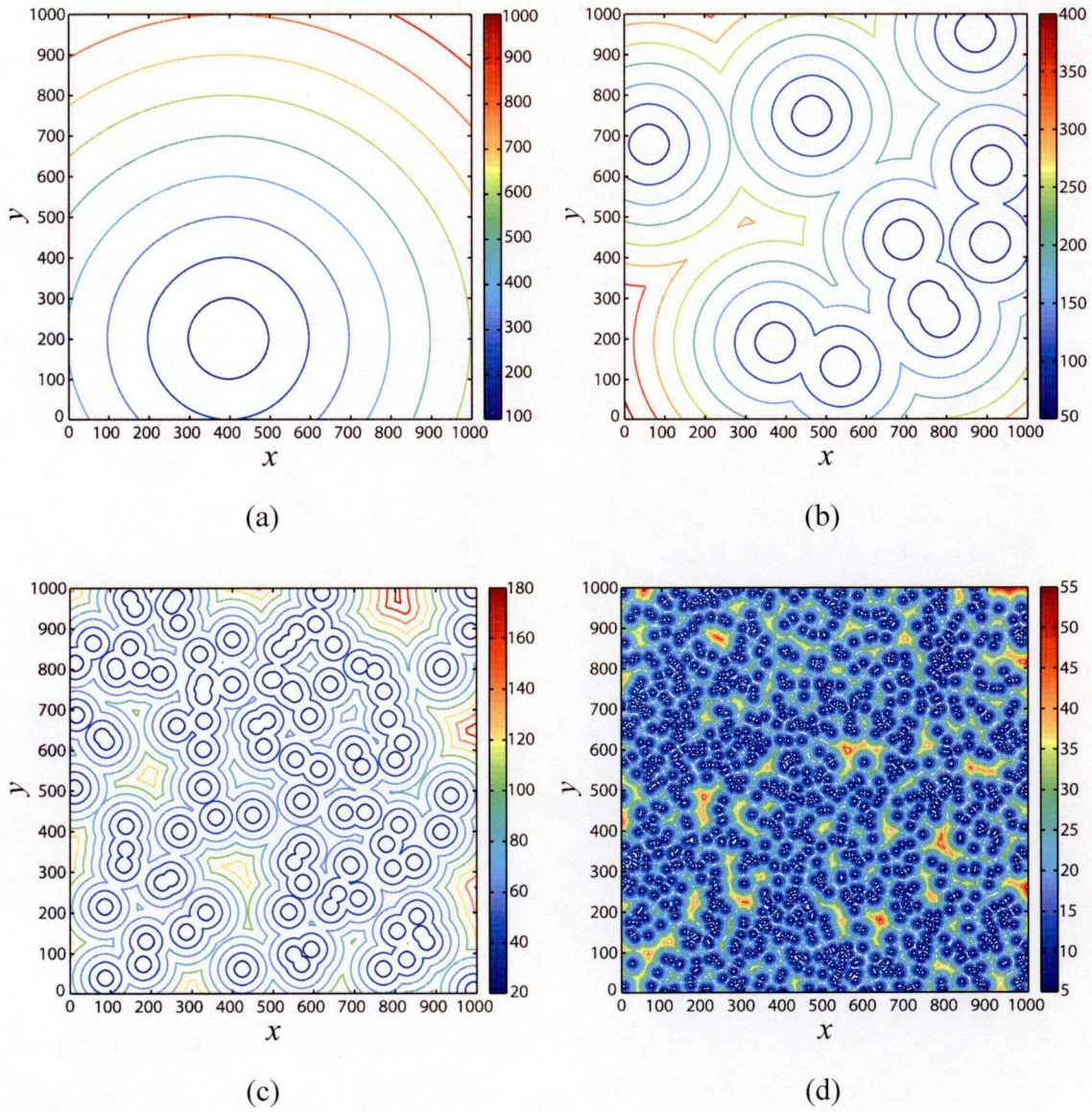

Fig. 2.16 Creating DFs from arbitrary distributed points.
Contours of the DF from (a) one target point. (b) 10 target points. (c) 10^2 target points. (d) 10^3 target points.

The contours are circles for one target point, while for multi-point situations, any position $\boldsymbol{x}$ on contours is corresponded to its nearest target point. With calling the fast sorting technique, FMM leads a very fast scheme for solving the Eikonal equation, and

thus creates DFs from target points efficiently. Noticing that the calculation time depends only on the number of mesh, the complexities for the cases Figs 2.16(a)-(d) do not obviously change.

Creating Signed Distance Functions from Non-Signed Distance Functions

With the usage of FMM, we can create a SDF from a non-SDF containing the interface of interest. During the calculation, only the information of interface is kept unchanged, which means the recalculated SDF preserves exactly the same interface as the initial non-SDF. Fig. 2.17 shows the example of creating a SDF from a circle function: $\phi(r) = (r^2 - 0.55^2)$ noticing that the contour with a marker point is the interface.

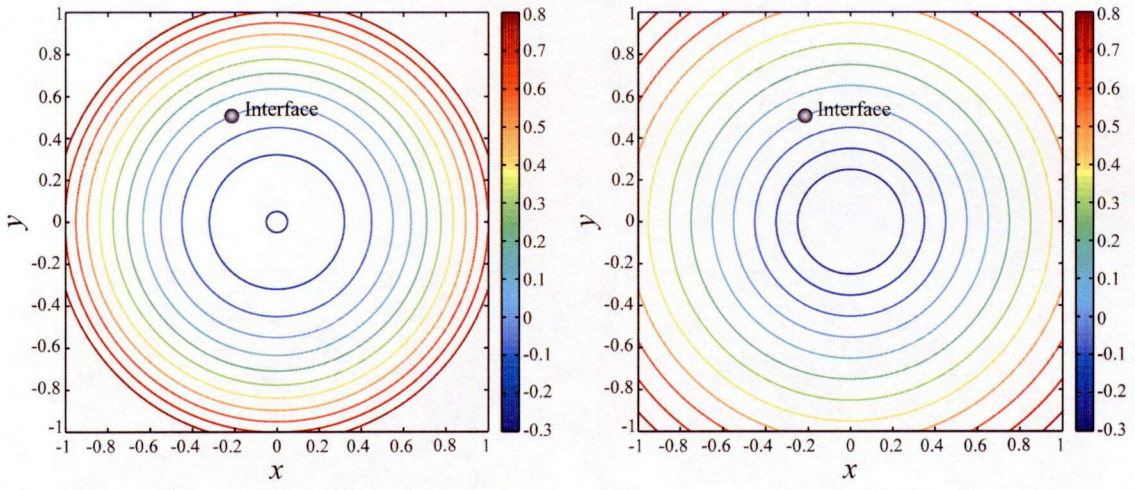

Fig. 2.17 Creating a SDF from a circle function: $\phi(r) = (r^2 - 0.55^2)$. (a) Contours of the initial non-SDF. (b) Contours of the recalculated SDF.

The contours of the recalculated SDF are concentric circles with a uniform space in between. The values inside the interface are negative while outside are positive.

The error norms (L_1 error, L_2 error and L_∞ error) of this recalculated SDF with the interface $\phi(r) = (r^2 - 0.55^2) = 0$ is investigated (see Table 2.1) and the result shows that our fast scheme gives a first-order accuracy.

Grid Points	L_1 error	L_2 error	L_∞ error
100×100	0.010330	0.009509	0.015224
200×200	0.005353	0.004734	0.009180

400×400	0.002817	0.002385	0.005462
800×800	0.001451	0.001180	0.003197
1600×1600	0.000762	0.000590	0.001835

Table 2.1 Error norms of the recalculated SDF with the interface: $\phi(r) = (r^2 - 0.55^2) = 0$.

We also create a SDF from a 'cauliflower' function: $\phi(r,\theta)=(r-0.5+0.1r\sin(8\theta))^3$ (see Fig. 2.18). The interface of interest can be of any shape and the contours of the recalculated SDF may not be just magnification or minification of the interface. One should be noted that FMM can create a SDF from not only an explicit function but also an implicit function containing interface of any shape and even multi-interface.

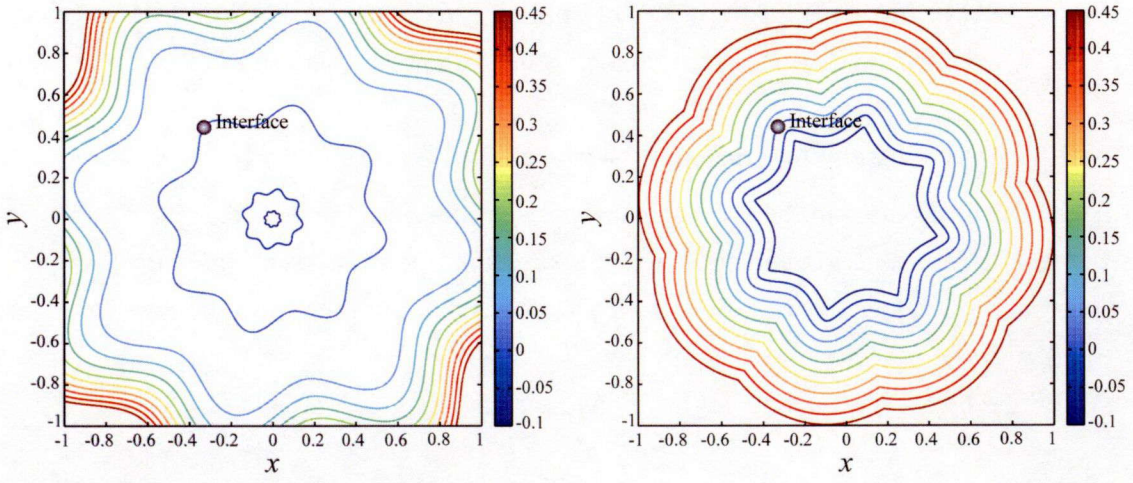

(a) (b)

Fig. 2.18 Creating a SDF from a 'cauliflower' function: $\phi(r,\theta) = (r-0.5+0.1r\sin(8\theta))^3$.
(a) Contours of the initial non-SDF. (b) Contours of the recalculated SDF.

Assembling Different Implicit Interfaces into One Signed Distance Function

Recalling that only the information of the interface is preserved, FMM can be used to assemble different interfaces into one SDF. Fig. 2.19 shows creating a SDF from 17 different implicit interfaces containing circles and cauliflowers.

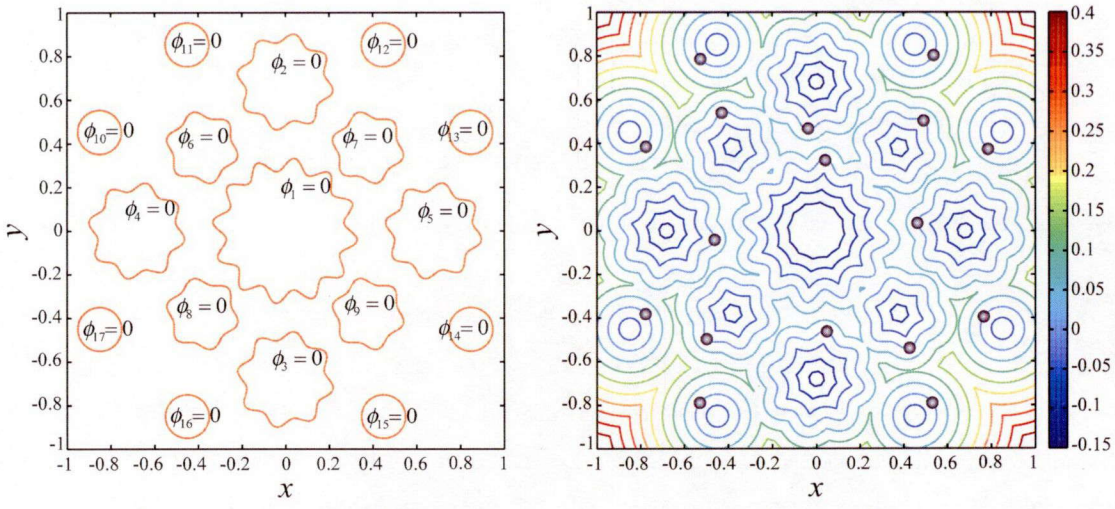

(a) (b)

Fig. 2.19 Creating a SDF from different implicit interfaces. (a) The initial 17 implicit interfaces. (b) The recalculated SDF with assembled interfaces.

The algorithm of assembling different interfaces is as follows:

(a) Tag the grid points in the *narrow band* of each individual interface.

(b) Create a new function and activate the *corresponding grids* (see Fig 2.20(a)).

(c) Extract the values of grid points found from (a) and put them into the *corresponding grids* of the new function.

(d) Run the FMM routine and get the signed distance (see Fig. 2.20(b)).

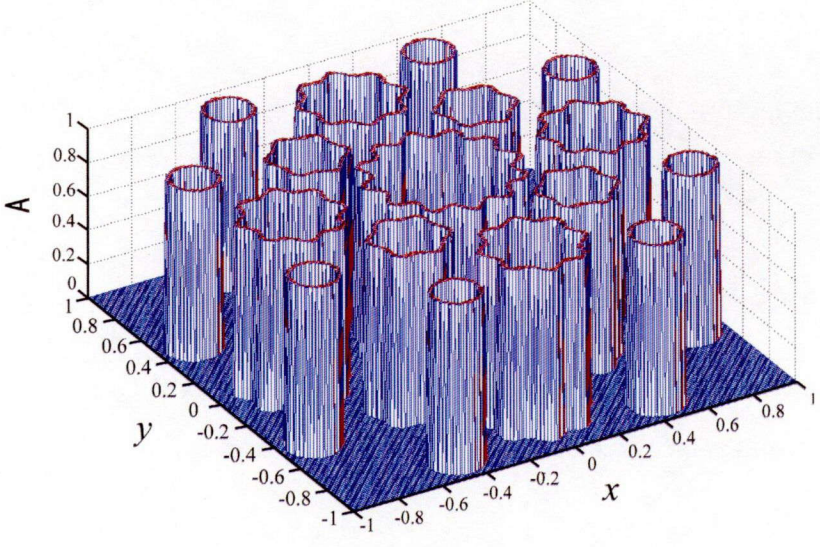

(a)

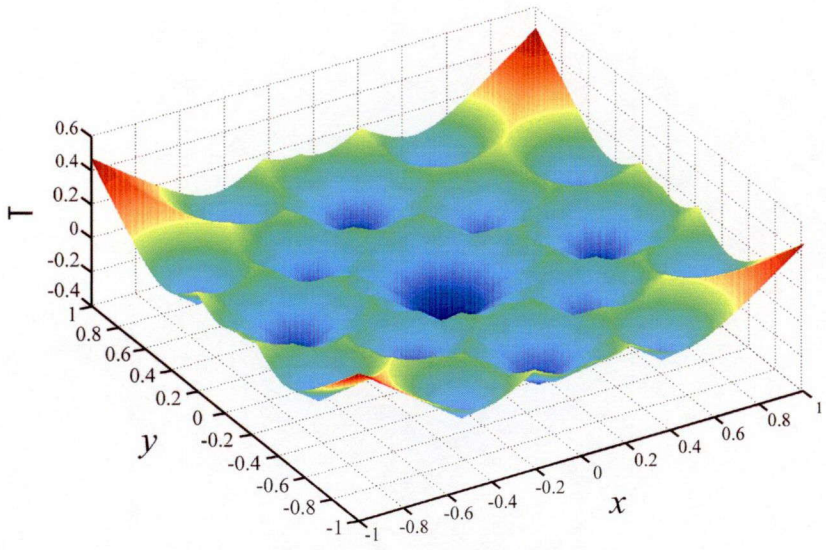

(b)

Fig. 2.20 Assembling different implicit interfaces into one SDF (a) Grid points of interest from 17 individual interfaces. (b) Signed distance value from the interfaces.

2.6.2 The Level Set Evolution of Implicit Interfaces

Merging of Loops under the Normal Vector

We first create a SDF ϕ containing four circles with clockwise orientation (see Fig 2.21(a)) as the initial function for level set evolution. This SDF is calculated by the technique of FMM mentioned in the previous subsection. The evolution equation under the normal vector takes the form

$$\phi_t + \boldsymbol{N} \cdot \nabla \phi = 0 \quad , \tag{2.44}$$

and the evolution of these four loops is shown from Fig. 2.21.

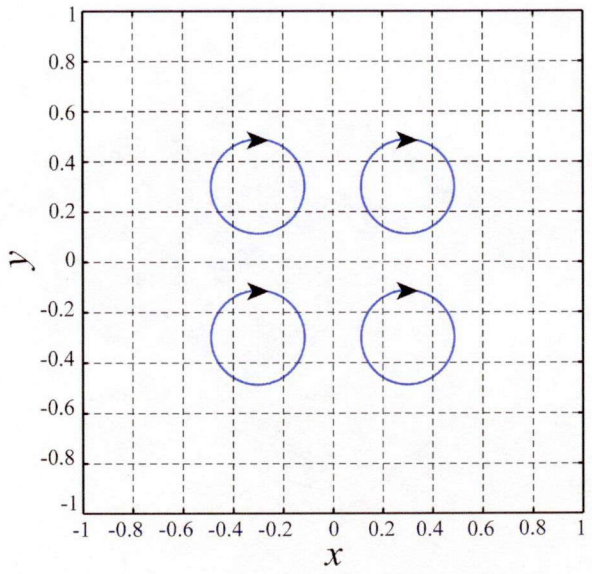

(a) $t = 0$

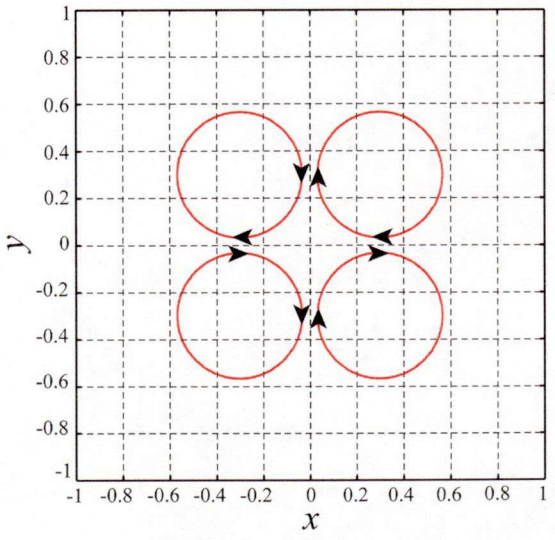

(b) $t = 0.08$

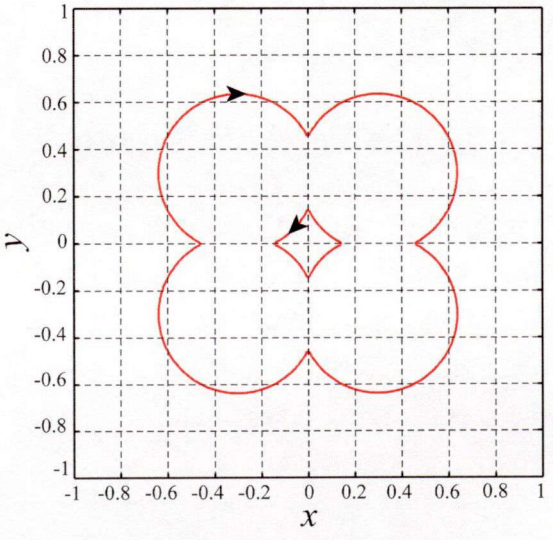

(c) $t = 0.15$

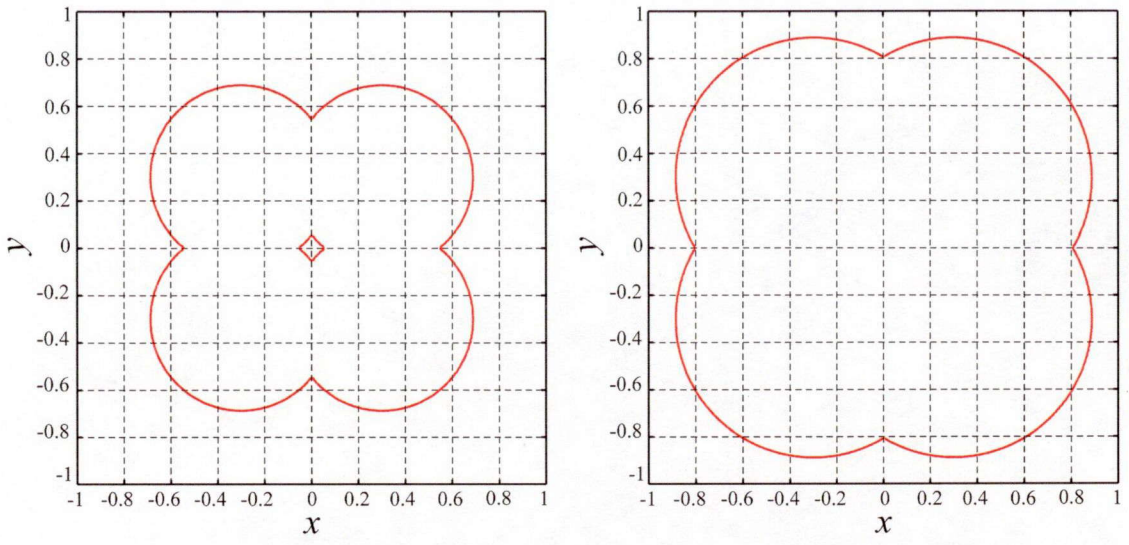

(d) $t = 0.20$ (e) $t = 0.40$

Fig. 2.21 Merging of four loops under the normal vector.

Firstly, the four loops extend under the normal vector of the front and get close to each other. When the segments with opposite orientations meet (see Fig. 2.21(b)), these segments are annihilated and the loops break on these points. Thus the initial four loops turn to be two loops with a large loop still preserving clockwise orientation and a small loop with the counterclockwise orientation (see Fig. 2.21(c)). The outer large loop keeps on enlarging while the inner small loop shrinks (see Fig. 2.21(d))) and finally the small loop disappears (see Fig. 2.21(e)).

2.6.3 Modeling Curve Evolution in Three Dimensions

Helix Shrinking under the Curvature Times Normal Vector

We first create two level set functions ϕ and ψ of which the zero isosurfaces (codimension-one interfaces) are two sine hypersurfaces (see Fig. 22(a)). Then we can get the helical intersection (codimension-two curve) from the two hypersurfaces (see Fig. 22(b)).

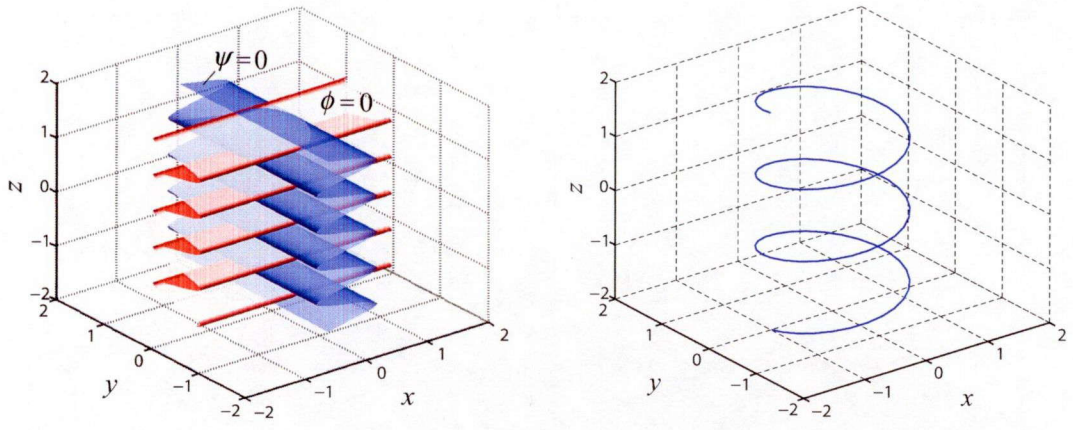

Fig. 2.22 Creating the initial level set functions (t = 0). (a) The initial two hypersurfaces. (b) Intersection of these two hypersurfaces.

The evolution equations for curvature motion of a helix in three dimensions take the form [74]

$$\begin{aligned} \phi_t + \kappa \boldsymbol{N} \cdot \nabla \phi = 0 \\ \psi_t + \kappa \boldsymbol{N} \cdot \nabla \psi = 0 \end{aligned} \quad . \tag{2.45}$$

From Eq. (2.45), we can see that although the intersection is the object we intend to deal with, two level set functions ϕ and ψ in the whole region need to be involved during the calculation of the evolution.

Fig. 2.23 shows the helix evolving under the curvature times normal vector in three dimensions. The curve remains helical in form during the evolution but the radius r about the center axis shrinks by a speed of $1/r$, in which case the straightening of the helix accelerated during the radius shrinking.

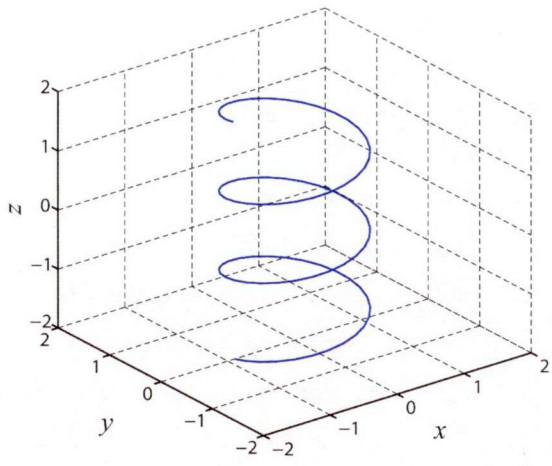

(a) $t = 0.10$

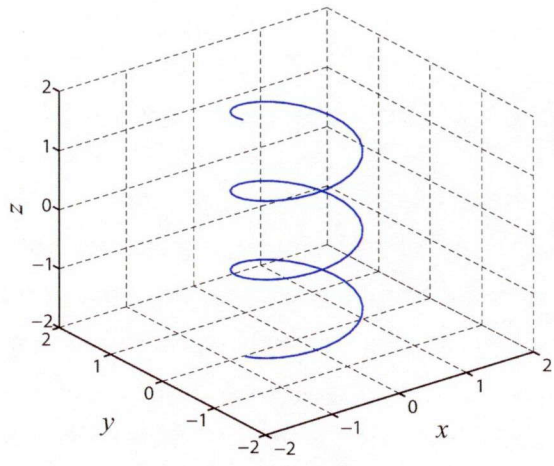

(b) $t = 0.20$

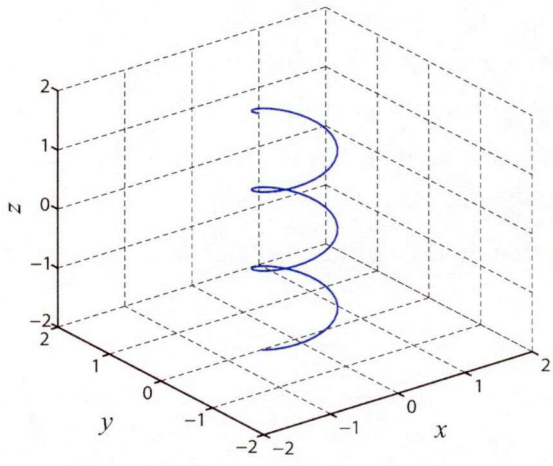

(c) $t = 0.40$

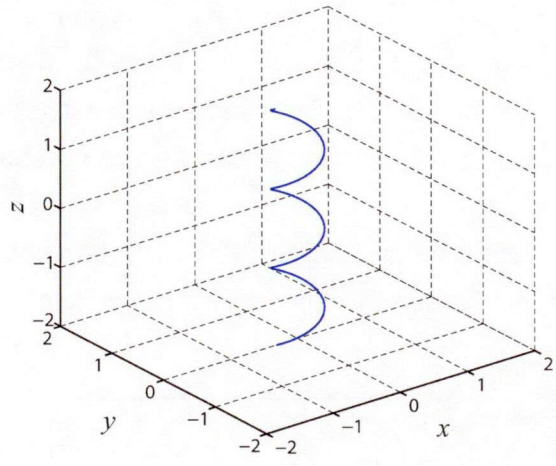

(d) $t = 0.50$

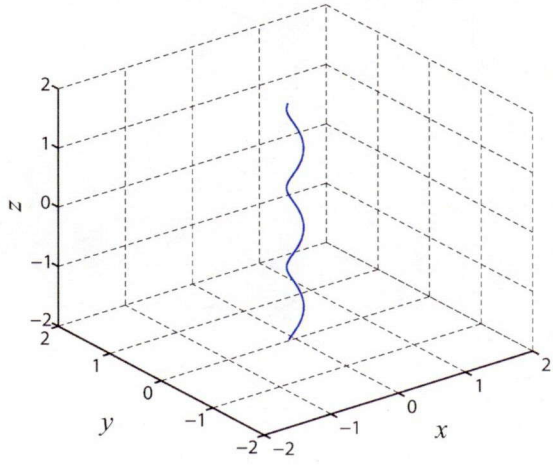

(e) $t = 0.60$

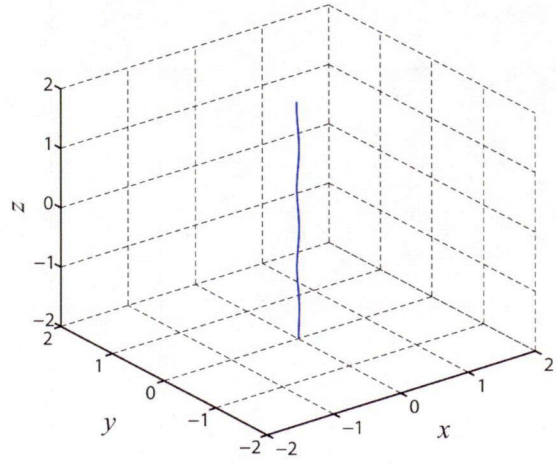

(f) $t = 0.70$

Fig. 2.23 Helix shrinking under the curvature times normal vector.

2.6.4 The Velocity Extension for the Level Set Evolution

For an interface moving problem, the key quantity needs to be determined is the velocity field of the interface. For some cases, the velocity field can be passively obtained from the geometric quantities of all the levels in which the interface is embedded, while for others, the velocity is locally computed on the interface and is not analytical expressed away from the interface. A reinitialization process is induced to keep the implicit level set function be a SDF but the process itself still leads to some additional diffusive error. We introduce the technique of FMM for extending velocities, and compare with the case without extending the front velocity.

Suppose a line in a two dimensional region gliding from left to right under a unit speed (see Fig. 2.24(a)), all the level sets are at first moving smoothly since the velocities defined on different levels are of uniform (we draw three contours including the front: blue(-Δh contour), green(0 contour) and red(Δh contour)). Then the gliding line meets a circular impenetrable particle with the radius R = 0.15 located in (0 0 0) (see the orange circle of Fig. 2.24(a)), in which case, the line should stop gliding rightward on the interface of the particle.

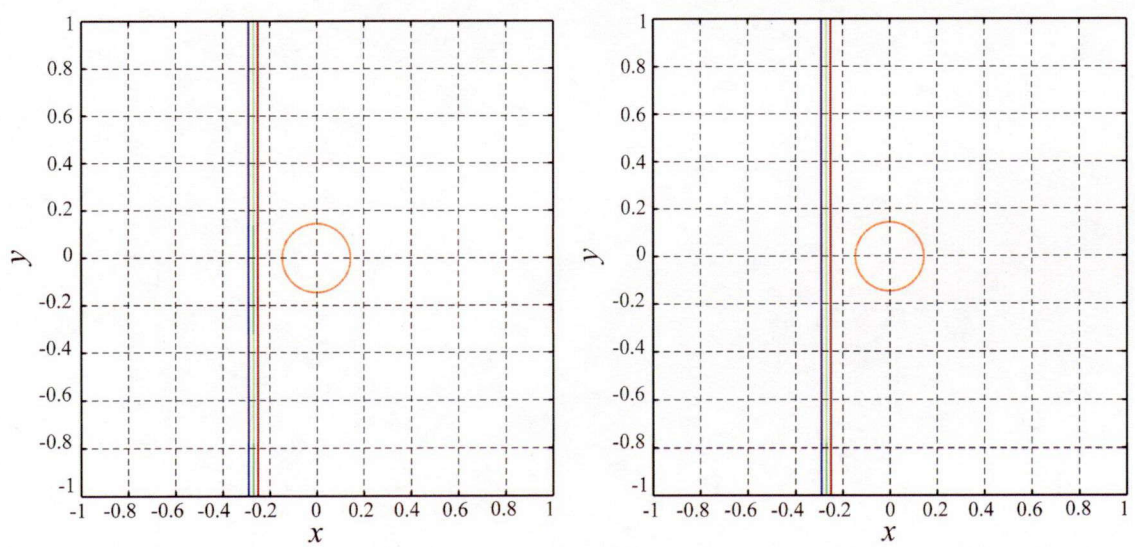

(a) $t = 0$

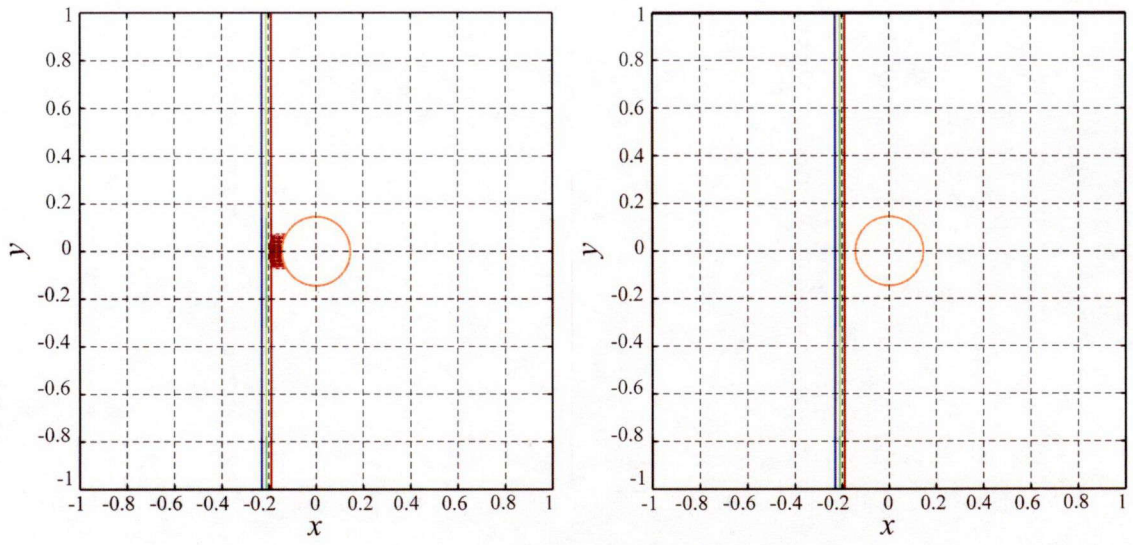
y
x
1
0.8
0.6
0.4
0.2
0
-0.2
-0.4
-0.6
-0.8
-1
-1 -0.8 -0.6 -0.4 -0.2 0 0.2 0.4 0.6 0.8 1

(b) $t = 0.06$

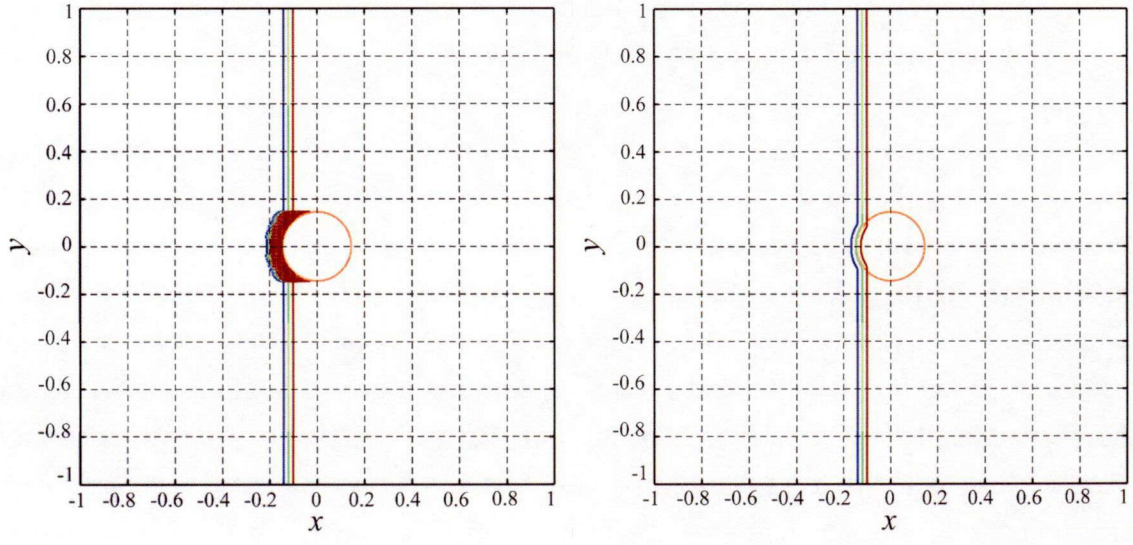
y
x
1
0.8
0.6
0.4
0.2
0
-0.2
-0.4
-0.6
-0.8
-1
-1 -0.8 -0.6 -0.4 -0.2 0 0.2 0.4 0.6 0.8 1

(c) $t = 0.15$

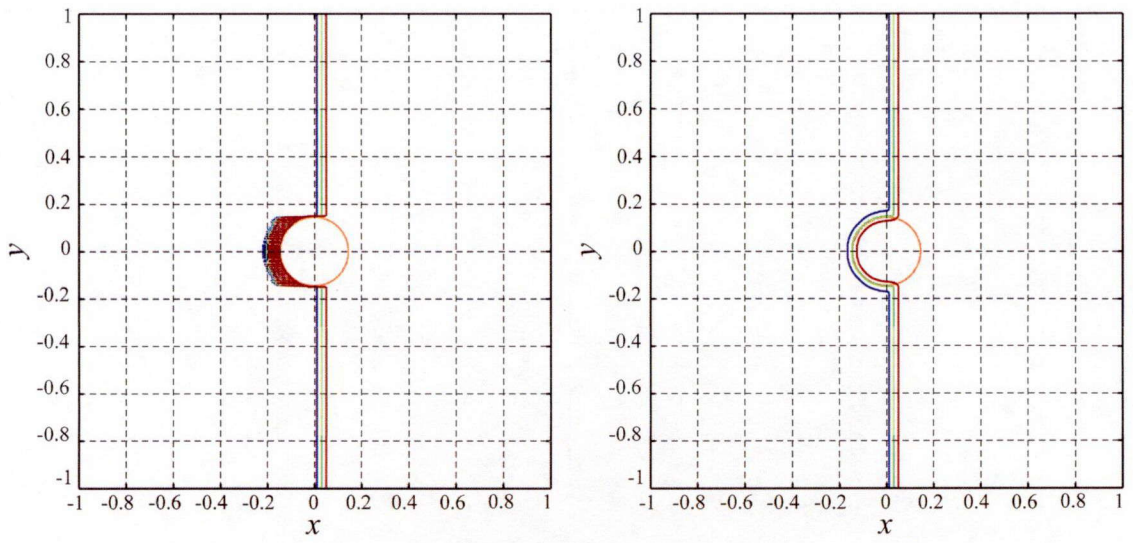

(d) $t = 0.30$

Fig. 2.24 A gliding line bypassing an impenetrable particle (left column: evolution without extension velocity; right column: evolution with extension velocity).

As we can see from Fig. 2.24(b)-(d), without velocity extension, the levels in front of the zero level in the orange circular region first stop before the zero level meets with the particle. As a consequence, these levels pile up and we could not get proper finite schemes for PDEs which use the neighboring points of the zero level. On the other hand, with the velocity extension, the velocity on all the other levels are recalculated according to the zero level set and we can get a beautiful evolution of the line bypassing an impenetrable particle. In Fig. 2.25, we draw out the contours of the two cases from Fig. 2.24(d), and the result of Fig. 2.25(b) shows that all the levels are uniformly distributed even the velocity of the interface is dramatically changed.

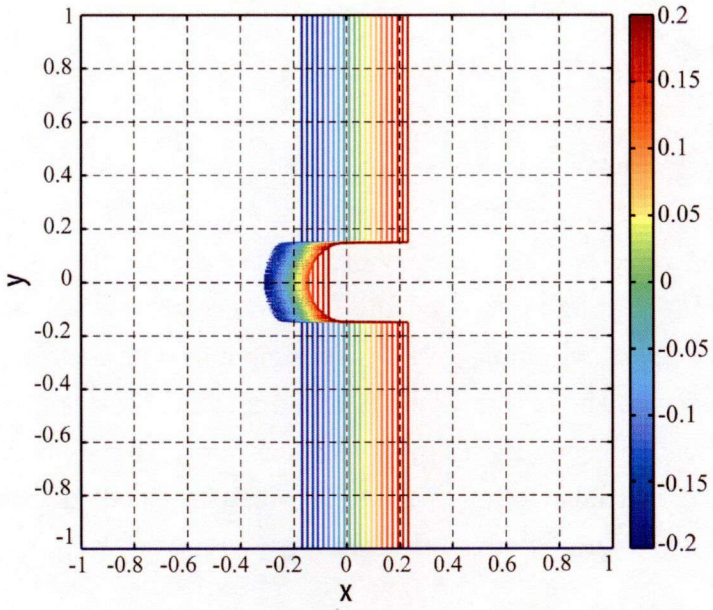

(a)

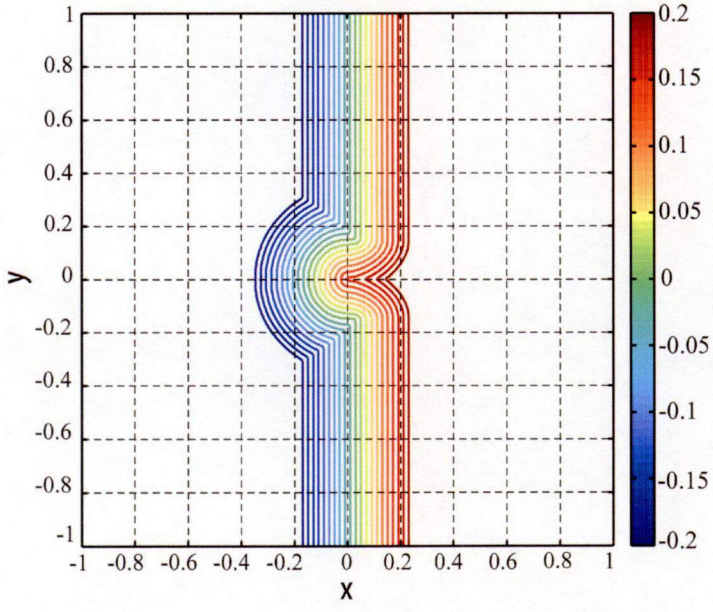

(b)

Fig. 2.25 Comparing the two cases of the gliding line bypassing an impenetrable particle. (a) Contours of Fig. 2.24(d) without the extension velocity. (b) Contours of Fig. 2.24(d) with the extension velocity.

2.7 Conclusion

We have shown the level set evolutions coupled with FMM creating accurate and consistent SDFs as the initial level set functions for the LSM and also used for the velocity extension when only the velocity of the front can be determined. Uniform grid points are created for easing high order finite difference scheme constructions, and thus we can present complex evolutions of level set functions and move a curve in a variety of flows. We have also shown the level set based method for representing and moving higher codimensional objects: curves in three dimensions. As shown from the numerical results, the topological changes of the interface can be handled naturally, especially when merging and breaking of the curve occur.

Chapter 3

Micromechanics of Defects and Level Set Method for Dislocation Dynamics

3.1 Abstract

Computational simulation of dislocation dynamics could generally be divided into atomistic and continuum models or even hybrid atomistic-continuum if strictly differentiated [5]. Although the application of atomistic simulation has specific aspect which could demonstrate collective behavior of atoms in crystal populated by dislocations, continuum theory can analyze the dislocation behavior over long range and real time scales. In this chapter, examples of dislocations dynamics are approached including edge dislocation climb, dislocation evolution under applied stress and dislocation interactions. In the plastic deformation of distorted solids, the line defects, which can be regarded as the atomistic topological change of the lattice alignment, evolve dramatically due to the given Peach-Koehler force [19]. This kind of mechanism has so far been analyzed by using discrete dislocation dynamics (DDD) which can revive the evolution of the dislocation loops properly but is extremely complicated and time-consuming. Since the level set method does not need to track individual dislocation line segment of all dislocation lines directly, it can demonstrate the variable topological changes in an easier form as one of the prospective computational modeling for defect mechanics.

This chapter is organized as follows. In Section 3.2, a basic conception of micromechanics of defects is introduced and the equation of internal stress field from dislocation periodically distributed in a Fourier transformed form is deduced. In Section 3.3, some numerical implementations to level set method for dislocation dynamics are

explained with the outline of the algorithm. In Section 3.4, we present some applications of level set dislocation dynamics as a preparing for the following chapters.

3.2 Theory of Dislocation Elasticity

In this section, we briefly introduce the continuum theory of elasticity. Fig. 3.1 shows a single lattice layer containing an edge dislocation with Burgers vector $\boldsymbol{b}$ [18-21].

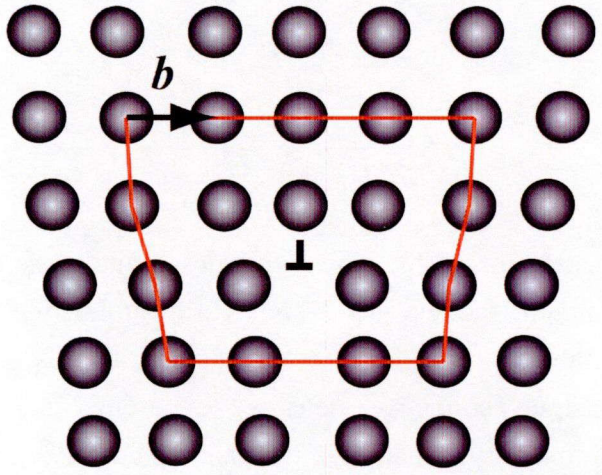

Fig. 3.1 Edge dislocation with Burgers vector $\boldsymbol{b}$.

Dislocation originated from displacement of crystal is regarded as continuous medium, which means displacement should preserve continuity. And because of this, the whole story begins with the displacement vector. After a passage around any closed contour L enclosing the dislocation line D, the elastic displacement vector $\boldsymbol{u}$ receives a certain finite increment b which is equal to the lattice vector in magnitude and direction,

$$\oint_L \mathrm{d}u_i = \oint_L \frac{\partial u_i}{\partial x_k}\mathrm{d}x_k = b_i \quad , \tag{3.1}$$

where $i,k = 1,2,3$ or indicial notation of tensor algebra. Distortion tensor $\boldsymbol{w}$ is defined by displacement vector $\boldsymbol{u}$,

$$w_{ij} = \frac{\partial u_j}{\partial x_i} \quad . \tag{3.2}$$

Substituting Eq. (3.2) to Eq. (3.1), we can get

$$\oint_L w_{ki} \mathrm{d}x_k = b_i \quad . \tag{3.3}$$

Using Stokes's theorem, Eq. (3.3) can be written as

$$\oint_L w_{ki} \mathrm{d}x_k = \int_S (\nabla \times \boldsymbol{w})_{ki} n_k \mathrm{d}S \quad , \tag{3.4}$$

where n_k is component of unit vector $\boldsymbol{n}$ normal to surface S which is an arbitrary surface spanning the closed line L. Since the rotation of the second-order tensor $\boldsymbol{w}$ can be written as

$$(\nabla \times \boldsymbol{w})_{ki} = e_{ipq} w_{kq,p} \quad , \tag{3.5}$$

where e_{ijk} is permutation tensor which is an anti-symmetrical in the suffixes j and k and the tensor $w_{ki,j} = u_{i,kj}$ is symmetrical according to suffixes k and j. The integrand of Eq. (3.4) is identically zero everywhere except meeting the plane which contains singularities, and the right-hand of Eq. (3.3) can be written as

$$b_i = b_i \int_S \delta(\gamma) \xi_k n_k \mathrm{d}S \quad , \tag{3.6}$$

where ξ is the unit tangent vector of dislocation line and $\delta(\gamma)$ is the delta function equaling to one when the infinitesimal plane dS meets singularity and zero otherwise. Thus we get the relationship using Eqs. (3.4) and (3.6):

$$(\nabla \times \boldsymbol{w})_{ki} = b_i \delta(\gamma) \xi_k \quad . \tag{3.7}$$

From Eq. (3.5), we know that

$$e_{ijm} w_{km,j} = b_i \delta(\gamma) \xi_k \quad . \tag{3.8}$$

We concentrate on stain and stress associated with dislocation displacement. First, define the infinitesimal strain tensor as the average of two distortions with the opposite suffixes:

$$\varepsilon_{ij} = \frac{1}{2}(w_{ij} + w_{ji}) \quad . \tag{3.9}$$

The stress tensor is determined from strain tensor by linear elastic constitutive equation, that is, Hookes's law as

$$\sigma_{ij} = C_{ijkl} \varepsilon^{\mathrm{e}}_{kl} = C_{ijkl} (\varepsilon_{kl} - \varepsilon^*_{kl}) \quad , \tag{3.10}$$

where the forth-order tensor C_{ijkl} is the elastic constant tensor and has the property of symmetry; ε^{e} is elastic strain and ε^* is eigenstrain. For an isotropic medium, Eq. (3.10) can be written as

$$\sigma_{ij} = 2\mu\varepsilon_{ij} + \lambda\varepsilon_{kk}\delta_{ij} \quad , \tag{3.11}$$

where Kronecker delta notation δ_{ij} equals to 1 when $i=j$ and 0 otherwise. In the absence of body force, the equilibrium equation is simply

$$\sigma_{ij,j} = 0 \quad . \tag{3.12}$$

Substitute Eqs. (3.2), (3.9) and (3.10) into Eq. (3.12), recalling that C_{ijkl} is symmetric, and we get

$$C_{ijkl}u_{k,lj} = C_{ijkl}\varepsilon^*_{kl,j} \quad , \tag{3.13}$$

Suppose $\varepsilon^*_{ij}(\boldsymbol{x})$ is given in the form of a single wave of amplitude $\tilde{\varepsilon}^*_{ij}(\boldsymbol{k})$, where $\boldsymbol{k}$ is the wave vector

$$\varepsilon^*_{ij}(\boldsymbol{x}) = \tilde{\varepsilon}^*_{ij}(\boldsymbol{k})\exp(i\boldsymbol{kx}) \quad . \tag{3.14}$$

Similarly, $u^*_i(\boldsymbol{x})$ can be written as

$$u^*_i(\boldsymbol{x}) = \tilde{u}^*_i(\boldsymbol{k})\exp(i\boldsymbol{kx}) \quad . \tag{3.15}$$

Substitute Eqs. (3.14) and (3.15) into (3.13), and we have

$$C_{ijkl}\tilde{u}_k(\boldsymbol{k})k_l k_j = C_{ijkl}\tilde{\varepsilon}^*_{kl}(\boldsymbol{k})k_j \quad , \tag{3.16}$$

where in the derivation $(i\boldsymbol{kx})_{,l} = ik_l$ is used. Using the notation

$$M_{ik}(\boldsymbol{k}) = C_{ijkl}k_j k_l \quad , \tag{3.17}$$

$$X_i = -iC_{ijkl}\tilde{\varepsilon}^*_{kl}k_j \quad , \tag{3.18}$$

we can get

$$\tilde{u}_i(\boldsymbol{k}) = X_j N_{ij}(\boldsymbol{k})D(\boldsymbol{k}) \quad , \tag{3.19}$$

where D and N_{ij} are written as

$$D(\xi) = e_{mnl}M_{m1}M_{n2}M_{l3} \quad , \tag{3.20}$$

$$N_{ij}(\xi) = \frac{1}{2}e_{ikl}e_{jmn}M_{km}M_{ln} \quad . \tag{3.21}$$

Finally, combining Eqs. (3.8), (3.9), (3.11) and (3.19) with defining the relationship $\xi_i\delta(\gamma)=d_i(\boldsymbol{k})\exp(i\boldsymbol{kx})$, we can deduce the isotropic elastic stress field which is associated with dislocation and takes the form of Fourier transform to its real coordinate under the periodic boundary condition, as shown in Fig. 3.2 [75]:

$$\tilde{\sigma}_{11} = 2\mu i(\frac{1}{k_1^2+k_2^2+k_3^2}(k_2b_3-k_3b_2)\tilde{d}_1 - \frac{1}{1-\nu}\frac{k_2^2+k_3^2}{(k_1^2+k_2^2+k_3^2)^2}[(k_2b_3-k_3b_2)\tilde{d}_1+(k_3b_1-k_1b_3)\tilde{d}_2+(k_1b_2-k_2b_1)\tilde{d}_3])$$

$$\tilde{\sigma}_{22} = 2\mu i(\frac{1}{k_1^2+k_2^2+k_3^2}(k_3b_1-k_1b_3)\tilde{d}_2 - \frac{1}{1-\nu}\frac{k_1^2+k_3^2}{(k_1^2+k_2^2+k_3^2)^2}[(k_2b_3-k_3b_2)\tilde{d}_1+(k_3b_1-k_1b_3)\tilde{d}_2+(k_1b_2-k_2b_1)\tilde{d}_3])$$

$$\tilde{\sigma}_{33} = 2\mu i(\frac{1}{k_1^2+k_2^2+k_3^2}(k_1b_2-k_2b_1)\tilde{d}_3 - \frac{1}{1-\nu}\frac{k_1^2+k_2^2}{(k_1^2+k_2^2+k_3^2)^2}[(k_2b_3-k_3b_2)\tilde{d}_1+(k_3b_1-k_1b_3)\tilde{d}_2+(k_1b_2-k_2b_1)\tilde{d}_3])$$

$$\tilde{\sigma}_{12} = \tilde{\sigma}_{21} = 2\mu i(\frac{1}{2(k_1^2+k_2^2+k_3^2)}[(k_3b_1-k_1b_3)\tilde{d}_1+(k_2b_3-k_3b_2)\tilde{d}_2]+\frac{1}{1-\nu}\frac{k_1k_2}{(k_1^2+k_2^2+k_3^2)^2}[(k_2b_3-k_3b_2)\tilde{d}_1+(k_3b_1-k_1b_3)\tilde{d}_2+(k_1b_2-k_2b_1)\tilde{d}_3])$$

$$\tilde{\sigma}_{23} = \tilde{\sigma}_{32} = 2\mu i(\frac{1}{2(k_1^2+k_2^2+k_3^2)}[(k_1b_2-k_2b_1)\tilde{d}_2+(k_3b_1-k_1b_3)\tilde{d}_3]+\frac{1}{1-\nu}\frac{k_2k_3}{(k_1^2+k_2^2+k_3^2)^2}[(k_2b_3-k_3b_2)\tilde{d}_1+(k_3b_1-k_1b_3)\tilde{d}_2+(k_1b_2-k_2b_1)\tilde{d}_3])$$

$$\tilde{\sigma}_{13} = \tilde{\sigma}_{31} = 2\mu i(\frac{1}{2(k_1^2+k_2^2+k_3^2)}[(k_1b_2-k_2b_1)\tilde{d}_1+(k_2b_3-k_3b_2)\tilde{d}_3]+\frac{1}{1-\nu}\frac{k_1k_3}{(k_1^2+k_2^2+k_3^2)^2}[(k_2b_3-k_3b_2)\tilde{d}_1+(k_3b_1-k_1b_3)\tilde{d}_2+(k_1b_2-k_2b_1)\tilde{d}_3])$$

(3.22)

Fourier transform assumes the periodic boundary condition with a prime cell and infinite image cells [76, 77] (see Fig. 3.2).

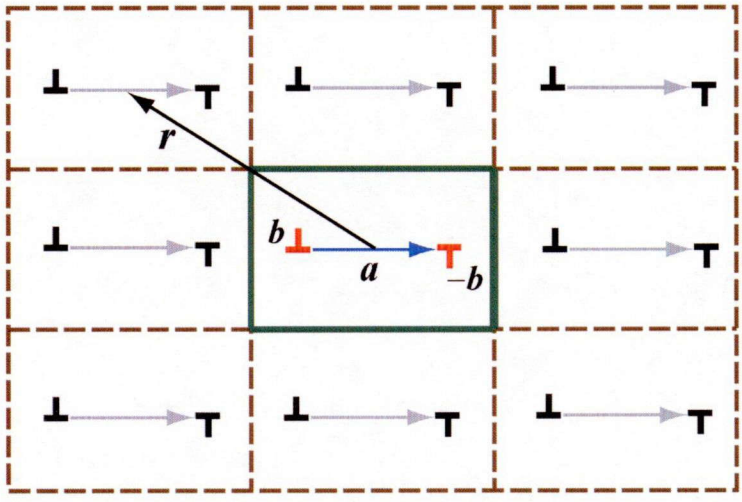

Fig. 3.2 Periodic simulation cell with dipole dislocations [76].

The dark green framed cell in the middle is the prime cell with dipole dislocations and the dashed line cells are image cells. Because of the periodicity of the boundary, the total elastic field in the prime cell contains the superposition of elastic field from all the other image cells infinitely extending.

The force which acts on dislocations is called Peach-Koehler force defined as

$$\boldsymbol{f} = (\boldsymbol{\sigma}^{\text{tot}} \cdot \boldsymbol{b}) \times \boldsymbol{\xi} \quad , \tag{3.23}$$

where the total stress $\boldsymbol{\sigma}^{\text{tot}}$ includes applied stress $\boldsymbol{\sigma}^{\text{app}}$ and internal stress $\boldsymbol{\sigma}^{\text{int}}$ caused by singularities;

$$\sigma^{\text{tot}} = \sigma^{\text{app}} + \sigma^{\text{int}} \quad . \tag{3.24}$$

And the Eq. (3.23) can be written as

$$f_i = e_{mni}\sigma^{\text{tot}}_{mk} b_k \xi_n \quad . \tag{3.25}$$

Dislocation can move conservatively (without diffusion) in the plane containing both its tangent vector and Burgers vector under the Peach-Koehler force of Eq. (3.25). At a high temperature, edge dislocations may move out of the slip plane by a non-conservative process, called climbing. Some models of dislocation dynamics are given in Sec. 3.4.

3.3 Implementations to Level Set Dislocation Dynamics

3.3.1 Mobility Tensor

The dislocation velocity is defined by

$$\boldsymbol{v} = \boldsymbol{M} \cdot \boldsymbol{f} \quad , \tag{3.26}$$

where $\boldsymbol{f}$ is Peach-Koehler force of Eq. (3.25) and $\boldsymbol{M}$ is the mobility tensor defined as [75, 78, 79]

$$\boldsymbol{M} = \begin{cases} m_g(\boldsymbol{I} - \boldsymbol{n} \otimes \boldsymbol{n}) + m_c \boldsymbol{n} \otimes \boldsymbol{n} & \text{(edge dislocation)} \\ m_g \boldsymbol{I} & \text{(screw dislocation)} \end{cases} , \tag{3.27}$$

where the term $\boldsymbol{I} - \boldsymbol{n} \otimes \boldsymbol{n}$ in the mobility tensor projects the velocity of an edge dislocation to its slip plane since edge dislocation can only glide in the self slip plane in the case that climb mobility is not considered. The m_g is glide mobility constant and m_c is climb mobility constant, $\boldsymbol{I}$ is identity matrix and $\boldsymbol{n}$ is normal vector of the slip plane that can be obtained as

$$\boldsymbol{n} = \frac{\xi \times \boldsymbol{b}}{|\xi \times \boldsymbol{b}|} \quad , \tag{3.28}$$

where ξ is the tangent vector of the dislocation written as the form of two level set functions ϕ and ψ;

$$\xi = \frac{\nabla\phi \times \nabla\psi}{|\nabla\phi \times \nabla\psi|} \quad . \tag{3.29}$$

For preventing singularity, we regularize the Eq. (3.29) as

$$\xi = \frac{\nabla\phi \times \nabla\psi}{\sqrt{\left|\nabla\phi \times \nabla\psi\right|^2 + \mathrm{d}x^2}} \quad . \tag{3.30}$$

The delta function first mentioned in Eq. (3.6) is given by

$$\delta(\gamma) = \delta(\phi)\delta(\psi) \quad . \tag{3.31}$$

The left side of Eq. (3.31) is a one-dimensional smear function defined as

$$\delta(x) = \begin{cases} \frac{1}{2\varepsilon}(1 + \cos\frac{\pi x}{\varepsilon}) & -\varepsilon \le x \le \varepsilon \\ 0 & \text{otherwise} \end{cases} \quad . \tag{3.32}$$

This smear function turns the pulse function into a continuous wave. We normally set the mobility ration of m_c and m_g to be

$$0 \le \frac{m_c}{m_g} \le 1 \quad . \tag{3.33}$$

3.3.2 Velocity Interpolation

For a normal level set function, the velocity could be defined for each of the level set [80, 81]. When added physical meaning, velocity could only be acquired from the zero level set. To define the other level sets' velocities, several approaches have been applied, Rhee *et al.* [82] used an underlying elliptic PDE coupled to a source term along the interface; Malladi *et al.* [83] introduced the idea of extrapolating the velocity at the closest point on the front; Sethian and Strain [84] defined the velocity at the interface depended on a jump condition across the interface; a speed function from the front Γ using some less physical quantity also be considerable. For the case of a three-dimensional curve, the real meaningful velocity is only the intersection of the two zero level set functions, which makes the problem much more complicated. According to Xiang Yang *et al.* [75, 78, 79], they first approximated the velocity of intersection points from grid points and then employed fast marching method (FMM) or fast sweeping technique (FSM) to update velocity of all the grids by the extension method.

For any grid point, the dislocation line segments in its nearby cubes are first found by the plotting method. For example, point C (grid point of interest) in Fig. 3.3, the distance from C to dislocation segment EF is the minimum distance from grid to

dislocation. We compute the velocities on E and F, find the location of G and interpolate the velocity on G from E and F. The velocity on C is approximated as that on G.

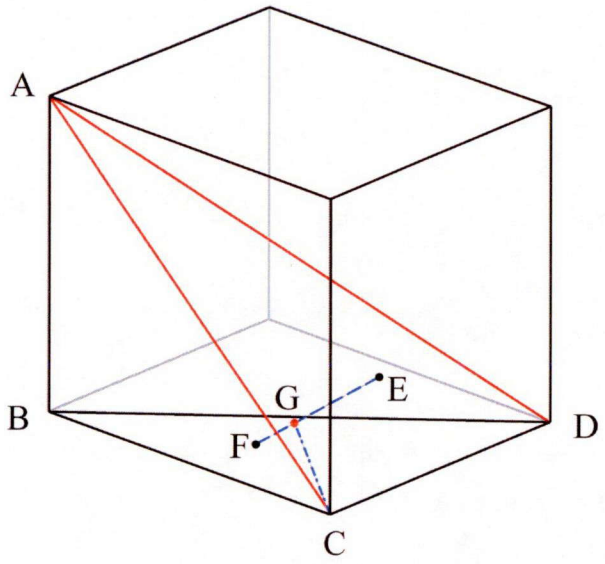

Fig. 3.3 A cubic of simulation grids.

The trilinear interpolation of velocity is defined from the eight neighboring grids as

$$v(x,y,z)=\frac{1}{8}\sum_{l_1,l_2,l_3=0}^{1} v_{i+l_1,j+l_2,k+l_3}\,\overline{x}_{l_1}\overline{y}_{l_2}\overline{z}_{l_3} \quad . \tag{3.34}$$

Assume that we have grid points $(x_{i+l_1}, y_{j+l_2}, z_{k+l_3})$ and the velocity $v_{i+l_1,j+l_2,k+l_3}$ on them, where l_1, l_2, l_3 = 0 or 1 for the neighboring grid points. In Eq. (3.26), the $\overline{x}_{l_1}$, $\overline{y}_{l_1}$ and $\overline{z}_{l_1}$ are defined as

$$\begin{aligned}
\overline{x}_{l_1} &= 1+(2l_1-1)\left(\frac{2(x-x_i)}{\mathrm{d}x}-1\right)\\
\overline{y}_{l_1} &= 1+(2l_2-1)\left(\frac{2(y-y_i)}{\mathrm{d}y}-1\right) \quad .\\
\overline{z}_{l_1} &= 1+(2l_3-1)\left(\frac{2(z-z_i)}{\mathrm{d}z}-1\right)
\end{aligned} \tag{3.35}$$

Then this velocity is extended to the whole space associated with the FMM or FSM to make sure the new calculated velocity satisfies Eq. (2.26) [85-87].

3.3.3 Outline of Algorithm

Step I: Initialize two level set functions ϕ and ψ both of which are SDFs as the initial functions.

Step II: Compute the tangent vector ξ and the delta function $\delta(\gamma)$ from Eqs. (3.29) and (3.31).

Step III: Compute the internal stress tensor $\tilde{\sigma}$ using Eq. (3.22) and an inverse Fourier transform.

Step IV: Compute the Peach-Koehler force $\boldsymbol{f}$ from Eqs. (3.23)-(3.24) and velocity field $\boldsymbol{v}$ using Eq. (3.26).

Step V: Perform velocity interpolation and extension introduced in Sec. 3.3.2.

Step VI: Evolve level set functions ϕ and ψ using Eq. (2.19).

Step VII: Reinitialize ϕ and ψ as explained in Sec 2.5.3.

Step VIII: Repeat step II to VII until the state is mechanically balanced.

3.4 Applications of Level Set Dislocation Dynamics

In this section, we present several applications using LSM for dislocation dynamics. The simulations were performed using the simulation cell which one side l has plus and minus units normalized by the real length of $250b$ (b denotes the magnitude of Burgers vector, here 0.286 nm). The cell box is divided into 64×64×64 grid points. The shear modulus μ is set to be 161GPa, and the Poisson ratio ν is set to be 1/3. For all the calculations, the stresses σ^* are scaled by $\mu b/(2l)$ and time t^* is scaled by $4l/(\mu b^2 m_g)$ where m_g is the mobility constant for dislocation glide and it is set be 1.0 in the present calculations.

During the simulations, the fifth order weighted essentially non-oscillatory (WENO) is used for spatial differentiation and the third order total variation diminishing Runge-Kutta (TVD-RK) is used for temporal differentiation [7]. Reinitialization for keeping the two level set functions, which are both signed distance functions (SDFs), is performed after each time step of solving the evolution equation to reduce the numerical errors. We do not present climb mobility if not specified and the periodic boundary condition is assumed in x, y and z directions.

3.4.1 Prismatic Dislocation Loop Shrinking under the Self-stress by Climb

An edge dislocation normally does not climb at a low temperature when diffusion is difficult and the movements of the dislocation are restricted on the self slip plane. While at a high temperature around 20%-30% of the melting degree, climb starts to take place and becomes severer when the temperature is much higher.

Suppose a dislocation loop with the Burgers vector perpendicular to the plane containing the loop (see Fig. 3.4(a)), in which case each segment of this dislocation loop is pure edge dislocation and this loop is called prismatic dislocation loop (PDL). A PDL can be formed in a material subject to irradiation or quenching by precipitation of vacancies or interstitial atoms [19, 20] and will shrink under the self-stress by climb (the climb mobility m_c is non-zero) at a high temperature (see Fig. 3.4). The leading order term in the shrinking force is [88]

$$f_{ps} = \frac{\mu b^2}{4\pi(1-\nu)} \kappa \log \frac{4}{\varepsilon\kappa} \quad , \tag{3.28}$$

where κ is curvature of the loop and ε is the radius of dislocation core.

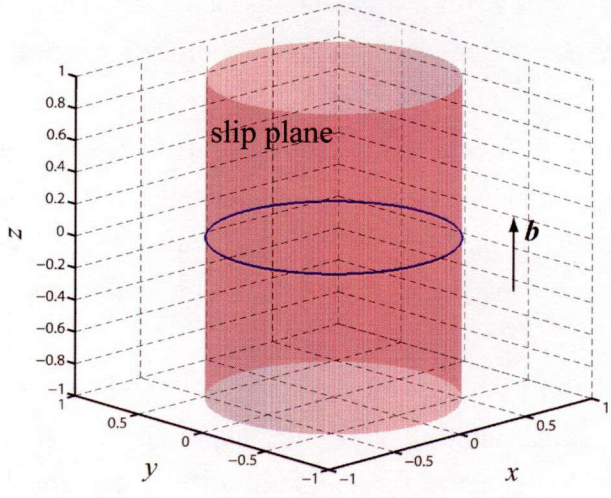

(a) $t^* = 0$

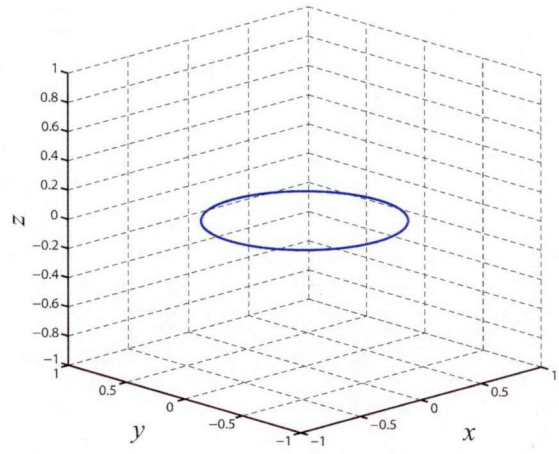

(b) $t^* = 0.03$

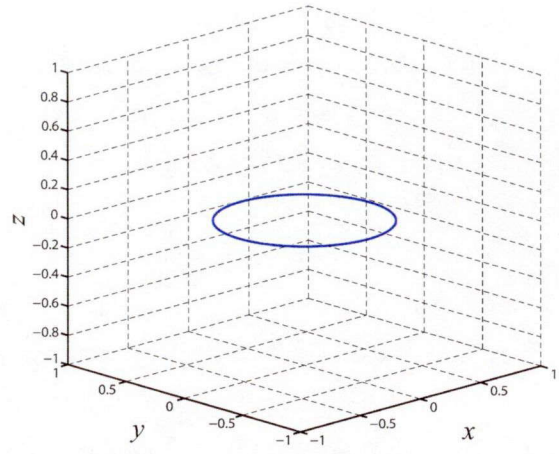

(c) $t^* = 0.06$

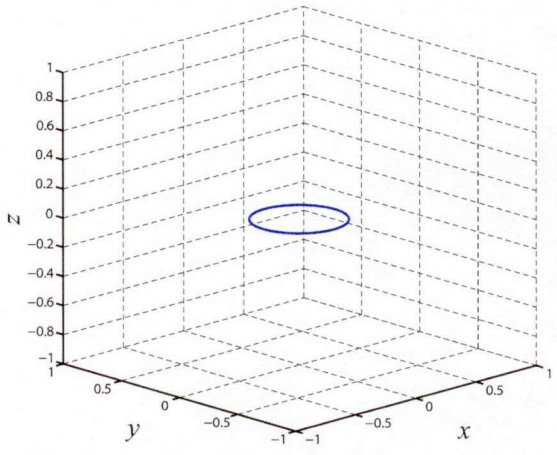

(d) $t^* = 0.09$

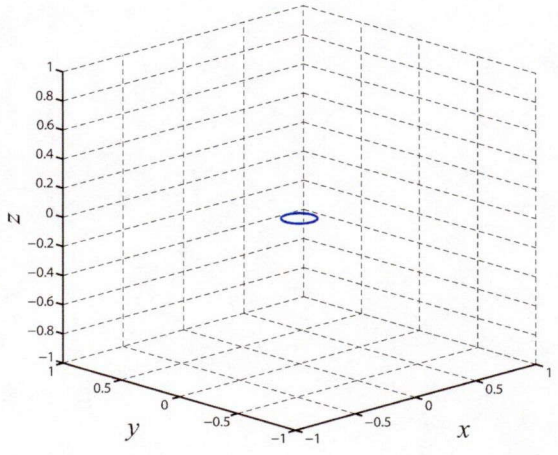

(e) $t^* = 0.12$

Fig. 3.4 A PDL shrinks under the self-stress by climb.

During the evolution, the edge dislocation loop jumps out of its slip plan which is a cylindrical surface (see Fig. 3.4(a)) containing the loop and moves toward the center. Note that the ratio of loop shrinking increases as the radius of the loop decreases since the internal stress of dislocation becomes more intense when segments get closer and finally this PDL vanishes. Recall that the values employed in Eq. (3.28) are $\mu = 161$ GPa, $\nu = 1/3$, $b = 0.286$ nm.

3.4.2 Orowan Loop Expanding under an Applied Stress

For this time, suppose a dislocation loop in the space with a slip plane containing both the dislocation loop itself and the Burgers vector, which is called Orowan loop (see Fig. 3.5(a)). In the absence of applied stress, Orowan loop also tends to shrink with the leading order term of the force [88]

$$f_{os} = \frac{\mu b^2}{4\pi(1-\nu)}[(1+\nu)\cos^2\theta + (1-2\nu)\sin^2\theta]\kappa \log\frac{4}{\varepsilon\kappa} \quad , \tag{3.29}$$

where θ is the angle between the tangent vector of the dislocation and Burgers vector. We apply a scaled stress $\sigma_{xz}^* = 7.5$ to the crystalline material to overcome the shrink of the Orowan loop caused by self-stress and expand this dislocation loop (see Fig. 3.5).

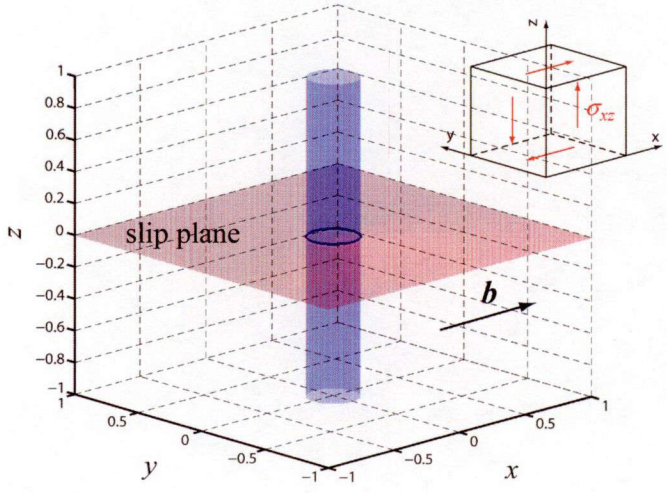

(a) $t^* = 0$

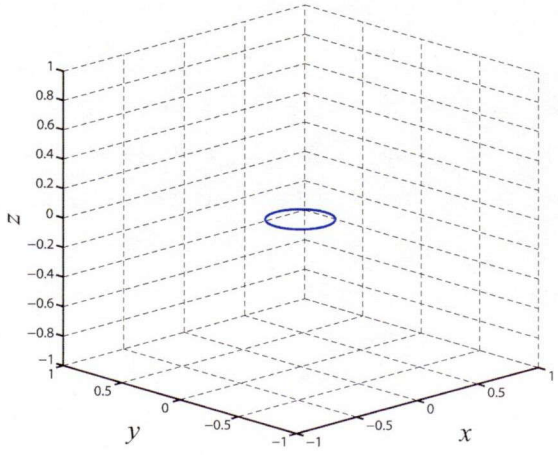

(b) $t^* = 0.03$

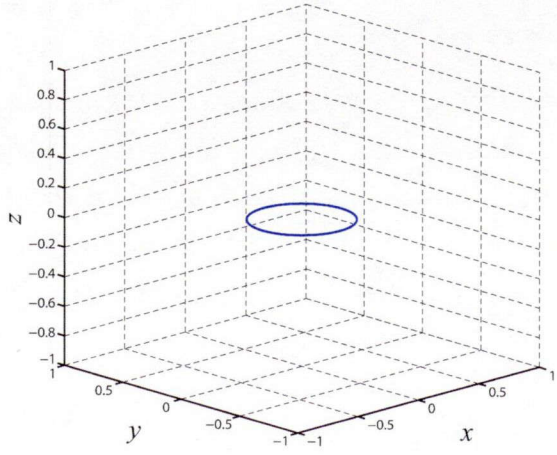

(c) $t^* = 0.06$

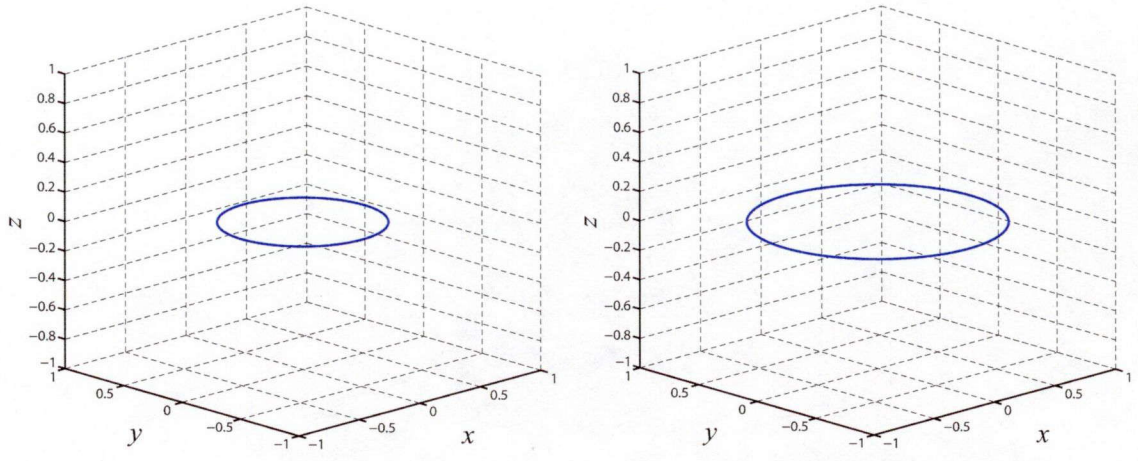

(d) $t^* = 0.09$ (e) $t^* = 0.12$

Fig. 3.5 An Orowan loop expanding under an applied stress σ_{xz}^*.

The simulation result shows the applied stress σ_{xz} has the ability to extend the Orowan loop and the ratio of loop expanding increases as the radius of the loop increases since the internal stress of dislocation becomes less intense when segments get further.

3.4.3 Orowan Loop Evolving under Other Applied Stress

In the previous subsection, we know that the applied stress σ_{xz} has the ability to extend the Orowan loop while we also show an interest on the effects of other applied shear stress to this kind of dislocation loop with or without consideration of climb mobility. An Orowan loop with the Burgers vector in x direction under the scaled shear stress $\sigma_{xz}^* = 2.5$ and $\sigma_{xy}^* = 4.0$ is presented (see Fig. 3.6).

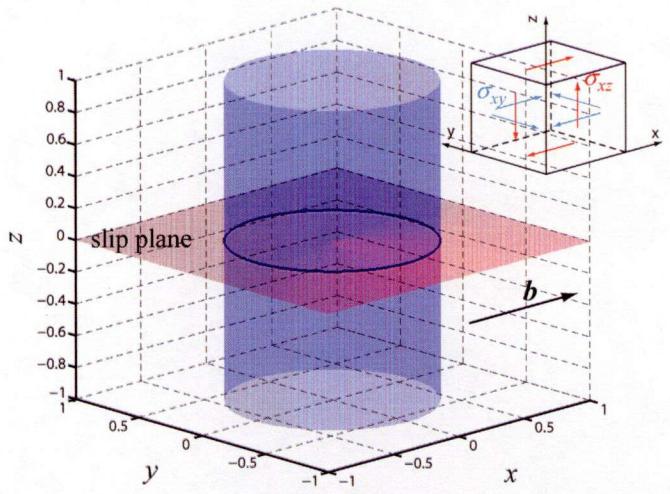

Fig. 3.6 An Orowan loop under the applied stress σ_{xz}^{*} and σ_{xy}^{*} ($t^{*} = 0$).

At a low temperature, the climb of edge dislocations barely happens and we set the mobility ratio m_c / m_g equals to 0. As we can see from Fig. 3.7, the pure screw dislocation segments can move out of the slip plane (x-y plane) to the opposite poles and drag the neighboring mixed segments as a line tension. While the pure edge dislocation segments can only glide on the self slip plane.

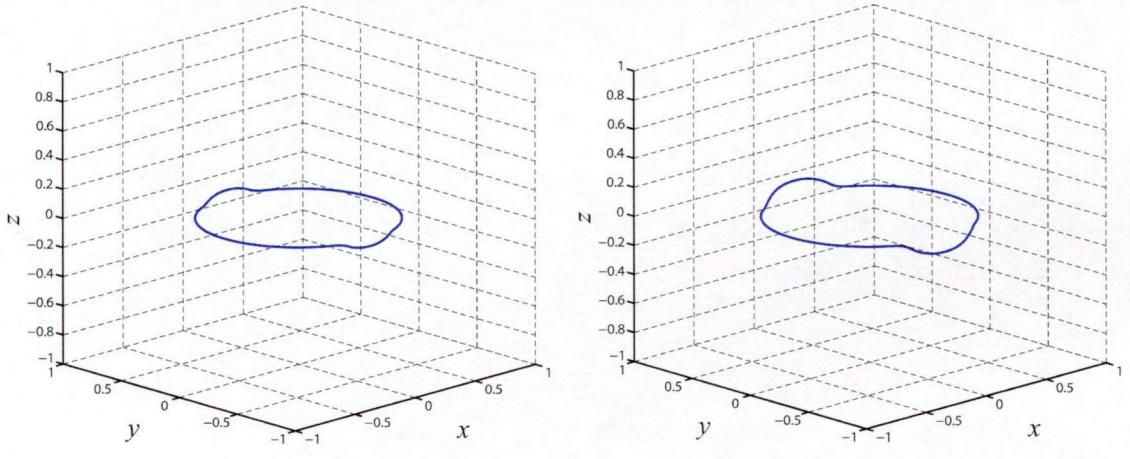

(a) $t^{*} = 0.03$ (b) $t^{*} = 0.06$

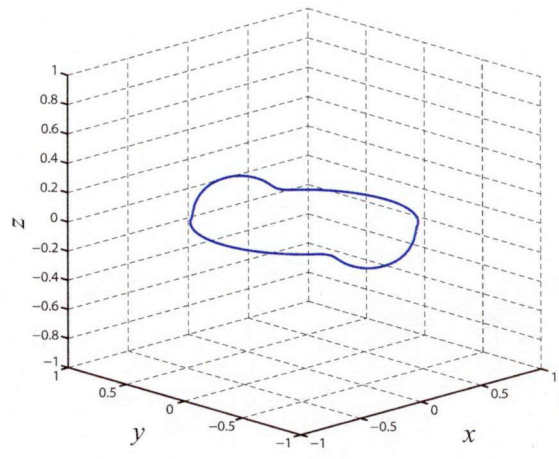

(c) $t^* = 0.09$

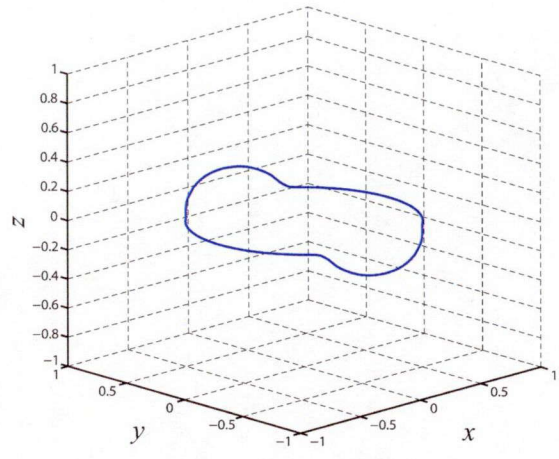

(d) $t^* = 0.12$

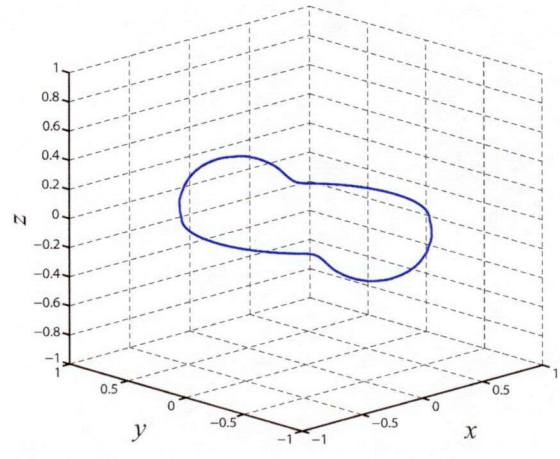

(e) $t^* = 0.15$

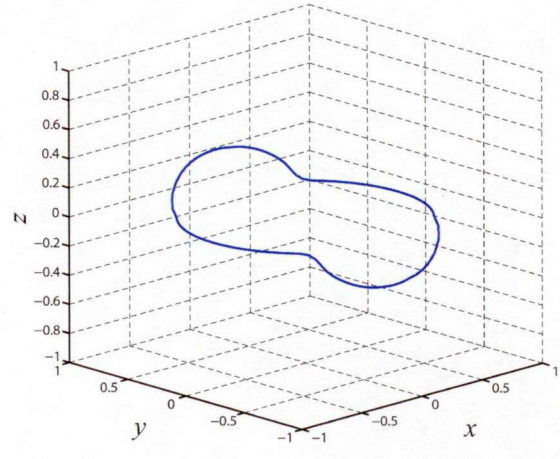

(f) $t^* = 0.18$

Fig. 3.7 An Orowan loop evolving under the applied stress σ^*_{xz} and σ^*_{xy} with $m_c/m_g = 0$.

At a high temperature, the non-screw dislocation segments can freely move out of the slip plane and the mobility ratio m_c/m_g is set to be 1. As we can see from Fig. 3.8, the Orowan loop rotates from its original plane during the expanding.

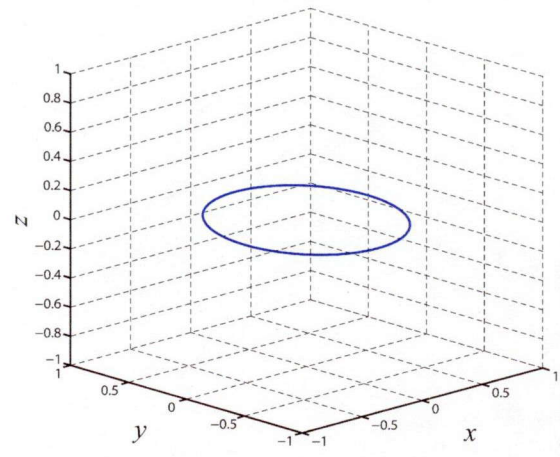

(a) $t^* = 0.03$

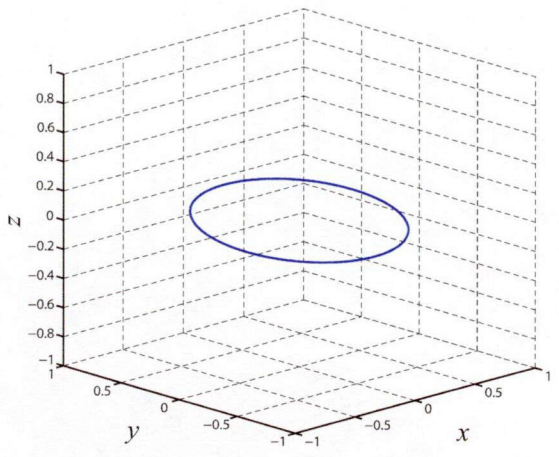

(b) $t^* = 0.06$

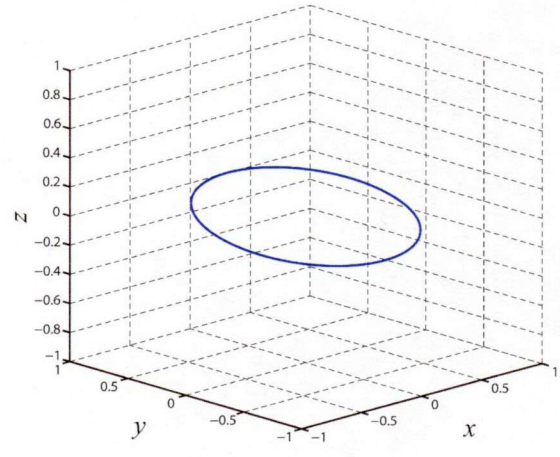

(c) $t^* = 0.09$

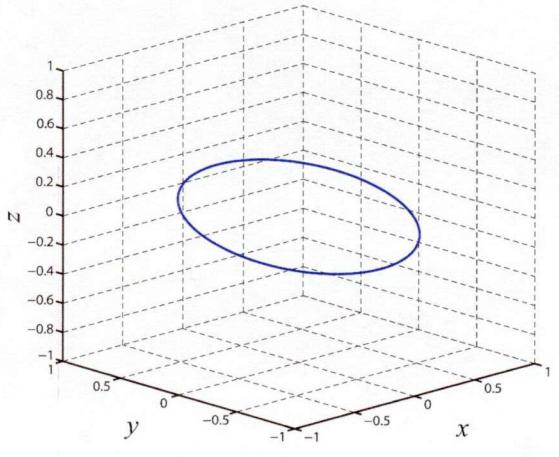

(d) $t^* = 0.12$

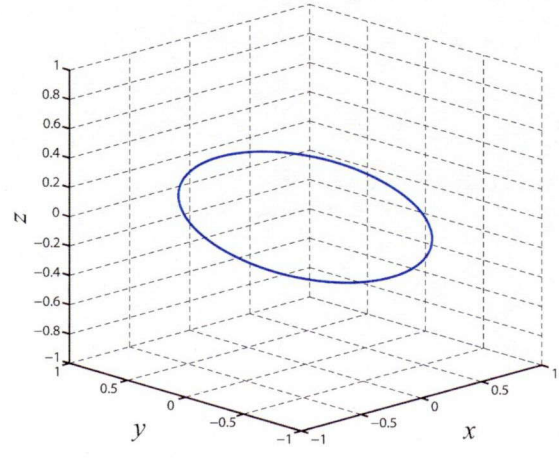

(e) $t^* = 0.15$

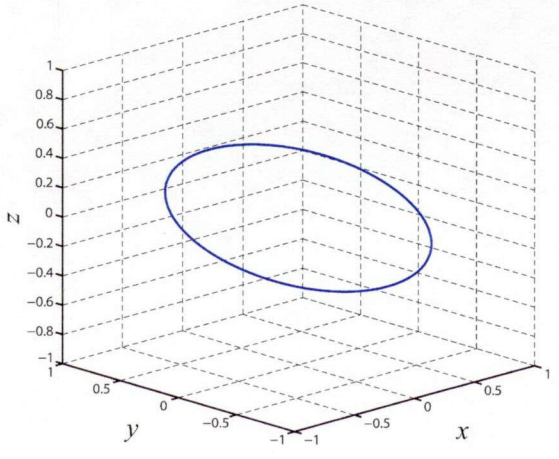

(f) $t^* = 0.18$

Fig. 3.8 An Orowan loop evolving under the applied stress σ_{xz}^{*} and σ_{xy}^{*} with $m_c/m_g = 1$.

Next we consider a medial situation and set the mobility ratio m_c/m_g to be 0.6. The loop also rotates, but since the climb mobility is smaller than glide mobility, the moving of screw dislocation segments is faster than the other parts (see Fig. 3.9).

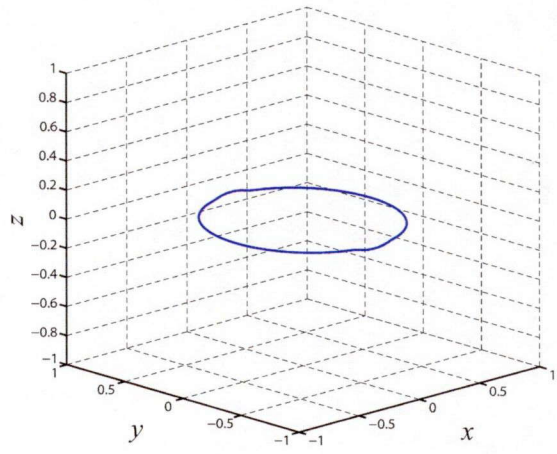

(a) $t^{*} = 0.03$

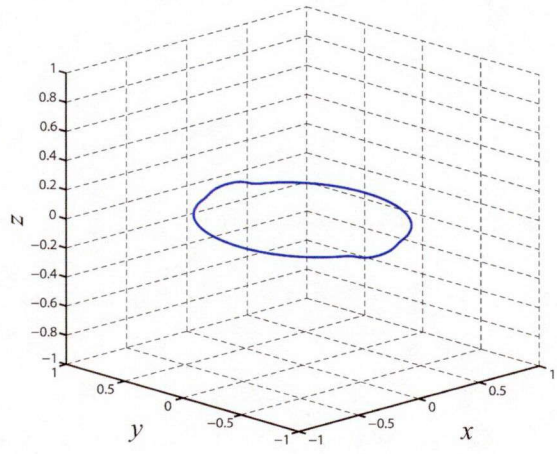

(b) $t^{*} = 0.06$

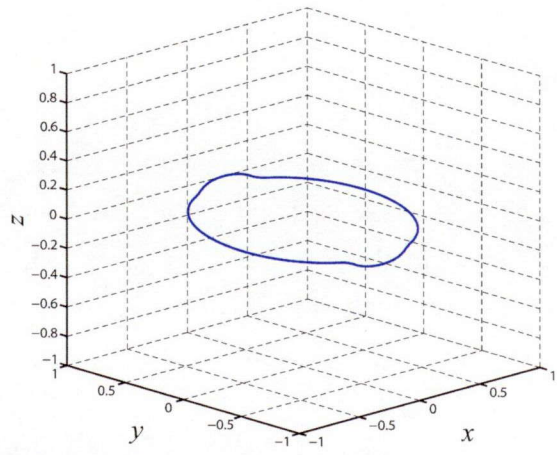

(c) $t^{*} = 0.09$

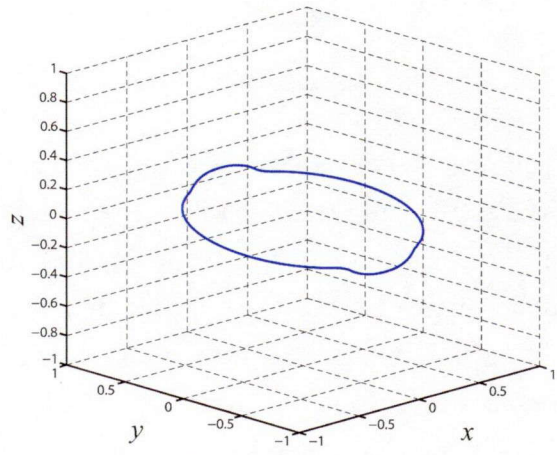

(d) $t^{*} = 0.12$

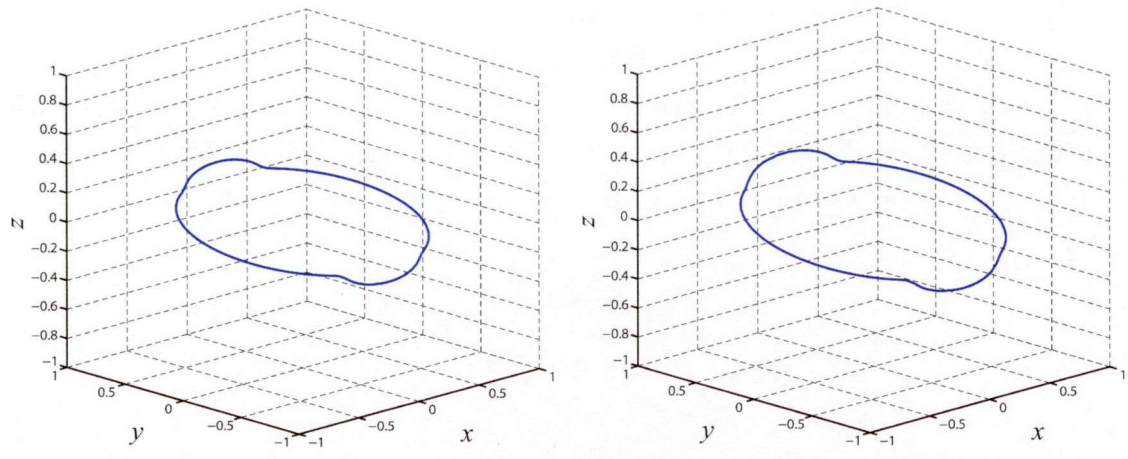

(e) $t^* = 0.15$ (f) $t^* = 0.18$

Fig. 3.9 An Orowan loop evolving under the applied stress σ^*_{xz} and σ^*_{xy} with $m_c/m_g = 0.6$.

The simulation results show that the applied stress σ_{xy} can drag the screw dislocation segments to the opposite poles and intend to rotate the Orowan loop from its initial slip plane at a high temperature.

3.4.4 Interactions of Parallel Dislocation Lines

The dislocation movement takes place from the very beginning of plastic deformation of material. As mentioned in chapter one, the interactions of dislocations are not severe and dislocations mostly glide in parallel slip planes immediately after yield stress. When dislocations get close to each other, the interactions including complex cross-plane interaction and the tangling of dislocations become dramatic, which make the plastic deformation of material hard to proceed.

We first consider two infinite straight edge dislocations I and II with the same orientation in -y direction and the same Burgers vector in x direction (see Fig. 3.10(a)) and want to investigate the movement driven by interaction force of these two dislocations without applied stress. The dislocation II is set apart from I at a distance of l in x direction and d in z direction. When l is smaller than d (we set l slightly smaller than d), the attractive force works, that is the two dislocations will glide on the individual slip planes to get close to each other (see Fig. 3.10).

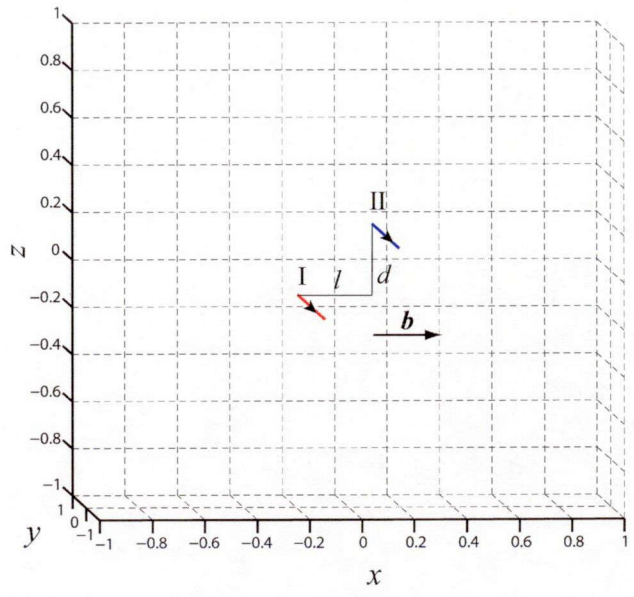

(a) $t^* = 0$

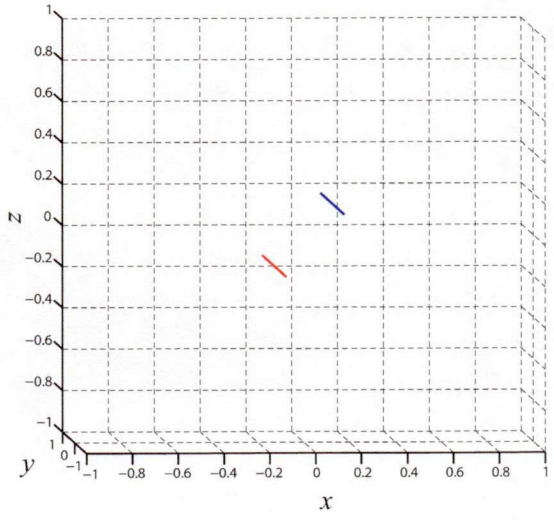

(b) $t^* = 0.03$

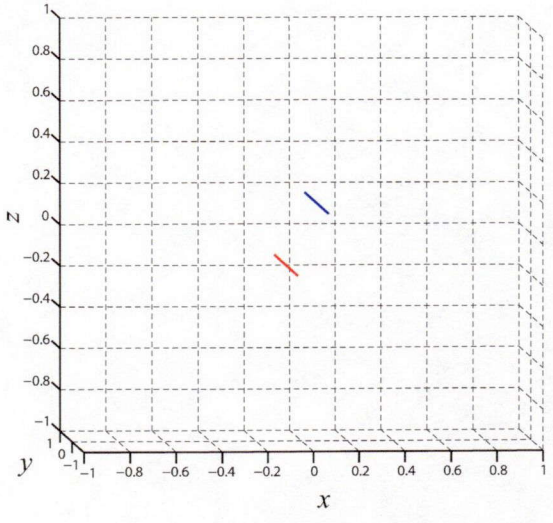

(c) $t^* = 0.06$

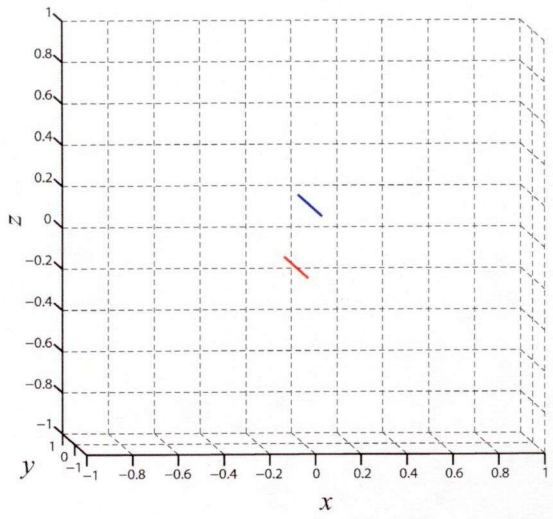

(d) $t^* = 0.09$

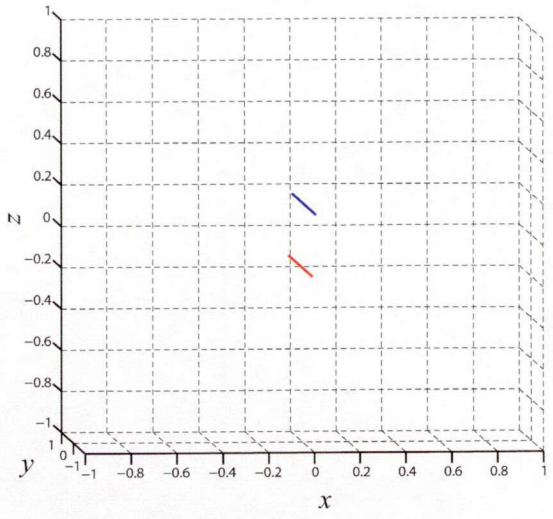

(e) $t^* = 0.12$

Fig. 3.10 Interaction of two parallel edge dislocations with the same orientation and the same Burgers vector ($l < d$).

When we set l slightly larger than d, the repulsive force works, which means that the two dislocations will glide on the individual slip planes to leave apart from each other (see Fig. 3.11).

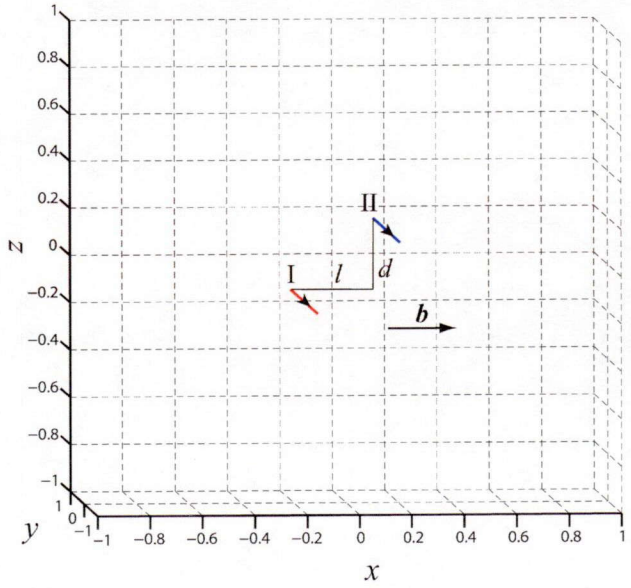

(a) $t^* = 0$

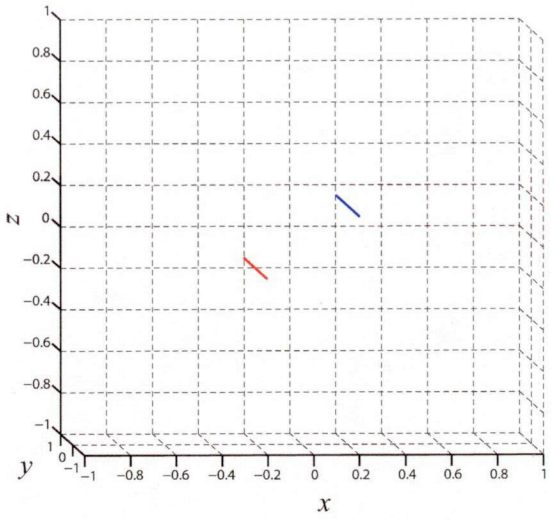

(b) $t^* = 0.03$

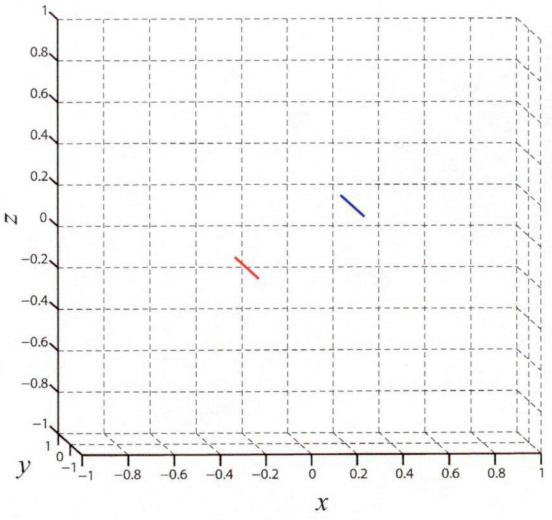

(c) $t^* = 0.06$

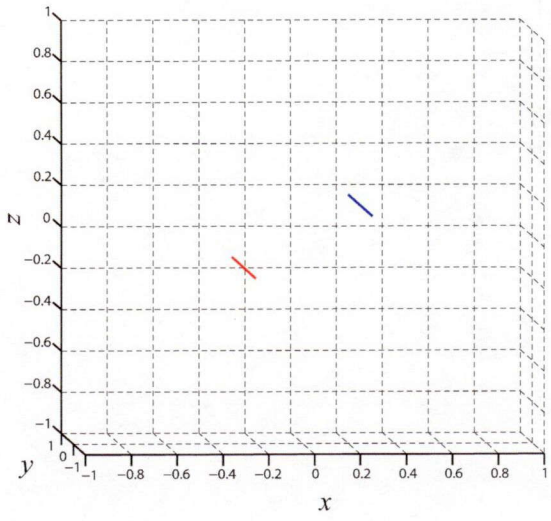

(d) $t^* = 0.09$

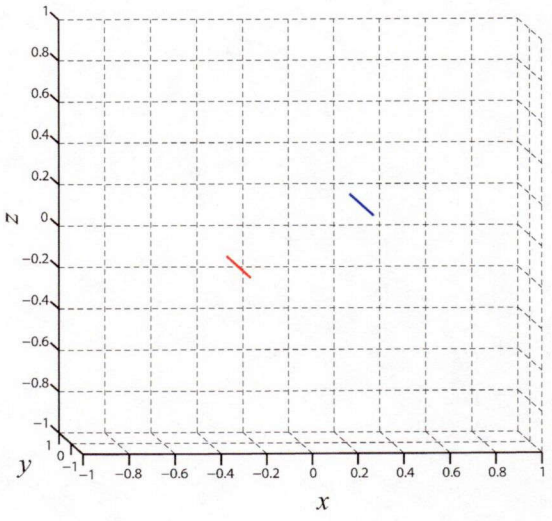

(e) $t^* = 0.12$

Fig. 3.11 Interaction of two parallel edge dislocations with the same orientation and the same Burgers vector ($l > d$).

Next we consider two screw dislocations with opposite orientations $\boldsymbol{t}_{\mathrm{I}}$ = (0, -1, 0) and $\boldsymbol{t}_{\mathrm{II}}$ = (0, 1, 0), respectively, and the same Burgers vector in -y direction (see Fig. 3.12(a)).

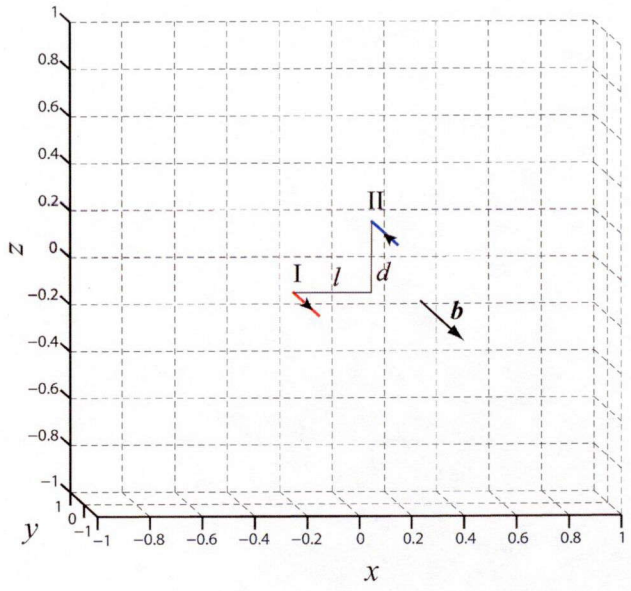

(a) $t^* = 0$

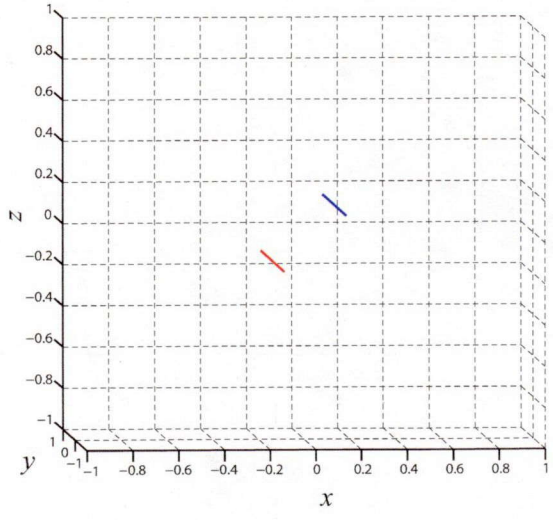

(b) $t^* = 0.03$

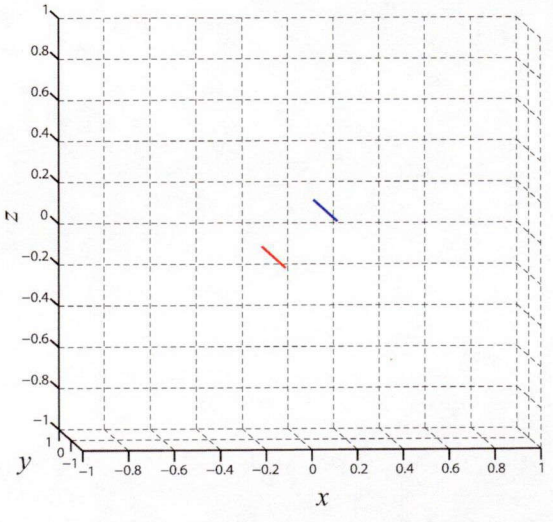

(c) $t^* = 0.06$

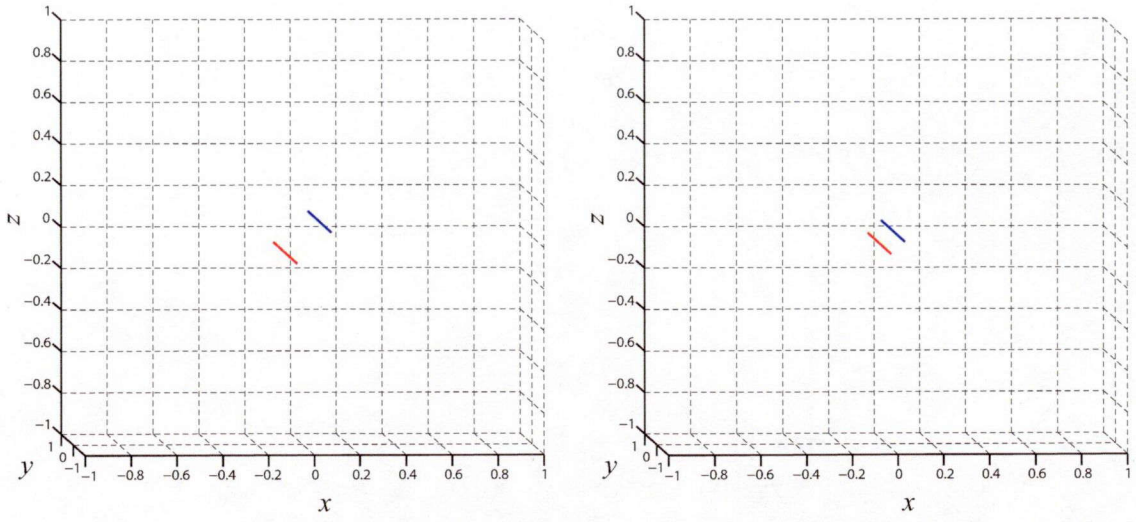

(d) $t^* = 0.09$ (e) $t^* = 0.12$

Fig. 3.12 Interaction of two parallel screw dislocations with opposite orientations and the same Burgers vector.

Two screw dislocations with opposite directions attract each other. Since any plane can be a slip plane for a screw dislocation, these two dislocations move directly toward each other and annihilates when they meet. Predictably, two screw dislocations with the same orientation and Burgers vector move apart from each other.

3.4.5 Interactions of Perpendicular Dislocation Lines

We discussed dislocations with parallel slip planes from the previous subsection. Now we consider two perpendicular dislocations with the tangent vectors $\boldsymbol{t}_{\mathrm{I}} = (0, -1, 0)$, $\boldsymbol{t}_{\mathrm{II}} = (1, 0, 0)$, and Burgers vectors $\boldsymbol{b}_{\mathrm{I}} = (0, -b_{\mathrm{I}}, 0)$, $\boldsymbol{b}_{\mathrm{II}} = (b_{\mathrm{II}}, 0, 0)$, respectively (see Fig. 3.13(a)). Since there is no specific slip plane for a screw dislocation, these two screw dislocations move directly by Peach-Koehler force. Two dislocation lines get close especially the middle segments that are closest to each other under the attractive force caused by each other's self-stress. The interaction becomes more severe when dislocation segments get closer (see Fig. 3.13).

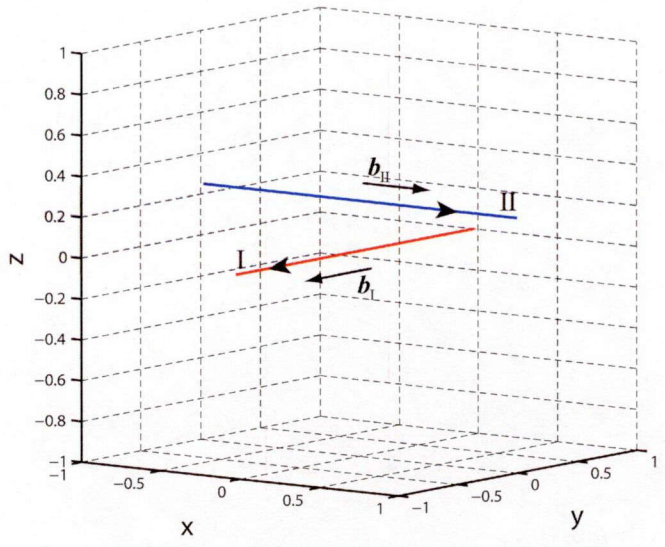

(a) $t^* = 0$

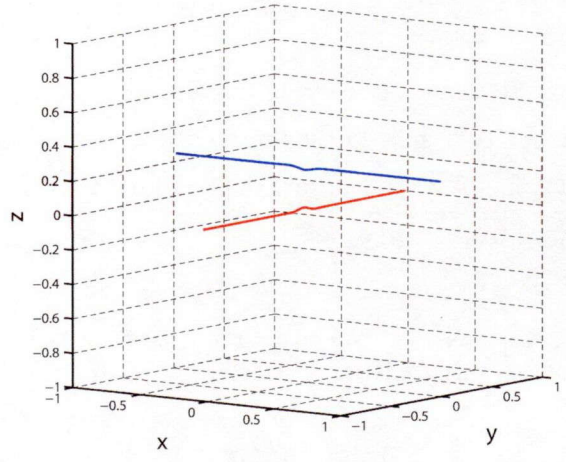

(b) $t^* = 0.03$

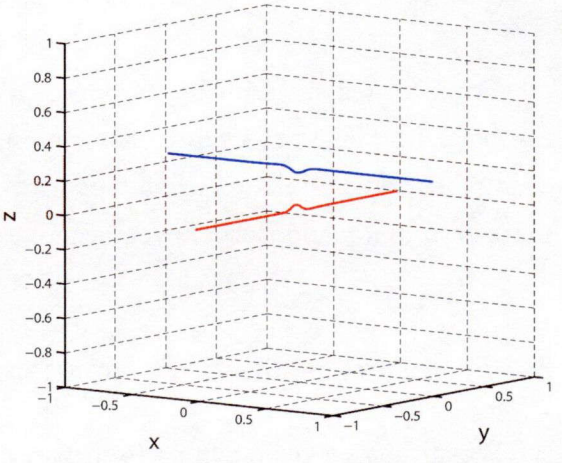

(c) $t^* = 0.06$

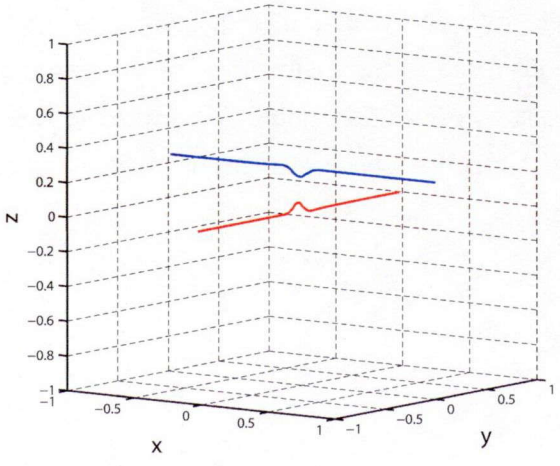

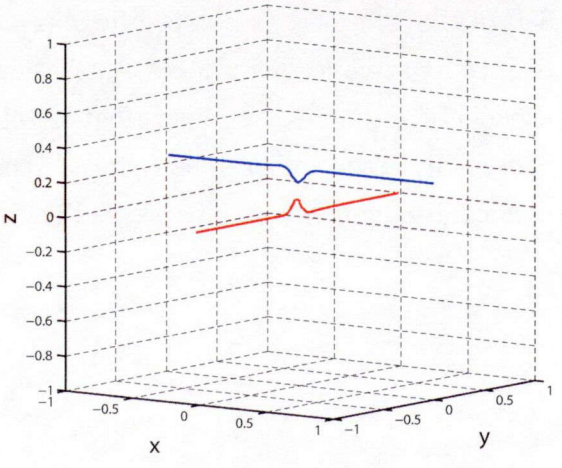

(d) $t^* = 0.09$ (e) $t^* = 0.12$

Fig. 3.13 Interaction of two perpendicular screw dislocations: case one.

Dislocations are line defects not only with Burgers vectors but also with orientations. We reset the direction of dislocation II from $\boldsymbol{t}_{II} = (1, 0, 0)$ to $\boldsymbol{t}_{II} = (-1, 0, 0)$ while the other conditions are exactly the same (see Fig. 3.14(a)). As we can see from Fig. 3.14, repulsive force takes place for this time and dislocations move apart from each other especially around their middle parts. The effect becomes weaker as the middle parts move further from each other and the movement becomes slower.

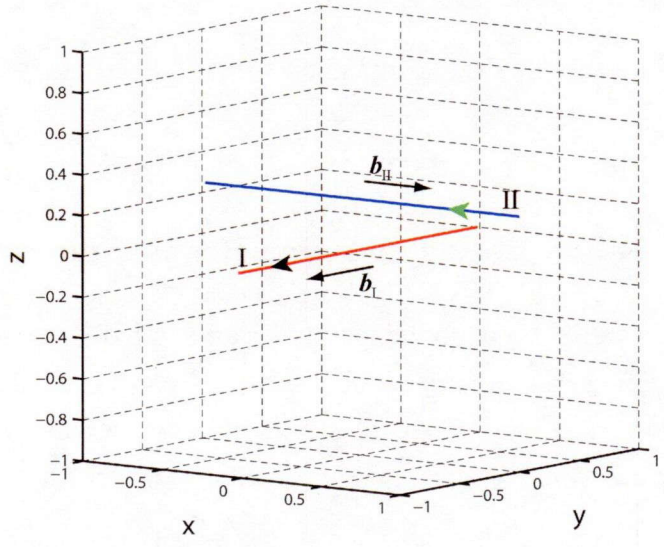

(a) $t^* = 0$

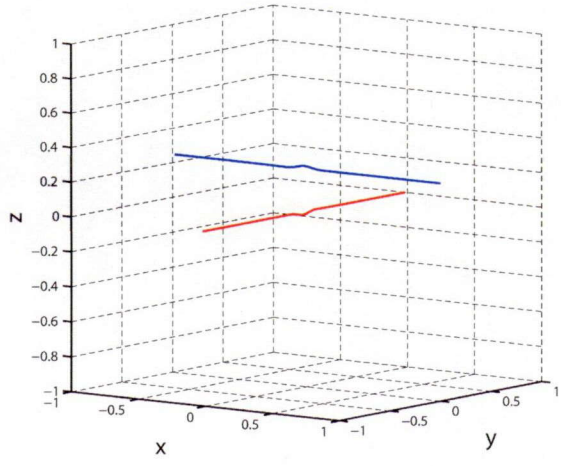

(b) $t^* = 0.03$

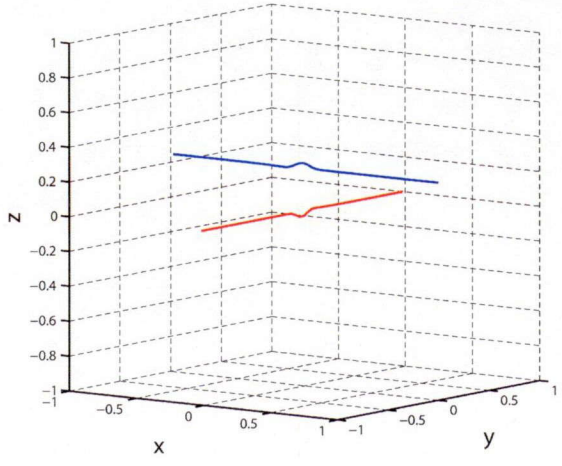

(c) $t^* = 0.06$

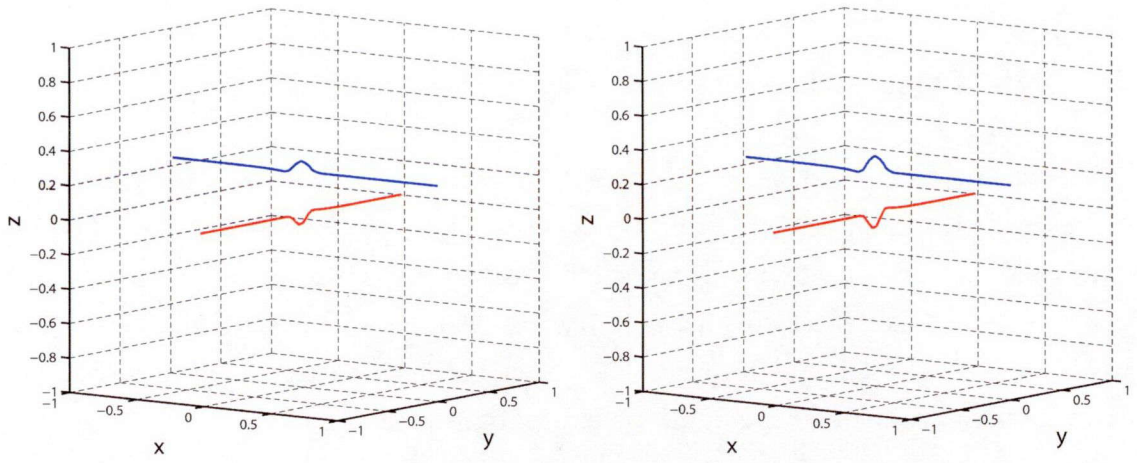

(d) $t^* = 0.12$ (e) $t^* = 0.18$

Fig. 3.14 Interaction of two perpendicular screw dislocations: case two.

3.4.6 Dislocation Bypassing an Impenetrable Spherical Particle

An edge dislocation can glide continuously under an applied shear stress until it meets other defects. Assuming that an impenetrable spherical particle exists on the way where the dislocation glides (see Fig. 15(a)). This hard particle with the radius of R exerts a strong short-range repulsive force acting on dislocations as [75, 78]

$$\begin{cases} f_0 & (r \le R) \\ f_0(R + dx - r)^2 / \mathrm{d}x^2 & (R < r \le R + \mathrm{d}x) \\ 0 & (r > R + \mathrm{d}x) \end{cases}, \tag{3.30}$$

where r is the distance from a point to the center of the particle and the width dx is the grid constant. We set the f_0 to be large enough to make sure that this hard particle cannot be penetrated by dislocations. Fig. 3.15 successfully shows an edge dislocation bypassing a hard spherical particle and leaves an Orowan loop.

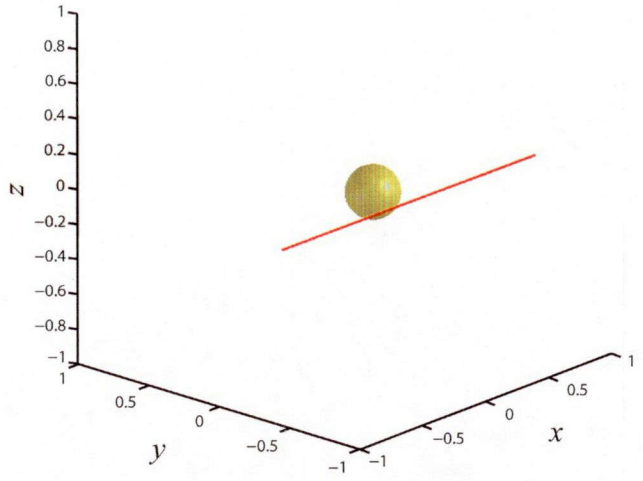

(a) $t^* = 0$

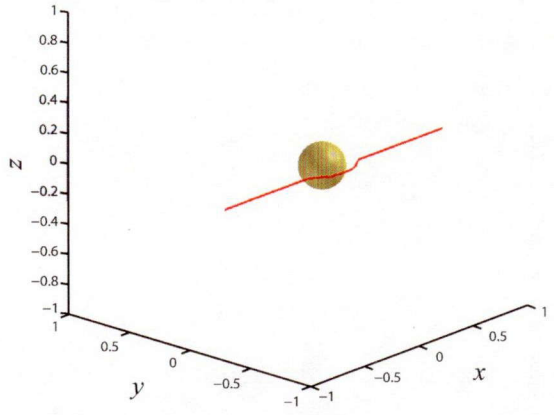

(b) $t^* = 0.07$

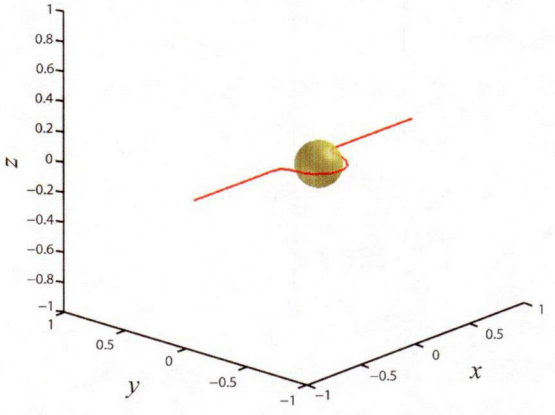

(c) $t^* = 0.17$

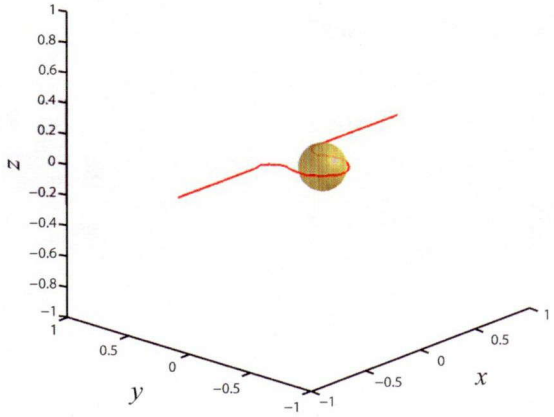

(d) $t^* = 0.24$

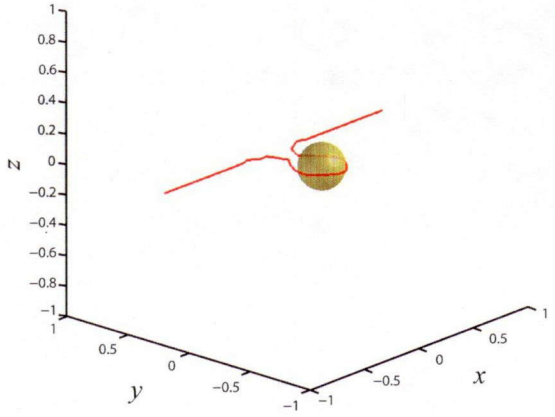

(e) $t^* = 0.29$

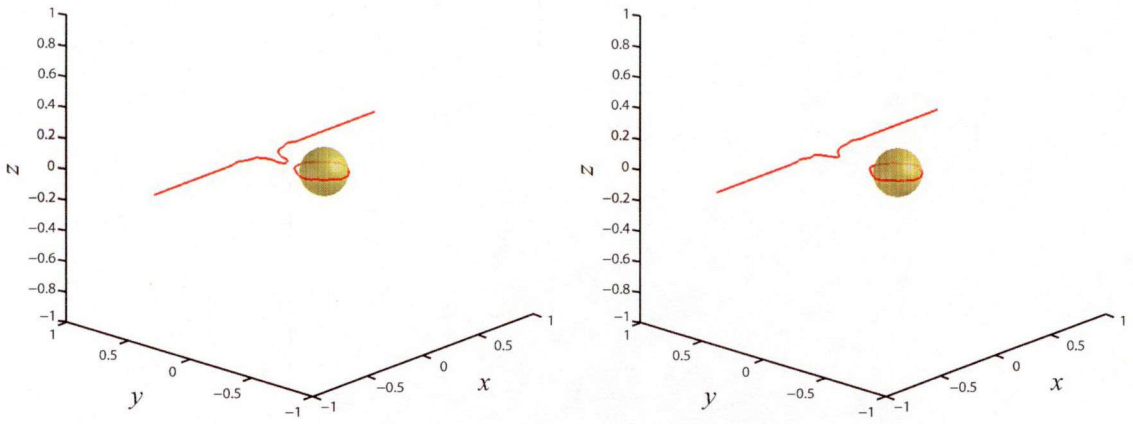

(f) $t^* = 0.33$ (g) $t^* = 0.37$

Fig. 3.15 An edge dislocation bypassing an impenetrable spherical particle.

The bypassing mechanism implies that the motions of dislocations are hindered if particles exit. As a consequence, the plastic deformations of the material are obstructed, which means that the existing of particles strengthens the material.

3.5 Conclusion

We have demonstrated a series of dislocation dynamics simulations based on level set method for codimension-two objects which are curves in three dimensions endued with physical meaning. The models of dislocation evolutions under self-stress and applied stress, dislocation/dislocation interactions and dislocation/particle interactions can all be demonstrated and the results quite accommodate to the analytical expectations. The internal stress field can be solved efficiently using FFT, assuming periodic boundary. Topological changes of dislocations, especially when merging and breaking occur, are handled naturally using level set dislocation dynamics. Besides, the simulations are performed in a relative large space and a long time interval.

Chapter 4

Evaluations for the Internal Stress Field of a Double Cross-slipped Dislocation Loop

4.1 Abstract

The onset of the second stage in the work hardening for an fcc single crystal, called *dynamic recovery*, where the curvature $\partial^2\sigma/\partial^2\varepsilon$ of a stress-strain curve becomes negative, is associated with the onset of cross-slip. However, there are a number of possible mechanisms for cross slip working in the final stage of work hardening [89-92]. Since the determination of the activation energies for these processes is very complicated, the detailed analysis of stage III remains uncertain. One mechanism for cross slip of a perfect dislocation is explained [93, 94]. Since the complexity and uncertain of the mechanism, we use level set dislocation dynamics (LS-DD) to model the phenomenon of cross slip and double cross slip and investigate the changes of internal stress and the effects of the cross-slipped dislocation to other dislocations.

This chapter is organized as follows. In Section 4.2, the mechanism for cross slip and double cross slip of a perfect dislocation is explained. In Section 4.3, the technique of moving curves on surfaces for level set evolutions is introduced. In Section 4.4, the double cross-slip of an expanding Orowan loop is modeled using LS-DD with the investigation of internal stress of the cross-slipped loop and the effects to other dislocations from the distorted dislocation loop.

4.2 Mechanism for Cross-slip and Double Cross-slip of a Perfect Dislocation

One mechanism for cross slip is suggested as shown in Fig. 4.1 [20]. In general, a screw dislocation tends to move in certain crystallographic planes, but can switch from one slip plane to another with the same Burgers vector ***b***. As we can see from Fig. 4.1(a), a perfect dislocation in fcc metal expands under the action of an applied shear stress on (1 1 1) plane with the Burgers vector ***b*** = [-1 0 1]. The loop expands until the local stress field makes dislocation motion changes and the loop prefers its gliding on (1 -1 1) to on (1 1 1). Since only the pure screw segment is free to move in both (1 1 1) and (1 -1 1) planes, this segment crosses slip at the edge of two planes (S in Fig. 4.1(b)) and glides on (1 -1 1) plane (see Fig. 4.1(c)) until it meets the edge CD where the loop prefers the initial slip plane of (1 1 1). Similarly, as shown in Fig 4.1(d), the screw dislocation crosses slip again from (1 -1 1) to (1 1 1) plane. This process is known as the double cross slip.

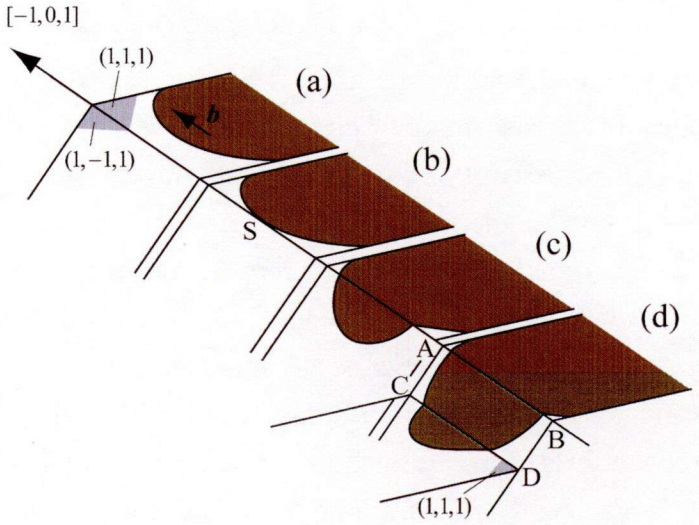

Fig. 4.1 A scheme of the mechanism for cross-slip and double cross-slip of a screw dislocation in a fcc metal.

4.3 Moving Curves on Surfaces

Given a surface M in three dimensions and a curve on that surface, suppose that the curve is constrained on surface M under a specific type of motion [95]. To realize this kind of restriction, the velocity of the curve is projected on the surface and the evolution equation turns to be:

$$\phi_t + P_{\nabla\psi}\boldsymbol{v}\cdot\phi_{\boldsymbol{x}} = 0\,, \tag{4.1}$$

where $P_{\nabla\psi}$ is the orthogonal projection operation which is defined by

$$P_{\nabla\psi} = \boldsymbol{I} - \frac{\nabla\psi\times\nabla\psi}{|\nabla\psi|^2}\quad . \tag{4.2}$$

Thus, the $P_{\nabla\psi}$ projects velocity $\boldsymbol{v}$ onto the level set surfaces of ψ, passing through the points in three dimensions.

An example a curve moving on a constrained surface is shown in Fig. 4.2. A loop expands in three dimensions, when given a specific constrain plane (see green plane in Fig. 4.2) with the usage of orthogonal projection operation from Eq. (4.2), the expanding velocity of the loop is projected onto the green plane and also the loop motion is constrained in that plane.

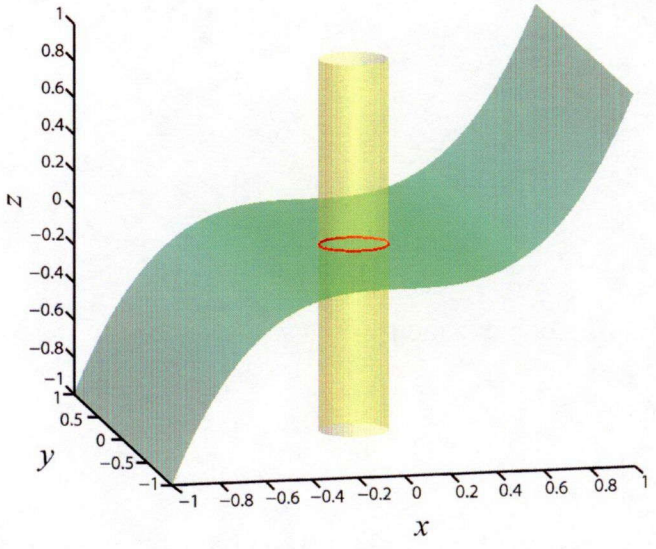

(a) $t = 0$

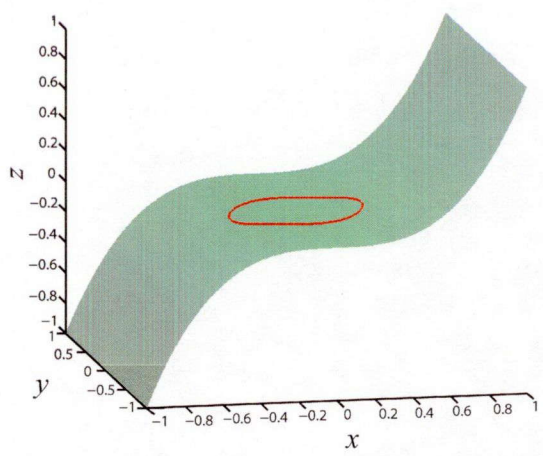

(b) $t = 0.2$

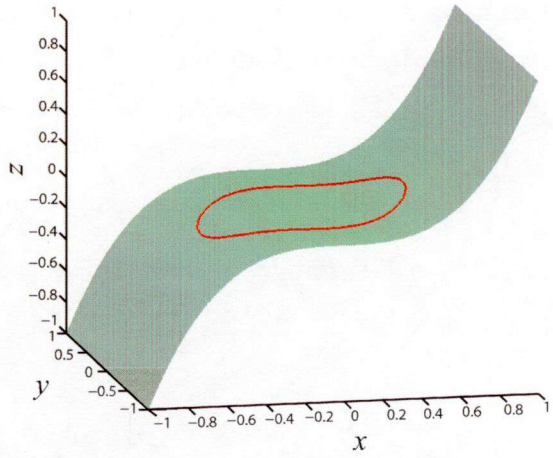

(c) $t = 0.4$

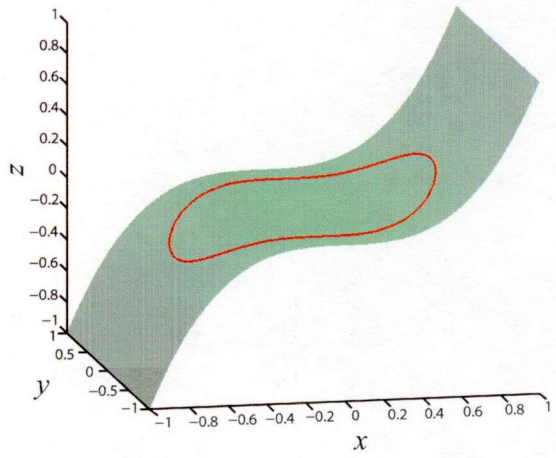

(d) $t = 0.6$

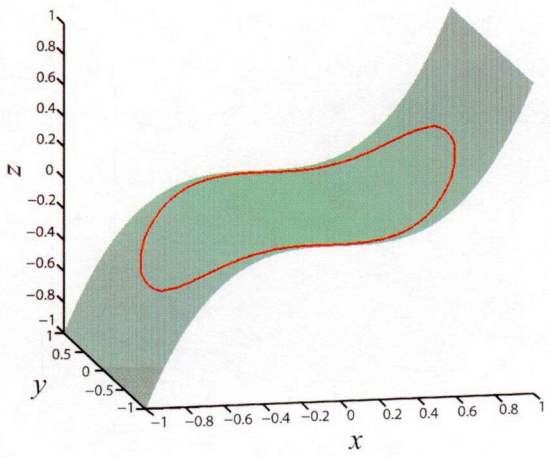

(e) $t = 0.8$

Fig. 4.2 Loop expanding on a specific constrained plane.

4.4 Double Cross-slip and Internal Stress Field

The simulations were performed using the simulation cell which one side has plus or minus unit normalized by the real length of 250b (b denotes burgers magnitude of 0.286 nm). The cell box is divided into 64×64×64 grid points. The shear modulus μ is set to be 161GPa and Poisson ratio ν is set to be 1/3. For all the calculations, the stresses σ^*

are scaled by $\mu b/(2l)$ and time t^* is scaled by $4l/(\mu b^2 m_g)$ where m_g is the mobility constant for dislocation glide and it is set be 1.0 in the present calculations.

During the simulations, the fifth order weighted essentially non-oscillatory (WENO) is used for spatial differentiation and the third order total variation diminishing Runge-Kutta (TVD-RK) is used for temporal differentiation [96-99].

4.4.1 Internal Stress of a Double Cross-slipped Dislocation

It's complicated for continuum dislocation models to demonstrate double cross-slip without using artificial rules. In this simulation, we create a double cross-slip plane on which the velocity vector of the loop evolution is projected to make sure that the dislocation can only glide on this specific plane (the curved green plane of Figure 4.3). The Orowan dislocation loop placed on the slip plane with the Burgers vector parallel to y coordinate, $\boldsymbol{b}$ = (0, b, 0), is subjected to the applied stress which varies during the dislocation evolution (see Fig. 4.3).

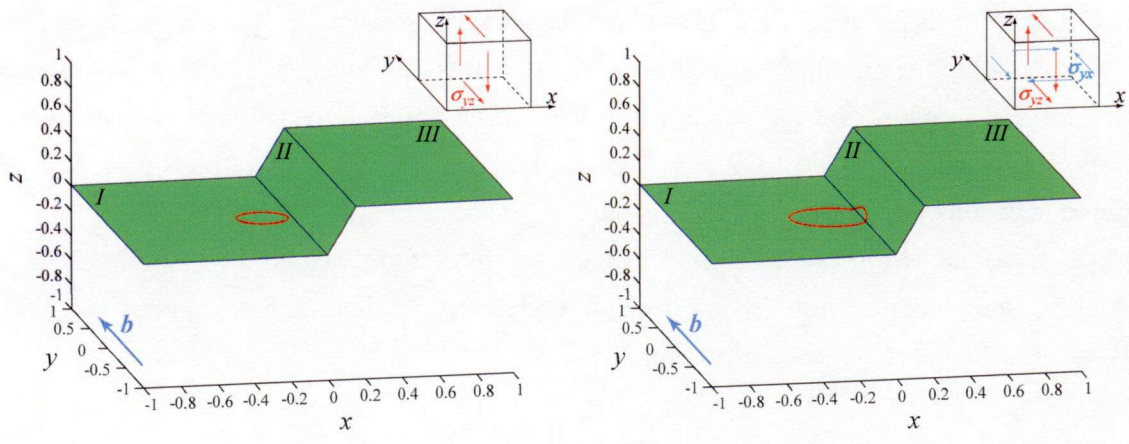

(a) In Plane *I* (b) Plane *I* to *II*

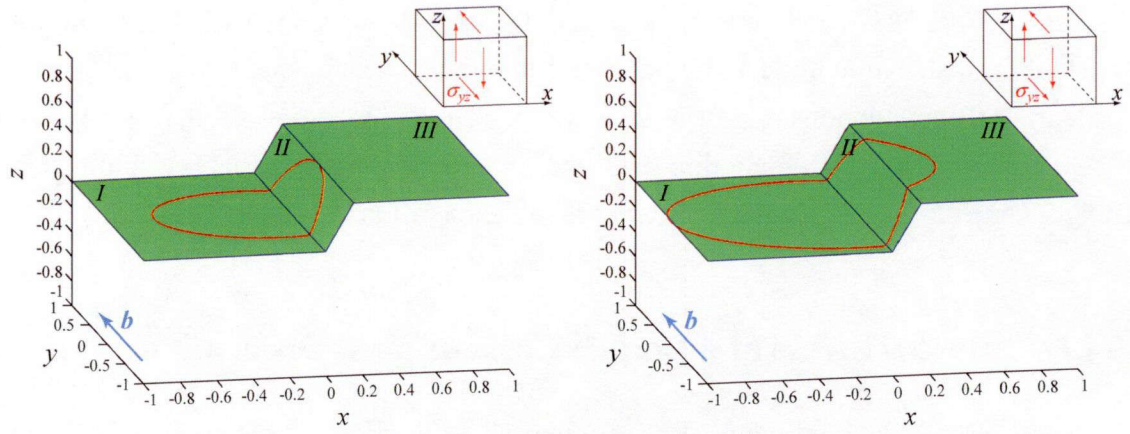

(c) Plane *I* to *II* (d) Plane *I* to *II* and then *III*

Fig. 4.3 Double cross-slip of a dislocation loop under the applied stress.

The Orowan loop first only expands on the self slip plane (plane *I*) under the applied stress σ_{yz} (see the top-right cubic of Fig. 4.3(a)). When this loop just meets the edge of plane *II*, we add another component σ_{yx} as the applied stress (see the top-right cubic of Fig. 4.3(b)). When this loop meets the edge of plane *III* again, the applied stress resumes to be like that for Fig. 4.3(a). The dislocation crosses slip again from plane *II* to plane *III*, which is parallel to the plane *I*, and expands on plane *III*. The dislocation does the cross slip twice, and we successfully realize the double cross slip. Now we discuss how to set the stress ratio of $\gamma = \sigma_{yx} / \sigma_{yz}$ so that the Peach-Koehler force projected on plane *II* becomes larger than that on plane *I*.

Before discussing the numerical results, we think about the simple example first: a straight screw dislocation in y direction under the applied stress σ_{yz} and σ_{yx}. The Peach-Koehler force in each direction is;

$$\begin{cases} f_x = \sigma_{yz} b = f_I \\ f_z = \sigma_{yx} b \end{cases}, \tag{4.3}$$

where f_x is the force in x direction, it is also the force on plane *I*; f_z is the force in z direction. The force on plane *II* is $f_{II} = f_x \cos\theta + f_z \sin\theta$. When $\beta = f_{II} / f_I > 1$ as $\gamma = \sigma_{yx} / \sigma_{yz}$,

$$\beta = \frac{f_{II}}{f_I} = \frac{\sigma_{yz} b \cos\theta + \sigma_{yx} b \sin\theta}{\sigma_{yz} b} = \cos\theta + \gamma \sin\theta > 1 \quad , \tag{4.4}$$

$$\therefore \gamma > \frac{1 - \cos\theta}{\sin\theta} \quad , \tag{4.5}$$

that is, when $\gamma > (1-\cos\theta)/\sin\theta$, the force on plane *II* overcomes the force on plane *I*, in which case it's more reasonable for the dislocation to glide on plane *II* rather than on plane *I*. For the model employed here in Fig. 4.3, θ is 68.2deg, and thus β is 1 when γ is 0.68 (drawn as the linear solution in Fig. 4.4).

For the three dimensional dislocation loop, we need to think about not only the applied stress field but also the internal stress field, since the internal stress also affects the dislocation evolution (drive the loop to shrink etc.). Figure 4.4 shows the relationships between γ ($=\sigma^*_{yx}/\sigma^*_{yz}$) and β ($=f_{II}/f_I$) when the applied stress σ^*_{yz} are 10, 20, 50, 100, respectively.

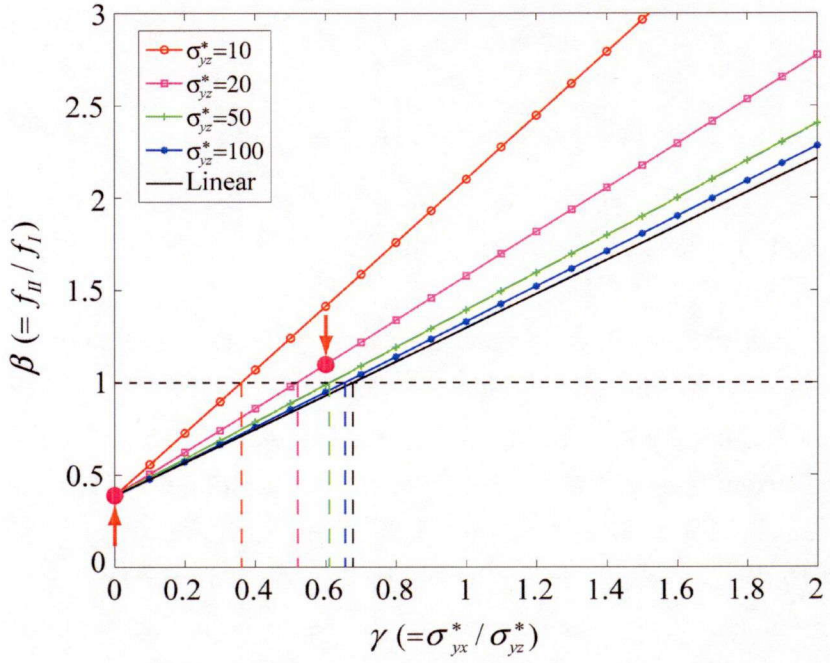

Fig. 4.4 Correlation between γ and β using LSM calculations.

When the applied stress σ^*_{yz} is relatively small, say 10 (see the red line of Fig. 4.4), the effect of internal stress is large and γ is small (0.36 compare to the linear solution 0.68). When the applied stress σ^*_{yz} is 100 in which order the internal stress is negligible, the $\gamma - \beta$ relationship is very close to the linear solution. This fact suggests that the driving force to cross slip is much affected by the topological three dimensional effect of the loop, and the less external stress σ^*_{yz} should be enforced to the field when applied stress relatively small since the internal stress arising from the loop is superimposed.

We take two cases: when $\gamma = 0$ and $\gamma = 0.6$ both of which are under the applied stress $\sigma^*_{yz} = 20$ (indicated by arrowheads in Fig. 4.4), and then observe the topological

change of each case and discuss the internal stress field. When $\gamma = 0$, the β is far below 1, the loop will only glide on the plane I (see Fig. 4.5(a)).

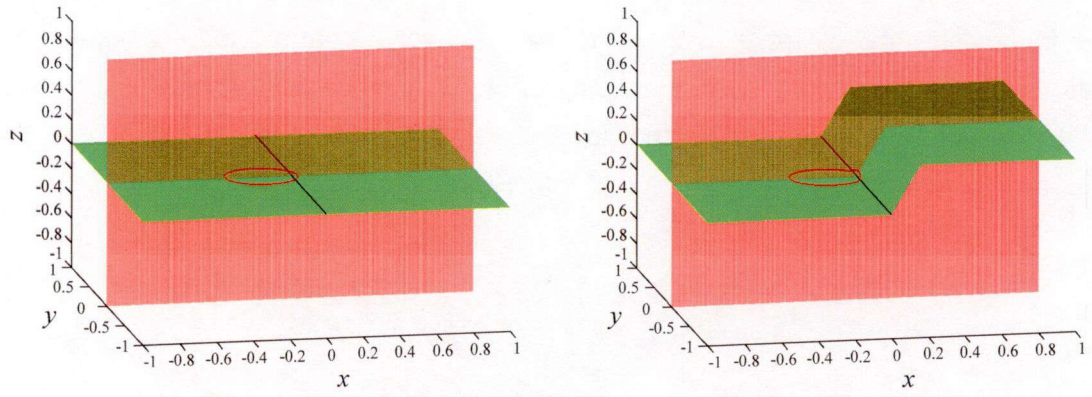

(a) γ=0 (b) γ=0.6

Fig. 4.5 Cross sections for displaying the internal stress distributions at γ=0 and γ=0.6 both of which are under the applied stress σ^*_{yz}=20 at $t^* = 0.005$.

Taking a slice of the dislocation configuration in the light red colored-plane in Fig. 4.5(a), the internal stress distributions are demonstrated in Fig. 4.6: Fig. 4.6(a) is dimensionless σ^*_{yx} component for Fig. 4.5(a) and Fig. 4.6(b) is σ^*_{yz}. Figs. 4.6(c), (d) and (e) are σ^*_{yz} distributions for the more expanded loop on plane I. The calculation steps were increased about four times for Fig. 4.6(c), seven times for (d), and twelve times for (e) of Fig. 4(b). Since the cell box is constrained to the periodic boundary condition, it should be reminded that the stress extremely close to both sides is influenced by the neighbor virtual cells. σ^*_{yx} is distributed mainly toward z direction, and thus the strong interference of stress is not observed inside the loop. Meanwhile, σ^*_{yz} is negative between the two dislocation cores and elliptically distributed. And it is positive on the left side and right side of the loop and symmetrically distributed according to the plane of $z = 0$. Therefore, σ^*_{yz} is the source for the dislocation to shrink itself and it could become the barrier for the dislocation to expand due to the external applied stress. When the loop is more expanded as Fig. 4.6(c) to (e), the stress inside the loop decays but still has a long-ranged interaction.

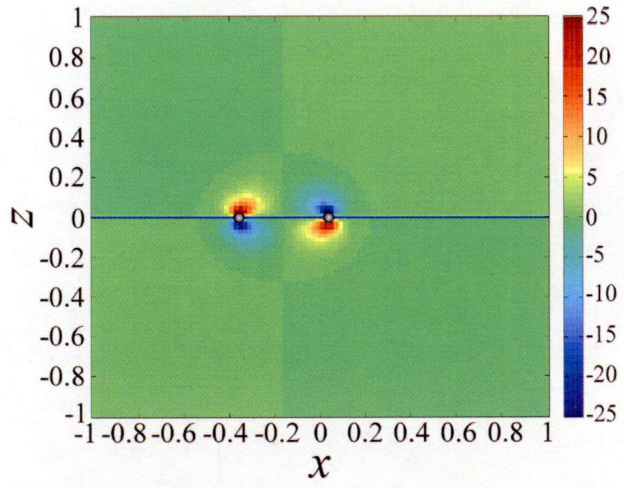

(a) σ^*_{yx} for Fig. 4.5(a)

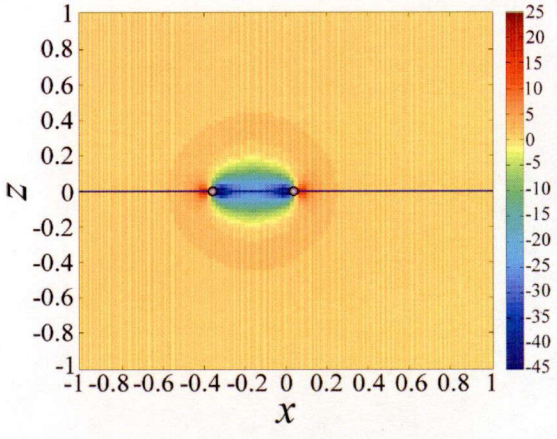

(b) σ^*_{yz} for Fig. 4.5(a)

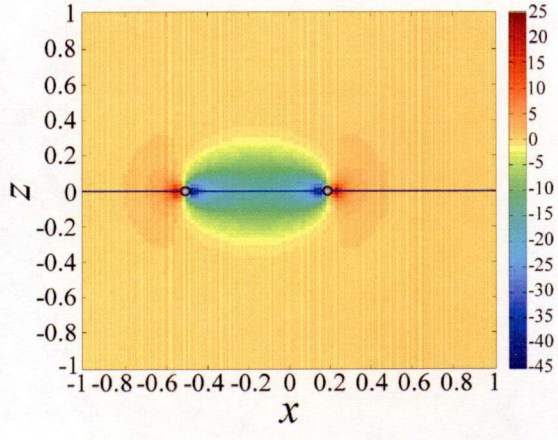

(c) σ^*_{yz} at $t^* = 0.02$

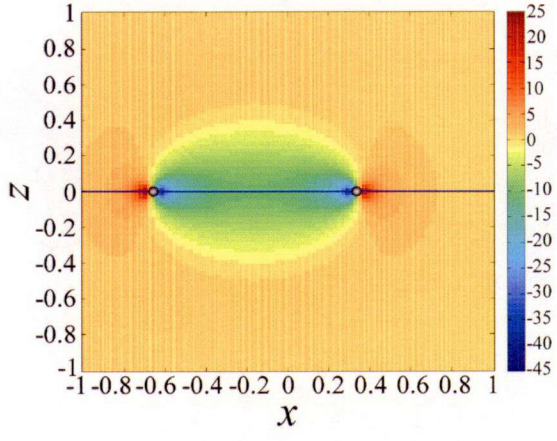

(d) σ^*_{yz} at $t^* = 0.035$

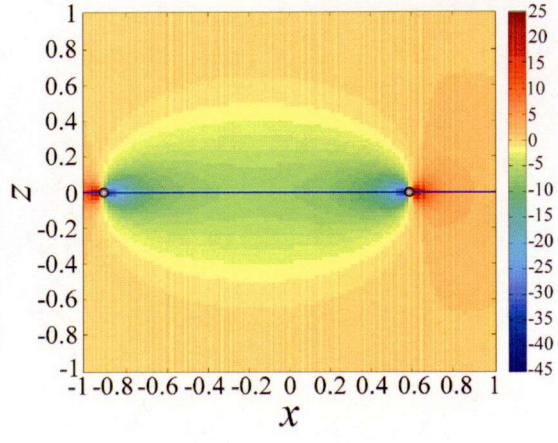

(e) σ^*_{yz} at $t^* = 0.06$

Fig. 4.6 Internal stress distributions of the loop when $\gamma = 0$, applied stress σ^*_{yz}=20.

When $\gamma = 0.6$, the β is larger than 1, the loop will glide from plane *I* to plane *II* (see Fig. 4.5(b)). When the dislocation just crept from plane *I* to plane *II*, we imaged the internal stress field of this bended dislocation loop in Fig. 4.7, similarly taking a slice of the configuration (light red plane in Fig. 4.5(b)). Figs. 4.7(a) and (b) are σ_{yx} and σ_{yz} components for Fig. 4.5(b), respectively. Figs. 4.7(c), (d) and (e) correspond to the entire processes of cross slip. Since the component σ_{yz} on the core of the dislocation is negative, this stress drives the dislocation to shrink unless a positive stress is applied. Not like the stress of Fig. 4.6(b), the elliptical negative value of σ_{yz} starts to bend over along the slip plane *II* and evolves more and more. The vicinal value of the right side dislocation also starts to rotate when dislocation crosses slip onto the inclined plane due to the asymmetry of the configuration. Viewing Figs. 4.7(c) to (e), the internal stress inside the loop still remains regardless of the different slip plane.

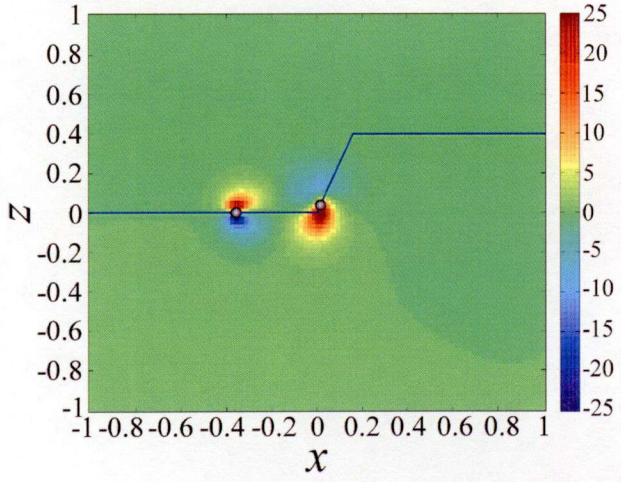

(a) σ^*_{yx} for Fig. 4.5(b)

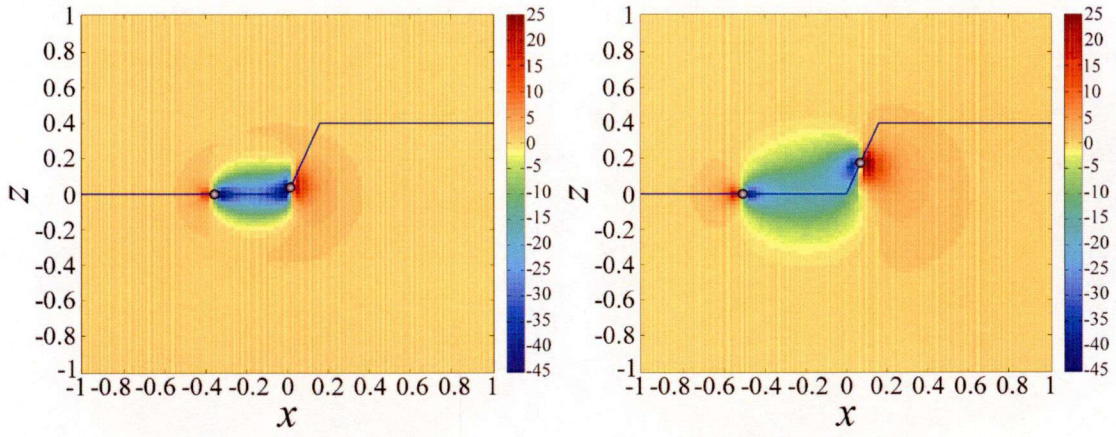

(b) σ^*_{yz} for Fig. 4.5(b)

(c) σ^*_{yz} at $t^* = 0.02$

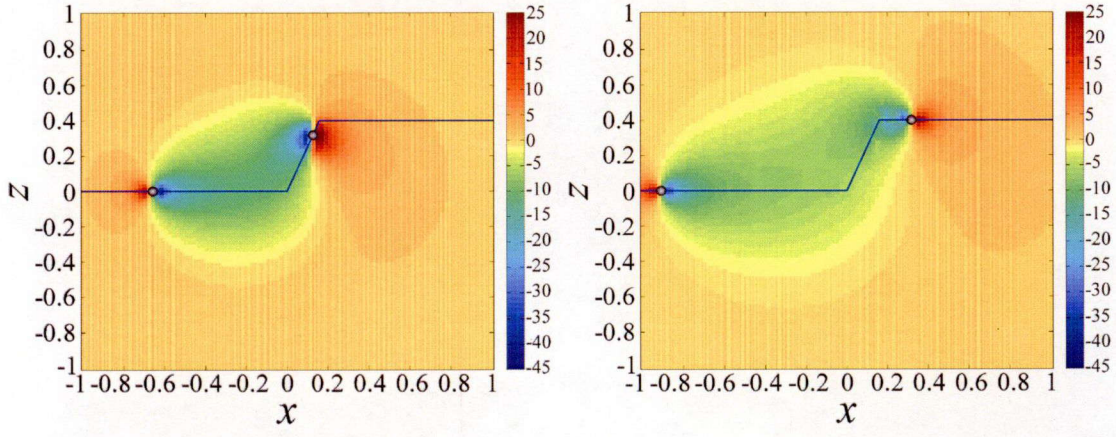

(d) σ^*_{yz} at $t^* = 0.035$

(e) σ^*_{yz} at $t^* = 0.06$

Fig. 4.7 Internal stress distributions of the loop when $\gamma = 0.6$, applied stress $\sigma^*_{yz} = 20$.

4.4.2 Effect of Internal Stress to Other Injected Dislocation

The effect of internal stress from both normal slip Orowan loop and cross-slip loop has been studied. According to the σ^*_{yz} component by which the injected negative screw dislocation segments will be drag to glide.

First we select four cross sections of *A*, *B*, *C*, *D* for a normal slip and studied how dislocation segments on these planes move (see Fig. 4.8) if negative screw dislocations P and Q were injected. The red and blue areas are attractive and repulsive regions, respectively, and the green is immobile region, all relative to the middle green line on

red plane *A* of Fig. 4.8(a), where the drag force exerted on the injected dislocation is less than the friction stress by Peierls potential (5MPa). The P segment on plane *A* is in red region (see Fig. 4.8(b)), which means it will be attracted to the middle line. When crosses the middle line, it will be repelled from the middle line to the right side. That is, the P segment will be driven rightward continuously. Then Q segment which is in blue region on plane *A*, will be repel against the middle line and glide towards the positive segment of the dislocation loop.

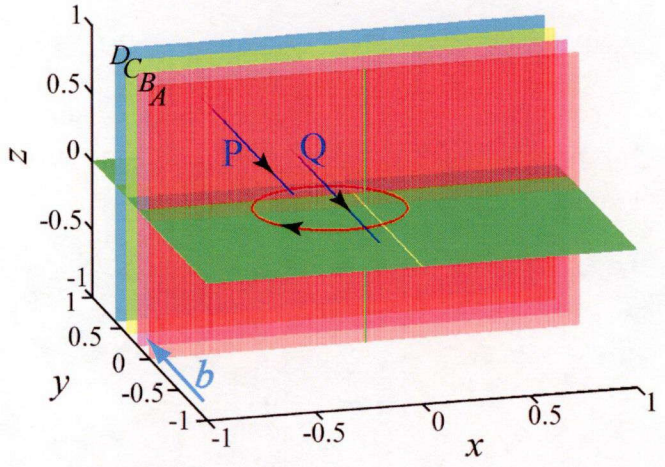

(a) Four cross sections

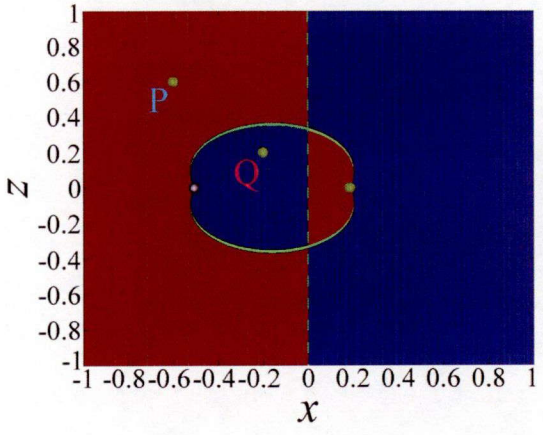

(b) Plane *A*

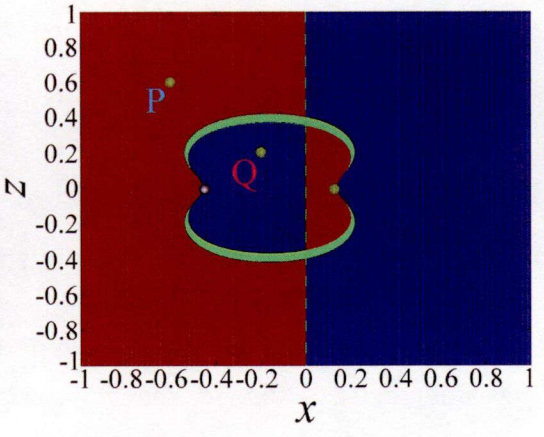

(c) Plane *B*

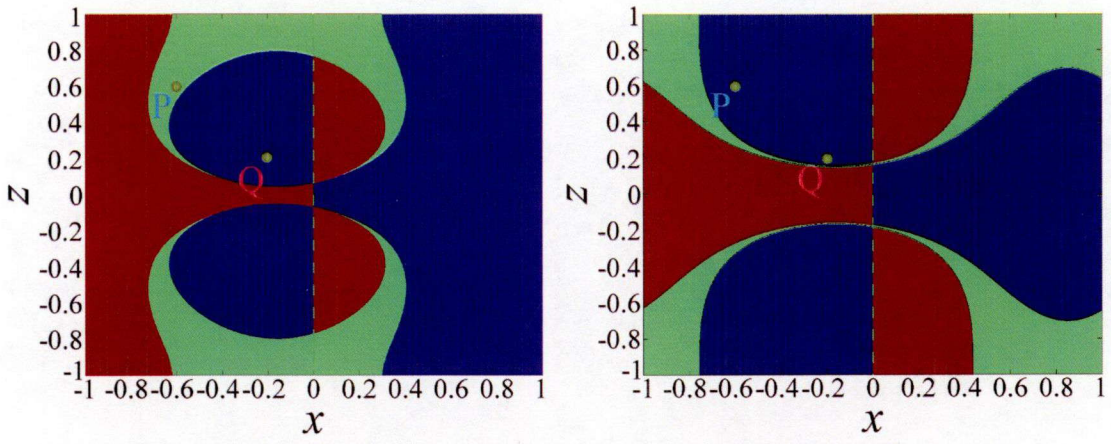

(d) Plane *C* (e) Plane *D*

Fig. 4.8 Attractive and repulsive region of four cross sections for a normal slip dislocation loop.

A cross-slip dislocation loop also has been studied similar to the normal slip loop mentioned above (see Fig. 4.9). The attractive region and repulsive region are not symmetric according to the plane of $z = 0$ since the negative screw dislocation segment crosses to the plane *II*, and the evolutions of the injected dislocations change comparing with the normal slip.

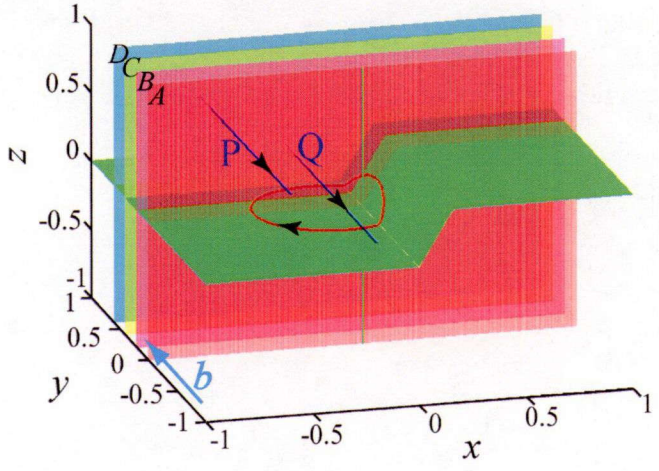

(a) Four cross sections

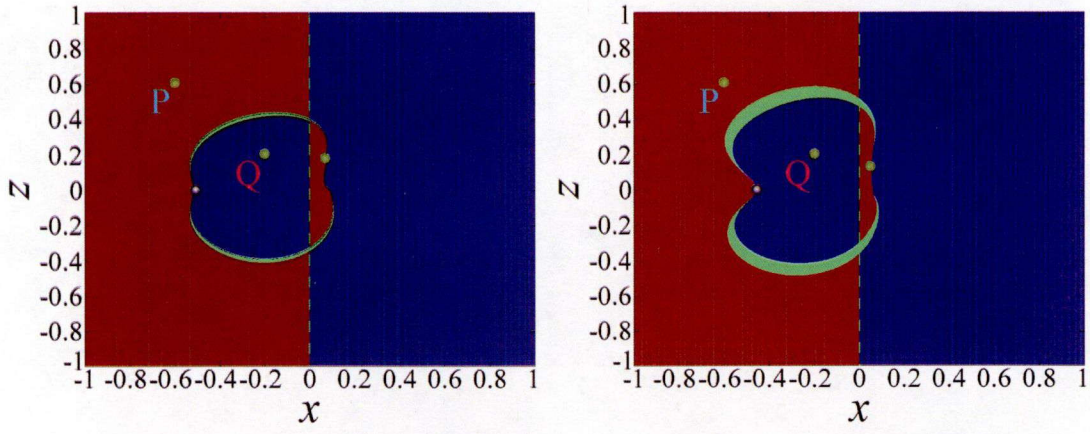

(b) Plane *A* (c) Plane *B*

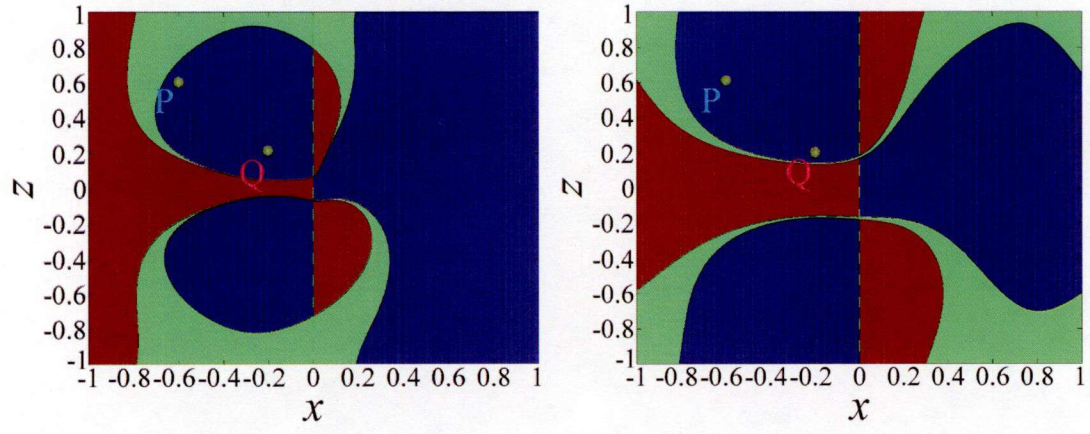

(d) Plane *C* (e) Plane *D*

Fig. 4.9 Attractive and repulsive region of four cross sections for a cross-slip dislocation loop.

4.5 Conclusion

The simulations using level set method successfully realized the cross-slip and double cross-slip. In the cross-slip simulation associated with the prescribed slip plane, when the applied external stress ratio γ between σ^*_{yx} and σ^*_{yz} is set to be 0.6 with σ^*_{yz}=20, the Peach-Koehler force on plane *II* becomes larger than that on the initial slip plane, and thus the Orowan loop starts to cross slip from plane *I* to plane *II*. Differing from the

theoretical value of γ (=0.68) for the straight dislocation model, the driving force to cross slip is much affected by the topological three dimensional effect of the loop, and the less external stress σ^*_{yx} is needed to be enforced to the field where the internal stress is superimposed.

We also discussed the internal stress distributions around the loop for the two cases of normal slip and double cross-slip. Because of the negative σ^*_{yz} component inside the dislocation core, the internal stress tends to drive the loop to shrink. The component σ^*_{yz} of applied stress makes the loop expand, while the component σ^*_{yx} tends to drag the loop upward at its right end. Thus, the internal stress σ^*_{yz} could become the barrier for the dislocation movement. When the loop is more expanded along the normal slip plane, the stress inside the loop decays but still has a long-ranged interaction. The internal stress inside the cross-slipped loop still remains regardless of the different slip plane.

Finally the effect of internal stress σ^*_{yz} has been studied by drawing the attractive and repulsive regions when a negative screw dislocation segment inserted both for normal slip and cross-slip. The attractive and repulsive regions are symmetric according to the plane of $z = 0$ for a normal slip while not symmetric for the cross-slip. As a consequence, the evolution of the injected negative screw dislocation line is much expected to be affected by the internal stress distribution.

Chapter 5

Modeling of Prismatic Dislocation Loops around a Spherical Inclusion

5.1 Abstract

Inclusions as the barriers for moving dislocations are often used for material hardening and this kind of precipitate hardening is often observed in aluminum alloy. Also inclusions are reasons for the nucleation of dislocations [100, 101] since the stress at inclusion-matrix interface is highly concentrated and the punching of coaxial prismatic dislocation loops (PDLs) in crystalline materials at precipitate-matrix interfaces without long-range applied stress is often observed by experiments. Precipitates employed in strengthening technique of quench-aging process generate misfit strain in the vicinity and constitute nucleation sites for PDLs. These misfit stresses associated with internal stresses from PDLs can be the barriers for mobile dislocations in matrix phase and thus are the reasons for precipitation hardening.

Tsuru and Shibutani [102] discussed the formation of PDL around a spherical inclusion in aluminium and investigated the stress distributions on {1 1 1} plane with different heights by molecular dynamics simulations. Their works give us a physical aspect for understanding the mechanism of PDL formation but the computational volume of material and time interval are comparatively limited. Thus we want to deliver and explain this complicated mechanism in a large scale by creating continuum models.

This chapter is organized as follows. In Section 5.2, the micromechanis of a misfitting spherical inclusion is introduced and the Peach-Koehler force from inclusion worked on dislocations is investigated. In Section 5.3, the technique of modeling open curves for level set method (LSM) is explained in order to initialize the two small half dislocation loops of the PDL formations. In Section 5.4, the formation of PDLs is

demonstrated using level set dislocation dynamics (LS-DD) with the studying of strain energy variation during the evolution.

5.2 Micromechanis of a Misfitting Spherical Inclusion and the Initialization of LSM

5.2.1 Misfit Stress Field

Consider an infinite homogeneous elastic solid D containing a spherical sub-domain Ω with the radius R (see Fig. 5.1), which undergoes a uniform permanent deformation (such as phase transformation, precipitate and recrystallization).

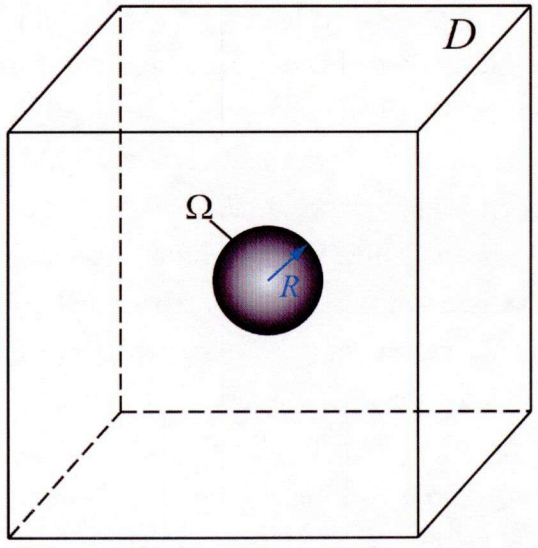

Fig. 5.1 A homogeneous elastic solid D with a spherical sub-domain Ω.

The displacement in the matrix is purely radial and decreases with radial distance as r^{-2}. Since the radial displacement u_r equals $\varepsilon_0 R$ at the inclusion-matrix interface ($r = R$),where ε_0 is the dilatational misfit strain, the displacement at r ($>R$) is [103]

$$u_r = \frac{\varepsilon_0 R^3}{r^2} \quad . \tag{5.1}$$

Therefore, the displacement components in rectangular Cartesian coordinates are

$$u_x = \varepsilon_0 R^3 \frac{x}{r^3}$$
$$u_y = \varepsilon_0 R^3 \frac{y}{r^3} \quad , \tag{5.2}$$
$$u_z = \varepsilon_0 R^3 \frac{z}{r^3}$$

where $r^2 = x^2 + y^2 + z^2$. We can get the strain tensor using Eqs. (3.2) and (3.9)

$$\varepsilon = \frac{\varepsilon_0 R^3}{r^5} \begin{pmatrix} r^2 - 3x^2 & -3xy & -3xz \\ -3xy & r^2 - 3y^2 & -3yz \\ -3xz & -3yz & r^2 - 3z^2 \end{pmatrix} \quad . \tag{5.3}$$

According to Eq. (3.11), the stress fields generated by the dilatational misfitting spherical inclusion with the radius R locating at the origin coordinate $(0, 0, 0)$ in an isotropic elastic matrix ($r > R$) is

$$\sigma = \frac{2\mu_M \varepsilon_0 R^3}{r^5} \begin{pmatrix} r^2 - 3x^2 & -3xy & -3xz \\ -3xy & r^2 - 3y^2 & -3yz \\ -3xz & -3yz & r^2 - 3z^2 \end{pmatrix} \quad , \tag{5.4}$$

where μ_M is shear modulus of matrix, ε_0 is a dilatational misfit strain and ν is Poisson ratio. Then the stress tensor inside the particle ($r < R$) can be similarly obtained as

$$\sigma = -4\mu_P \varepsilon_0 \begin{pmatrix} 1 & 0 & 0 \\ 0 & 1 & 0 \\ 0 & 0 & 1 \end{pmatrix} \quad , \tag{5.5}$$

where μ_P is shear modulus of precipitate. Then the total stress field has three aspects: stress caused by dislocation σ^{dis}, stress generated by inclusions σ^{inc} and applied stress σ^{app}:

$$\sigma^{tot} = \sigma^{dis} + \sigma^{inc} + \sigma^{app} \quad . \tag{5.6}$$

It is easy to see the maximum shear stress (MSS) at the inclusion-matrix interface is on the cylinder surface of radius $R/\sqrt{2}$ (see Fig. 5.1), where MSS meets the critical shear stress for dislocation nucleation and, as a result, small half loops are punched out [20, 101].

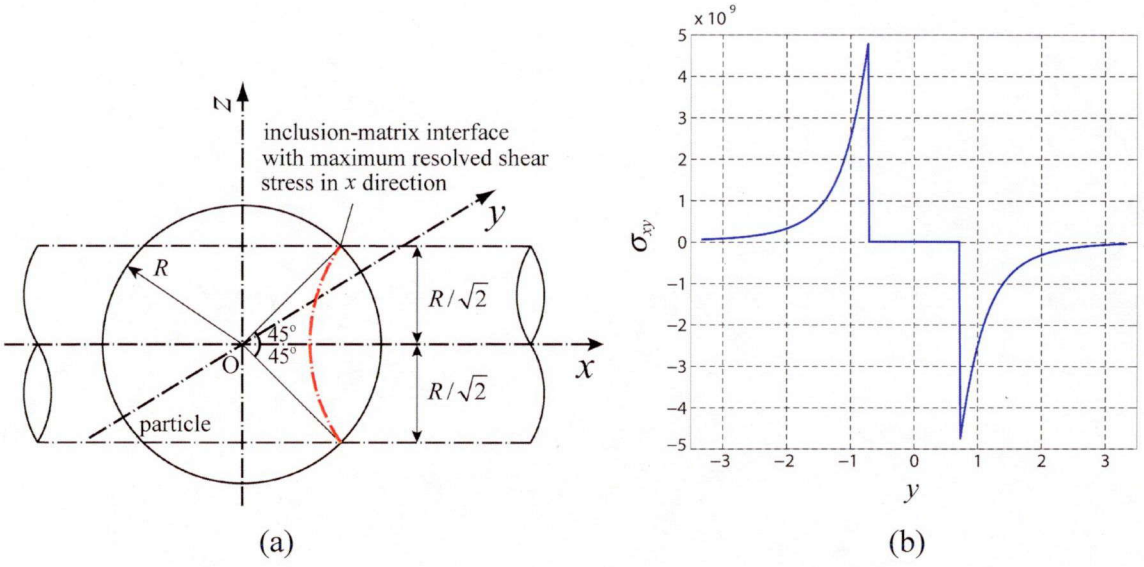

(a) (b)

Fig. 5.1 (a) A misfitting spherical inclusion and the cylindrical surface with maximum resolved shear stress in x direction. (b) σ_{xy} on the red cross-section ($x = R/\sqrt{2}$) of Fig. 5.1(a) at $z = 0$ (μ_M=161GPa, ε_0=0.01, R=0.3).

5.2.2 Punching of Initial Dislocation Loops

The present paper mainly focuses on the morphological evolution of dislocation driven by the right elastic field. Therefore, the nucleation of dislocation at the inclusion-matrix interface is computationally modeled as below.

The nucleation of dislocations happens where stress is very concentrated. The stress required to nucleate a dislocation loop with radius equal to r_c [20] is

$$\tau = \frac{\mu_M b}{4\pi r_c}[\ln(\frac{2r_c}{r_0}) + 1] \quad . \tag{5.7}$$

where r_0 is the radius of dislocation core. As we can see, $\tau \approx \mu_M/50$ for the nucleation of a dislocation loop with radii $r_c \approx 15b$ and r_0 taken as $2b$. The MSS at the inclusion-matrix interface is given from Eq. (5.4) with ε_0 given as 0.01 is

$$\tau_{max} = 3\varepsilon_0\mu_M \approx \mu_M/33 \ , \tag{5.8}$$

that is, the MSS generated from the inclusion exceeds the critical stress for nucleating dislocation loops with the radius equaling to $15b$, and we assume two small half

dislocation loops are emitted on the cylindrical surface with the radius equaling to $R/\sqrt{2}$ in the matrix (see Fig. 5.2).

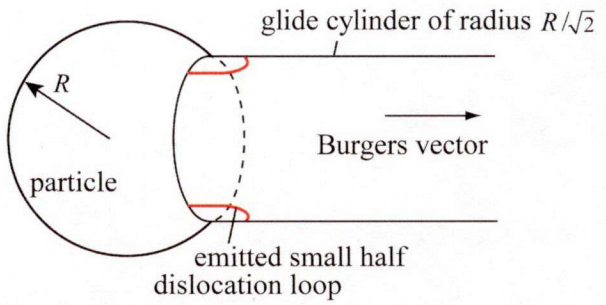

Fig. 5.2 Schematic diagram of two small half loops emitted around a spherical inclusion generating a shear stress which exceeds the critical stress for dislocation loop nucleation.

5.2.3 Peach-Koehler Force Worked on Dislocations

When two small half dislocation loops are punched out around a misfitting spherical inclusion, these dislocation loops are driven by the misfit stress field of Eq. (5.4) and expand on the cross-slip plane until they merge with each other [104, 105]. Then, this dislocation loop becomes a PDL and glides away from inclusion-matrix interface to relax the strain energy. We study the Peach-Koehler force worked on edge dislocations and on PDLs for convenience in discussing the mechanism of PDL formation. In this chapter, [1 0 0], [0 1 0] and [0 0 1] are referred to x, y and z directions, respectively.

We first consider edge dislocations with orientation [0 -1 0] (in the -y direction) and the Burgers vector $\boldsymbol{b}^* = [1\ 0\ 0]$ (normalized by b: the magnitude of Burgers vector $\boldsymbol{b}$ and oriented in the x direction), as shown in Fig. 5.3. A spherical particle of radius $R = 100b$ with the dilatational misfit strain $\varepsilon_0 = 0.015$ is located at origin (see Fig. 5.3(a)). The Peach-Koehler force worked on edge dislocation segments distributed on x-z plane when $y = 0$ (the gray slice of Fig. 5.3(a)) is investigated (see Fig. 5.3(b)). We can see that when an edge dislocation is at top right of the spherical particle, the Peach-Koehler force f_x^* (scaled by μ_M; $f_x^* = f_x^{PK} / \mu_M$ as μ_M = 161GPa) is positive which means this edge dislocation will be driven away from the inclusion, while when an edge dislocation is at bottom right area, the force is negative and the dislocation will be attracted toward the inclusion. The force on the left half area becomes an opposite manner.

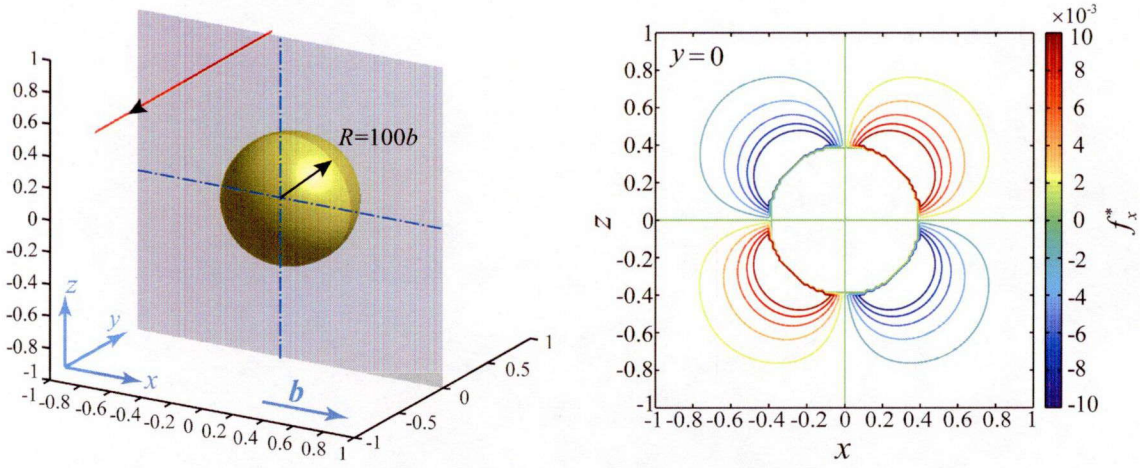

(a) x-z plane (y = 0) (b) Force in x direction

Fig. 5.3 Peach-Koehler force worked on edge dislocations around a misfitting spherical inclusion on the gray slice.

When a PDL with clockwise orientation (according to the x direction) is produced (see the red circle of Fig. 5.4(a)), this PDL receives a repel force paralleling to Burgers vector. We investigate the Peach-Koehler force f_x^* on the homocentric PDL on the plane of x = 0.6 (see the gray slice of Fig. 5.4(a)), and draw a image figure of the force in order to see the gradual change (see Fig. 5.4(b)). The force first radially increases as the radius of the dislocation loop increases from zero and reaches the maximum 4.6×10^{-3} when the radius of the loop reaches $R/\sqrt{2}$ (black dashed circle), and then decreases as the radius of the loop increases. Since the equality of the magnitude of the force on each segment for each individual PDL, the PDL glides away from the inclusion-matrix interface keeping its shape.

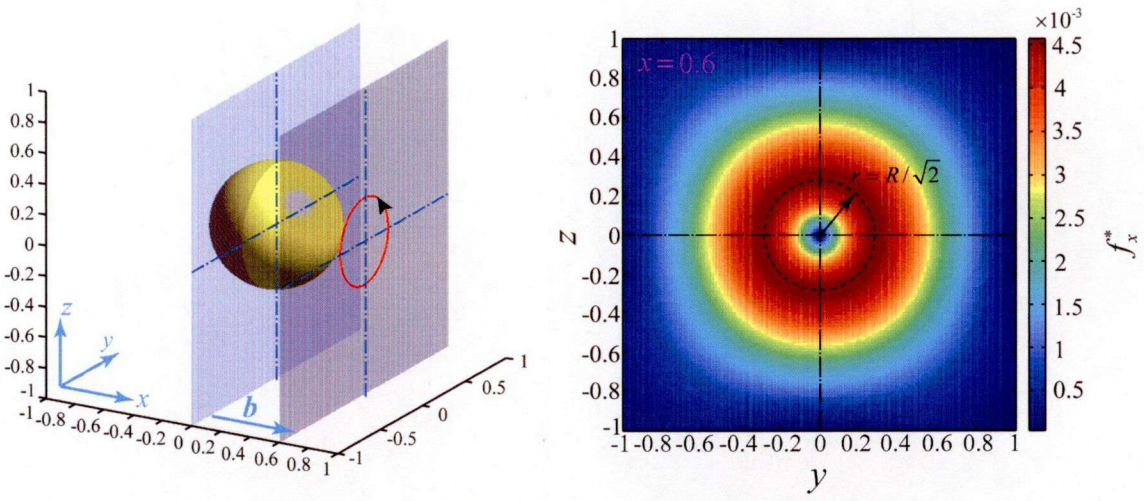

(a) y-z plane (x = 0.6) (b) Force in x direction

Fig. 5.4 Peach-Koehler force worked on PDLs around a misfitting spherical inclusion on the gray slice.

5.3 Representing Open Curves using LSM

LSM is used to represent closed curves that either loops or lines with ends located at the boundaries of the computational region. However, there exist problems that ends of the curves located within computational region. Smereka [106] used an additional level set function with the codimension-two intersection points of two level set functions to represent ends of curves (see Fig. 5.5).

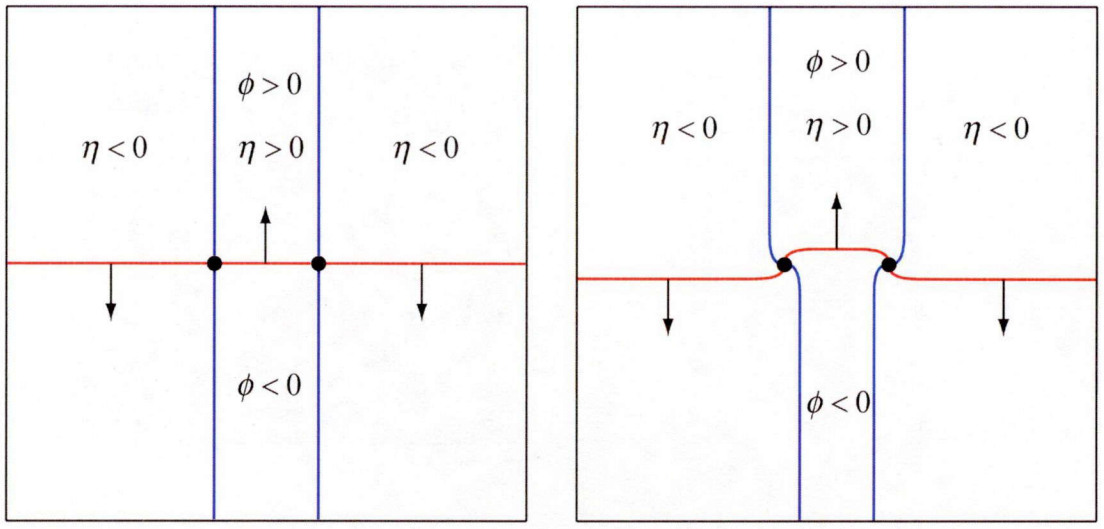

(a) (b)

Fig. 5.5 Representing an open curve with an additional level set function η. (a) Initial stage. (b) A slightly later time.

The curve of interest is defined as the $\phi = 0$ isocontour in the region where $\eta > 0$ (part of red curve between two black intersection point, see Fig. 5.5), while a ghose curve is defined as the $\phi = 0$ isocontour in the region where $\eta < 0$ (two parts of red curve outside two black intersection point).

Then we show an example of the spiral crystal growth of an open curve (see Fig. 5.6), so called Frank-Read source mechanism. The curve of interest defined as $\Gamma(t) = \{\phi(\boldsymbol{x},t) = 0, \eta(\boldsymbol{x},t)>0\}$ evolves under the velocity given as

$$v = \mathrm{sgn}(\eta)\frac{\nabla\phi}{|\nabla\phi|}(1 - \lambda\,\mathrm{sgn}(\eta)\kappa(\phi)) \quad , \tag{5.9}$$

where sgn is a sign function, κ is local curvature and λ is a constant.

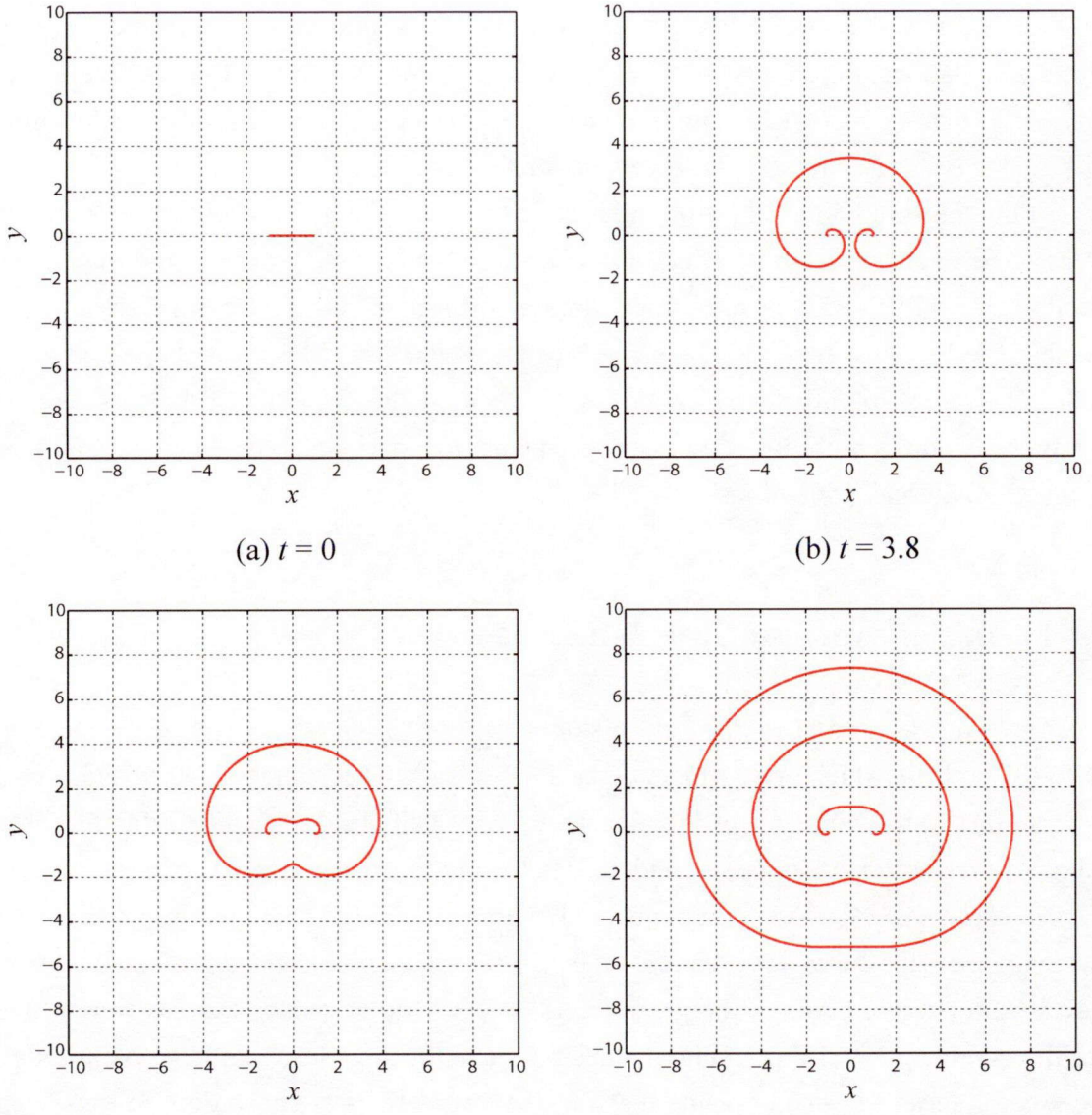

Fig. 5.6 Spiral crystal growth of an open curve.

5.4 Simulation Results

In this section, we present the formation of PDL using LS-DD. The simulations were performed using the simulation cell which one side l has plus and minus units normalized by the real length of 250b (b denotes the magnitude of Burgers vector, 0.286 nm). The cell box is divided into 64×64×64 grid points. The shear modulus μ_M and μ_P

are set to be 161GPa and 80GPa, respectively, and Poisson ratio ν is set to be 1/3. For all the calculations, the stresses are scaled by $3\mu_M b(1-\nu)/(2l(1+\nu))$ and time is scaled by $2l/(\mu_M m_g)$ (that is, $t^* = t/(2l/\mu_M m_g)$) where m_g is the mobility constant for dislocation glide and is set be 1.0 in the present calculations.

During the simulations, the fifth order weighted essentially non-oscillatory (WENO) is used for spatial differentiation and the third order total variation diminishing Runge-Kutta (TVD-RK) is used for temporal differentiation [7]. Reinitializations for keeping the level set functions be signed distance function (SDF) are performed after each time step of solving the evolution Eq. (2.19) to reduce the numerical errors. We do not present climb mobility if not specified and the periodic boundary condition is assumed in x, y and z directions.

5.4.1 Initialization of Two Half Dislocation Loops

To represent two initial small half dislocation loops, we create two hypersurfaces (ϕ=ψ=0) both of which are cylinders (see Fig. 5.7(a)). The intersections of these two hypersurfaces are two small dislocation loops with half inside the inclusion (see blue "ghost curves" in Fig. 5.7(b)) and with half in the matrix (red "curves of interest" in Fig. 5.7(b)). The value of ψ is positive outside the green cylinder (ψ=0) and negative inside the cylinder. The upper intersection loop has the clockwise orientation since ψ first varies from positive through the green interface (ψ=0) to negative, and the bottom one has the counterclockwise orientation since the value of ψ varies from negative through the green interface (ψ=0) to positive again (the orientations are according to top-down view as shown in Fig. 5.7(a)).

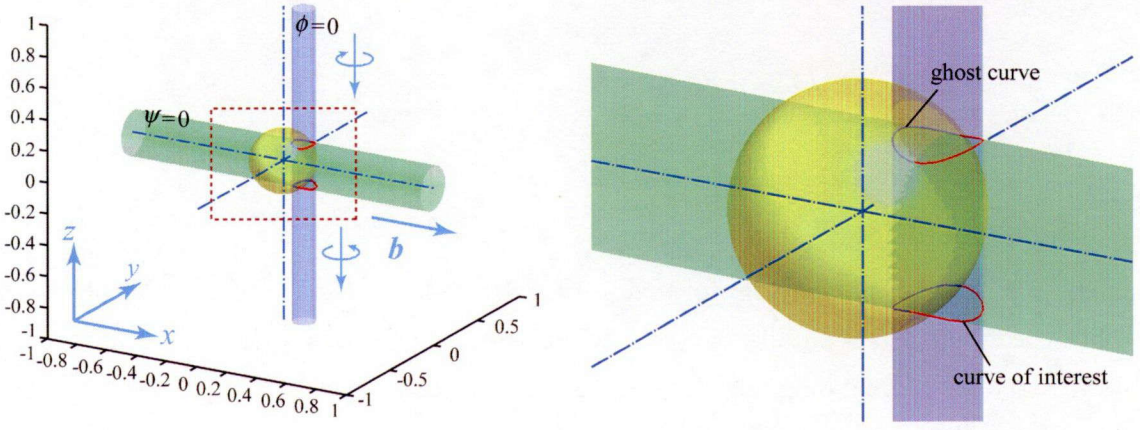

(a) (b)

Fig. 5.7 (a) Representing two small dislocations loops by two hyperplanes (ϕ=ψ=0) with half loops in the matrix (red curves) and half inside the inclusion (blue curves); (b) Zoom in of the dashed rectangle of (a).

The curves of interest Γ^{I} (red curves) are the intersections of $\phi = 0$ and $\psi = 0$ outside the spherical inclusion, while the segments inside the inclusion surface (blues curves) are treated as ghost curves Γ^{G} [7] which are not taken into account in the simulations [7]. These two types of curves are defined as

$$\begin{cases} \Gamma^{I}(\boldsymbol{x},t) = \{\phi(\boldsymbol{x},t) = 0,\ \psi(\boldsymbol{x},t) = 0,\ \boldsymbol{x} \in V \setminus \bar{\Omega}\} \\ \Gamma^{G}(\boldsymbol{x},t) = \{\phi(\boldsymbol{x},t) = 0,\ \psi(\boldsymbol{x},t) = 0,\ \boldsymbol{x} \in \bar{\Omega}\} \end{cases}, \tag{5.10}$$

where V represents the whole calculation region and Ω represents the region of the spherical particle (yellow ball of Fig. 5.7(a)). And also we replace the tangent vector ξ of Eq. (3.30) by

$$\xi^{\text{dis}} = \delta(\boldsymbol{x})\xi\ , \tag{5.11}$$

where δ function is defined as:

$$\delta(\boldsymbol{x}) = \begin{cases} 1 & \boldsymbol{x} \in V \setminus \bar{\Omega} \\ 0 & \boldsymbol{x} \in \bar{\Omega} \end{cases}. \tag{5.12}$$

The Eqs. (5.10) and (5.11) are used to make sure that the half parts embedded in the inclusion do not contribute internal stress to the whole region and thus Γ^{G} can be negligible.

5.4.2 Mechanism of Prismatic Dislocation Loop Formation

In this simulation, we specify a misfitting spherical particle of radius $R = 50b$ with the dilatational misfit strain ε_0= 0.01 and the normalized Burgers vector $\boldsymbol{b}^* = [1\ 0\ 0]$ defined on both inclusion and matrix. During the whole calculation, this spherical particle keeps invariable and produces a misfit stress field according to Eq. (5.4) in a homogeneous isotropic matrix ($r > R$) and the stress tensor according to Eq. (5.5) inside the inclusion ($r < R$), respectively. As indicated in subsection 5.2.3, the magnitude of the misfit stress field reaches the maximum on the cylindrical surface of the radius $R/\sqrt{2}$ with the axis paralleling to the Burgers vector (see the light green cylinder of Fig. 5.8(a)). When

the MSS ($\mu_M/33$) exceeds the critical stress for nucleation of dislocation loops of radius equal to $15b$ ($\mu_M/100$), two small half dislocation loops are injected of which the half loop on top has the clockwise orientation and the bottom one has the anticlockwise orientation (according to top-down view as Fig. 5.8 (a)). Thus, the farthest segments of the two half loops are edge dislocations and the segments on the inclusion-matrix interface are screw dislocations. The velocity vector of the dislocation evolution is projected onto the cross-slip plane (light green cylinder) to make sure that the dislocations always receive the maximum shear stress from the inclusion among all the slip planes.

Under the shear stress generated by the inclusion, the forward edge components glide away from the inclusion-matrix interface by repel force and the screw components paralleling to the axis of the glide cylinder experience a force causing them to cross slip around the circular surface of the cylinder (see Fig. 5.8 (b)). As the half loops are expanding on the cylinder, the two screw components with opposite orientations of the two half loops approach to each other (see Fig. 5.8 (b)), and annihilate when two half dislocation loops merge. Finally they become one dislocation loop (see Fig. 5.8 (c)). The middle mixed dislocation segments experience more intense shear stress than top and bottom edge dislocation segments and also internal stress of dislocation acting like line tension of the loop. Therefore, the middle-bended dislocation loop preferably becomes a prismatic dislocation loop with all the segments perpendicular to the Burger vector (see Fig. 5.8 (d)). This PDL glides along the cylinder surface away from the inclusion-matrix interface (as seen in Fig. 5.8 (e), the loop can only glide on the cylinder because any other motions need climb mobility). Since the influence of the stress decreases as the distance from inclusion to dislocation increases (see Eq. (5.4)), the driving force on the PDL gradually weakens. At last, the motion ceases at the position where the driving force is no larger than friction stress by Peierls potential (τ_{PN}=5MPa).

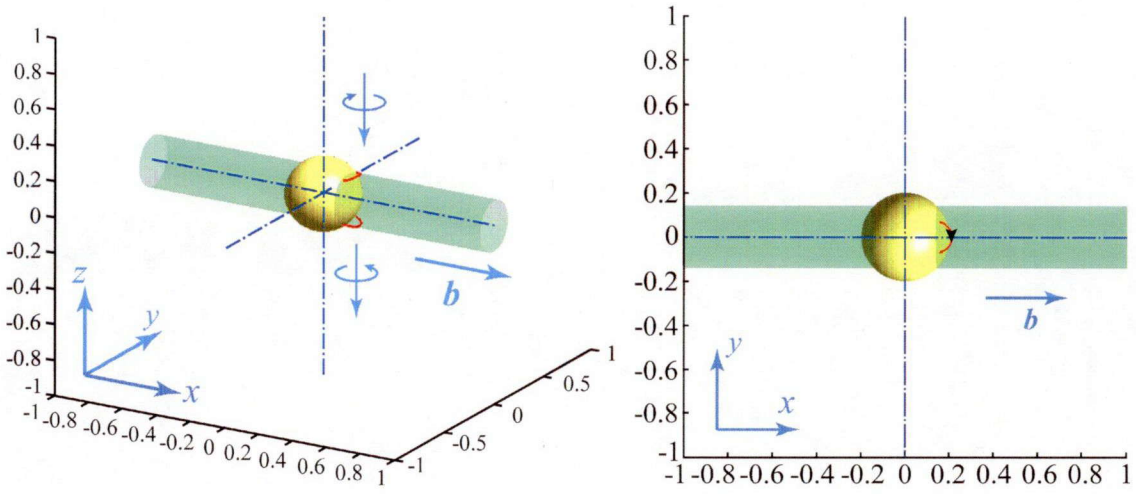

(a) $t^* = 0$

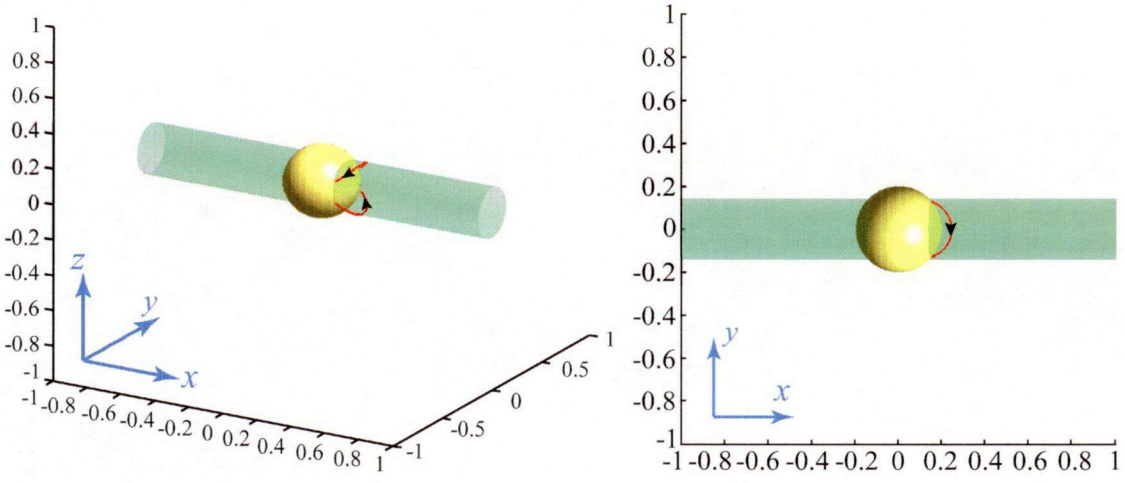

(b) $t^* = 0.08$

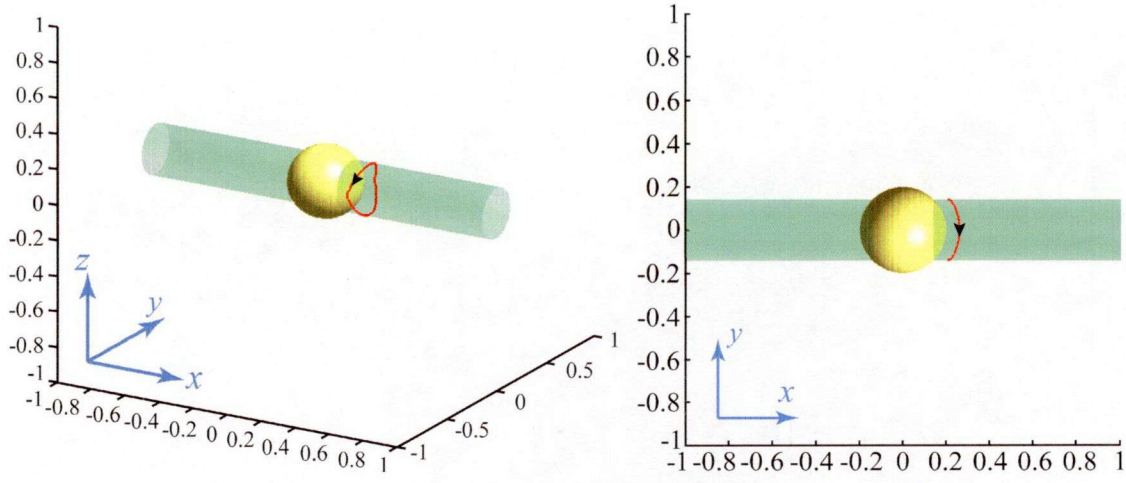

(c) $t^* = 0.16$

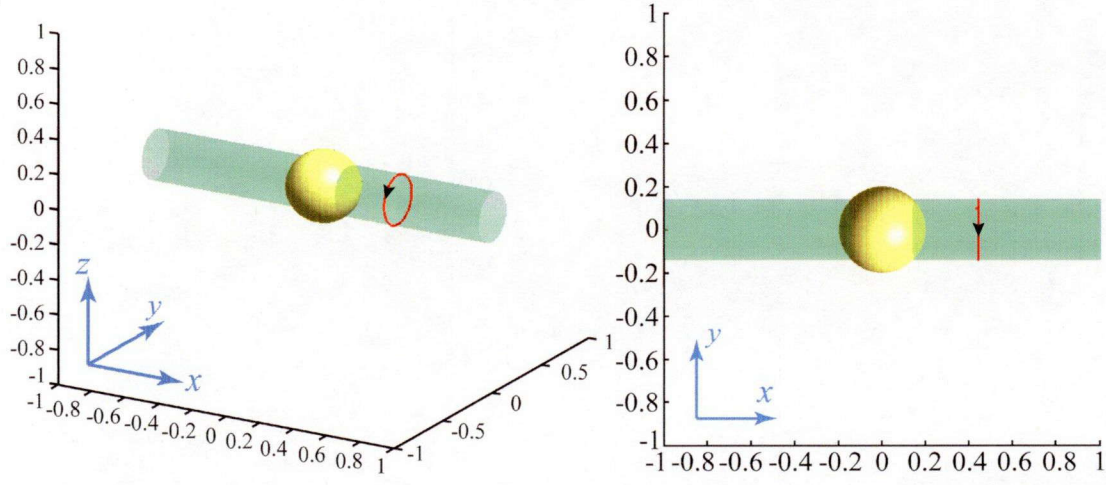

(d) $t^* = 0.85$

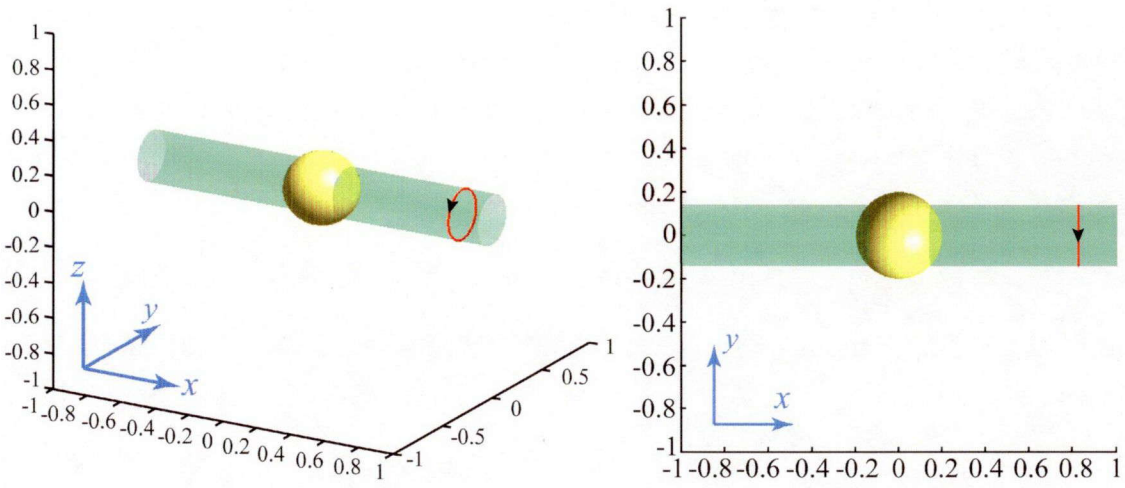

(e) $t^* = 2.5$

Fig. 5.8 Formation of a PDL under the shear stress generated by a misfitting spherical inclusion of radius $R = 50b$ with the dilatational misfit strain $\varepsilon_0 = 0.01$ in a homogeneous isotropic medium. The left column shows a three-dimensional view and the right column shows a top-down view.

5.4.3 Strain Energy Variation during the Process

The elastic strain energy is defined as the integration of the multiplication of stress field and strain field in the whole volume V [23], [24]:

$$E_{\mathrm{el}} = \frac{1}{2}\int_V \sigma_{ij}\varepsilon_{ij}\mathrm{d}\boldsymbol{x} = \frac{1}{2}\int_V C_{ijkl}\varepsilon_{kl}\varepsilon_{ij}\mathrm{d}\boldsymbol{x} \quad , \tag{5.13}$$

where $\mathrm{d}\boldsymbol{x} = \mathrm{d}x\mathrm{d}y\mathrm{d}z$. When two origins (inclusion and dislocation) generating stress field coexist, the total stress is the superposition of them in the linear elastic framework:

$$E_{\mathrm{el}}^{\mathrm{tot}} = \frac{1}{2}\int_V (\sigma_{ij}^{\mathrm{inc}} + \sigma_{ij}^{\mathrm{dis}})(\varepsilon_{ij}^{\mathrm{inc}} + \varepsilon_{ij}^{\mathrm{dis}})\mathrm{d}\boldsymbol{x} \quad , \tag{5.14}$$

and Eq. (5.14) can be expanded as

$$E_{\mathrm{el}}^{\mathrm{tot}} = \frac{1}{2}\int_V \sigma_{ij}^{\mathrm{inc}}\varepsilon_{ij}^{\mathrm{inc}}\mathrm{d}\boldsymbol{x} + \frac{1}{2}\int_V \sigma_{ij}^{\mathrm{dis}}\varepsilon_{ij}^{\mathrm{dis}}\mathrm{d}\boldsymbol{x} + \frac{1}{2}\int_V \sigma_{ij}^{\mathrm{inc}}\varepsilon_{ij}^{\mathrm{dis}}\mathrm{d}\boldsymbol{x} + \frac{1}{2}\int_V \sigma_{ij}^{\mathrm{dis}}\varepsilon_{ij}^{\mathrm{inc}}\mathrm{d}\boldsymbol{x} \quad , \tag{5.15}$$

where σ^{inc} and ε^{inc} indicate the stress and strain fields of matrix caused by inclusion and σ^{dis} and ε^{dis} due to the case by dislocation. The first two terms of the right side of Eq. (5.15) are strain energy generated by inclusion and dislocation, respectively. And the last two terms are elastic interaction energy for the coexistence of inclusion and dislocation. Due to the symmetry of elastic constant:

$$C_{ijkl} = C_{klij} \quad , \tag{5.16}$$

the third and fourth terms of Eq. (5.15) should be equal. The Eq. (5.15) can thus be written as

$$E_{el}^{tot} = E_{el}^{inc} + E_{el}^{dis} + E_{el}^{int} \quad . \tag{5.17}$$

where E_{el}^{inc}, E_{el}^{dis}, E_{el}^{int} are elastic strain energy caused by inclusion, dislocation and dislocation-inclusion interaction, respectively. During the whole process of PDL formation, the E_{el}^{inc} keeps unvaried ($E_{el}^{*inc} = E_{el}^{inc} / (\mu_M b^3) = 716.9$), so we just focus on E_{el}^{*dis} and E_{el}^{*int} which are scaled by $\mu_M b^3$ (see Fig. 5.9). The process is divided into three stages depending on different topological shapes of the dislocation. During the step I (computational step t^* from 0 to 0.12), two small loops expand along the cross-slip cylindrical surface. The E_{el}^{*dis} quickly increases since the total length of the dislocation is rapidly enlarged. While the E_{el}^{*int} also quickly increases and reaches the climax when two loops merge and the pure screw segments annihilate. At stage II (t^* from 0.12 to 0.85), the E_{el}^{*dis} decreases when the middle-bended loop becomes a PDL as a consequence of the total length of the loop intending to be shorten energetically. The E_{el}^{*int} decreases since the dislocation loop glides away from the inclusion-matrix interface. At stage III (t^* from 0.85 to the end), the PDL continues to glide along the cylinder away from inclusion-matrix interface and therefore E_{el}^{*int} continues to decrease. Since there is no dislocation deformations, the E_{el}^{*dis} does not obviously change.

As discussed above about the elastic strain energy caused by inclusion, dislocation and dislocation-inclusion interaction, we can obtain the total strain energy variation during the whole process (see the blue curve of Fig. 5.9). As the small dislocation is punched out and expanded along the cross-slip cylindrical surface, the total strain energy quickly increases since the total length of the dislocations is extended and interaction energy dramatically increases (stage I). After that, E_{el}^{*tot} decreases since the total dislocation loop length shortens and the PDL moves away from the interface (stage II and III). Finally, it flattens at stage III because no obvious deformation of dislocation is observed and dislocation- inclusion interaction becomes weaken.

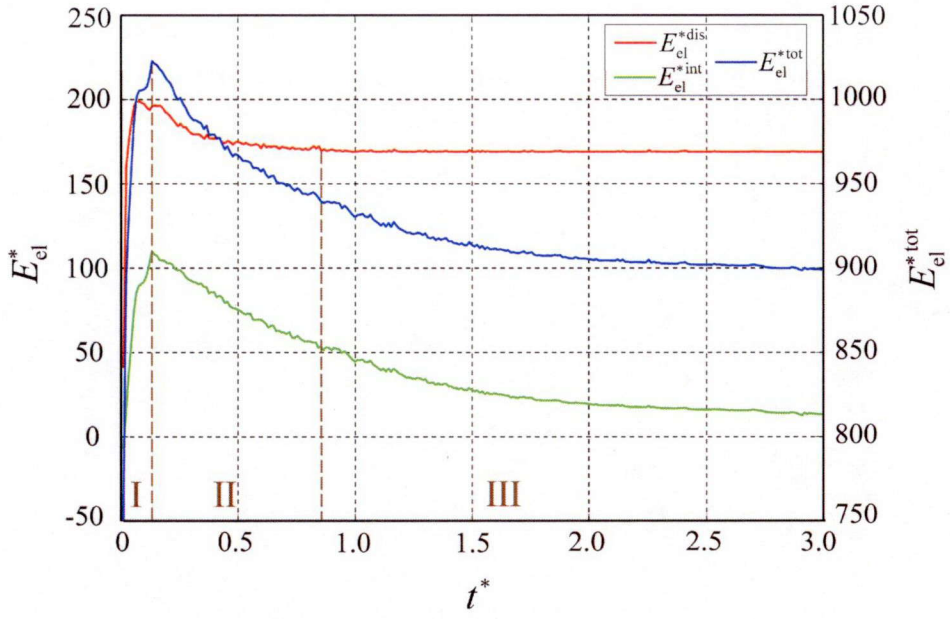

Fig. 5.9 Strain energy (caused by dislocation and dislocation-inclusion interaction, respectively) and total strain energy variation during the process of PDL formation around a misfitting spherical particle of radius $R = 50b$ with the dilatational misfit strain $\varepsilon_0 = 0.01$.

5.5 Conclusion

The simulations using LSM successfully realized the formation of PDL. On the glide cylinder where the inclusion-matrix interface meets the maximum resolved shear stress, two small half loops with opposite orientations are punched out. The forward edged segments are repelled from the inclusion, while the screw segments cross slip around the circular surface of the cylinder. Making the loops approaching to each other, the screw dislocations with opposite directions annihilate as two half loops merge and then become a middle-bended loop. Finally the middle-bended loop becomes a prismatic dislocation loop and glides along the cylinder until the driving force becomes less than friction (Peierls barrier).

We also studied the elastic strain energy variation during the process of PDL formation. The total strain energy first increases as the initial two small half dislocation loops expand and reaches the climax when two loops merge. Then, the strain energy quickly decreases as the loop approaches a perfect prismatic loop. After that, the PDL

glides relatively fast since misfit shear stress is intensive near the inclusion. Finally, as the moving of the PDL slows down without any deformation of dislocation, the decreasing of the strain energy also becomes slow until the PDL stops.

Chapter 6

Summaries

This thesis has presented a series of dislocation evolutions using level set method (LSM) in the base of elastic theory for dislocation. Dislocation as the line defect in solid decides many mechanical properties of crystalline materials, especially the ability for plastic deformation. The strain-stress relationships have been made for materials, where dislocations move immediately after the elastic deformation. This is the reason why materials cannot resume the original shapes even after unloading, so called "plasticity". Therefore, for its importance and complexity, dislocation draws lots of attentions in both academic and industrial fields.

In chapter 2, we have introduced LSM coupled with fast marching method (FMM) and shown extreme success of topological evolutions of interfaces especially when merging and breaking occur. FMM is utilized for creating signed distance functions (SDFs) with demanded implicit interfaces as initial functions for level set evolutions and is also associated with the determination of extension velocities. In that case, the level set functions can always preserve SDFs during the evolutions. The preservation of smooth distribution for values is significant for preventing the diffusion of the interface since the partial derivatives with stencil of several grids length of the functions are taken. Furthermore, representation of codimension-two objects by two level set functions is introduced, which makes the demonstration of curves in three dimensions available.

In chapter 3, we have shown a series of models of dislocation evolutions based on level set dislocation dynamics (LS-DD) in three dimensions. Based on the complex internal stress fields solved efficiently by FFT under the periodic boundary condition, the prismatic dislocation loop (PDL) shrinks automatically at an equivalent high temperature and dislocation curves interact with the others. An Orowan loop expands or rotates from its original slip plane under the applied shear stress fields. We have also successfully seen the formation of an Orowan loop from a gliding linear edge dislocation under an applied stress when it meets an impenetrable particle.

In chapter 4, we have also realized the phenomena of cross-slip and double cross-slip of an Orowan loop which the screw segment reacts at the edge of cross-slip plane. With the aid of the moving curves on specific surfaces technique, the expanding loop can choose to cross slip from initial slip plane when the Peach-Koehler force projected on the cross-slip plane becomes larger than the initial one under the applied shear stresses. We have investigated the internal stress of the cross-slipped dislocation loop and studied the effects to the other dislocations from the distorted loop in comparison with the case of a normal expanding Orowan loop.

In chapter 5, we have successfully demonstrated the formation of PDLs. Firstly two small half loops with opposite orientations are punched out on a cylindrical surface where the inclusion-matrix interface meets the maximum resolved shear stress. Then, the forward edged segments are repelled from the inclusion while the screw segments cross slip around the circular surface of the cylinder and approach to each other. Two half dislocation loops merge into a middle-bended loop when two screw segments with opposite orientations meet and annihilate. Finally, the middle-bended loop becomes a PDL. Afterwards the PDL glides away from the inclusion along the cylindrical surface until the driving force becomes less than the frictional stress (Peierls barrier). Since the series of movements happen automatically, we studied the elastic strain energy variation during the whole process. The total strain energy first increases and reaches the climax when two loops merge as the initial two small half dislocation loops expand. Then, the strain energy quickly decreases as the loop becomes a perfect PDL. After that, the PDL glides relatively fast since misfit shear stress is intensive near the inclusion and the decreasing of strain energy is also relatively quick. Finally as the moving of the PDL slows down keeping the same shape, the decreasing of strain energy also becomes slow.

Now at the end of this thesis, which so far has been focused on the complicate dislocations description in three dimensions, it is natural to raise the question: can we demonstrate the interactions of between the linear dislocation and the other point and planar defects? And can we extend this method to more macroscopic field keeping the unpredictable internal stress field due to the complicate morphology of dislocation? It is quite challengeable subject which should be overcome for the prospective multi-scale modeling of materials. It is hoped that LSM with the powerful ability for manipulating topological evolutions of multi-codimensional objects would be the best candidate for this kind of methodology.

References

[1] V. Volterra. *Sur l' équilibre des corps élastiques multiplement connexes.* Annales Scientifiques de l' École Normale Supérieure, Sér. 3(24): 401-517, 1907.

[2] G. I. Taylor. *Plastic Deformation of Crystals.* Proceedings of the Royal Society of London, Vol.145: 362-404, 1934.

[3] M. Polanyi. *Lattice Distortion which Originates Plastic Flow.* Zeitschrift fur Physik, Vol.89(9-10): 660-662, 1934.

[4] E. Orowan. *Plasticity of Crystals.* Zeitschrift fur Physik, Vol.89(9-10): 605-659, 1934.

[5] V. V. Bulatov, W. Cai. *Computer Simulations of Dislocation.* Oxford University Press, 2006.

[6] A. Luft, L. Kaun. *Electron Microscopic Investigation of the Dislocation Structure in Molybdenum Single Crystals Deformed in Tension at 293 and 493K.* Phys. Stat. Solid, Vol.37: 781-793, 1970.

[7] A. Seeger, J. Diehl, S. Mader, H. Rebstock. *Work-hardening and Work-softening of Face-centred Cubic Metal Crystals.* Phil. Mag., Vol.2: 323-350, 1957.

[8] E. Carrasco, O. Rodriguez de la Fuente, M. A. Gonzalez, J. M. Rojo. *Dislocation Cross Slip and Formation of Terraces around Nanoindentations in Au(001).* Phy. Rev. B, Vol.68: (180102), 2003.

[9] E. O. Hall. *The Deformation and Ageing of Mild Steel.* Proc. Phys. Soc. B, Vol.64: 747- 753, 1951.

[10] N. J. Petch. *The Fracture of Metals.* Progr. in Metal. Phys., Vol.5: 1-52, 1954.

[11] J. W. Mitchell. *Crystals of Silver Chloride with a Low Density of Dislocations, Growth and Perfection of Crystals.* New York: John Wiley & Sons, pp.386-389, 1958.

[12] J. R. Patel. *Impurity Clustering Effects on Dislocation Generation in Silicon.* Discussion of the Faraday Society, Vol.38: 201-210, 1964.

[13] A. Eikum, G. Thomas. *Precipitation and Dislocation Nucleation in Quench-aged Al-Mg Alloys.* Acta Metallurgica, Vol.12: 537-545, 1964.

[14] X. J. Xin, G. S. Daehn, R. H. Wagoner. *Equilibrium Configuration of Coaxial Prismatic Dislocation Loops and Related Size-dependent Plasticity.* Acta Materialia, Vol.45: 1821-1836, 1997.

[15] A. Giannattasio, S. Senkader, R. J. Falster, P. R. Wilshaw, *Generation of Dislocation Glides Loops in Czochralski Silicon.* Journal of Physics: Condensed Matter, Vol.14: 12981-12987, 2002.

[16] J. W. Mitchell. *Crystals of Silver Chloride with a Low Density of Dislocations, Growth and Perfection of Crystals.* New York: John Wiley & Sons, pp.389, 1958.

[17] S. Yip. *Handbook of Materials Modeling.* Springer, pp.2307-2323, 2005.

[18] T. Mura. *Micromechanics of Defects in Solids.* Kluwer Academic Publishers, 1987.

[19] J. P. Hirth, J. Lothe. *Theory of Dislocations.* New York: Wiley, 1982.

[20] D. Hull, D. J. Bacon. *Introduction to Dislocations.* Butterworth-Heinemann, 2001.

[21] L. D. Landau, E. M. Lifshitz. *Theory of Elasticity.* Elsevier Ltd, 1986.

[22] R. E Peierls. *The Size of a Dislocation.* Proc. Phys. Soc., Vol.52: 34-37, 1940.

[23] F. R. N. Nabarro. *Dislocations in a Simple Cubic Lattice.* Proc. Phys. Soc., Vol.59: 256-272, 1947.

[24] H. C. Huang, G. H. Gilmer, T. D. de la Rubia. *An Atomistic Simulator for Thin Film Deposition in Three Dimensions.* Journal of Applied Physics, Vol.84(7): 3636–3649, 1998.

[25] M. Rak, M. Izdebski, and A. Brozi. *Kinetic Monte Carlo Study of Crystal Growth from Solution.* Computer Physics Communications, Vol.138(3): 250-263, 2001.

[26] A. C. Levi, M. Kotrla. *Theory and Simulation of Crystal Growth.* Journal of Physics: Condensed Matter, Vol.9(2): 299-344, 1997.

[27] W. Cai, A. Arsenlis, C. R. Weinberger, V. V. Bulatov. *A Non-Singular Continuum Theory of Dislocations.* Journal of the Mechanics and Physics of Solids, Vol.54(3): 561–587, 2006.

[28] B. Devincre, L. P. Kubin. *Mesoscopic Simulations of Dislocations and Plasticity.* Materials Science and Engineering A, Vol.(234-236): 8-14, 1997.

[29] K. W. Schwarz. *Simulation of Dislocations on the Mesoscopic Scale. I. Methods and Examples.* Journal of Applied Physics, Vol.85(1): 108-119, 1999.

[30] K. W. Schwarz. *Simulation of Dislocations on The Mesoscopic Scale. II. Application to Strainedlayer Relaxation.* Journal of Applied Physics, Vol.85(1): 120-129, 1999.

[31] H. M. Zbib, M. Rhee, J. P. Hirth. *On Plastic Deformation and the Dynamics of 3D Dislocations.* Int. J. Mech. Sci., Vol.40: 113-127, 1998.

[32] M. Rhee, H. M. Zbib, J. P. Hirth, H. Huang, T. de la Rubia. *Models for Long-/Short-range Interactions and Cross Slip in 3D Dislocation Simulation of BCC Single Crystals.* Modelling Simul. Mater. Sci. Eng., Vol.6: 467-492, 1998.

[33] L. P. Kubin, G. Canova, M. Condat, Benoit Devincre, V. Pontikis, Yves Bréchet. *Dislocation Microstructures and Plastic Flow: A 3D Simulation.* Solid State Phenomena Vol. (23- 24): 455-472, 1992.

[34] L. P. Kubin, Benoit Devincre, G.R. Canova, Yves Bréchet. *3D Simulations of Dislocations and Plasticity.* Solid State Phenomena, Vol.(42-43): 217-226, 1995.

[35] D. Rodney, Y. Le Bouar, A. Finel. *Phase Field Methods and Dislocations.* Acta Materialia, Vol.51(1): 17-30, 2003.

[36] Y. U. Wang, Y. M. Jin, A. M. Cutino, A. G. Khachaturyan. *Nanoscale Phase Field Microelasticity Theory of Dislocations: Model and 3D Simulations.* Acta Mater. Vol.49: 1847-1857, 2001.

[37] S. Y. Hu, Y. L. Li, Y. X. Zheng, L. Q. Chen. *Effect of Solutes on Dislocation Motion: a Phase Field Simulation.* International Journal of Plasticity, Vol.20: 403-425, 2004.

[38] S. Osher and J. A. Sethian, *Fronts Propagating with Curvature-dependent Speed: Algorithms Based on Hamilton-Jacobi Formulations.* J. Comput. Phys., Vol.79: 12-49, 1988.

[39] J. A. Sethian. *Fast Marching Methods.* SIAM Review, Vol.41: 199-235, 1999.

[40] S. Osher, R. Fedkiw. *Level set Method and Dynamic Implicit Surfaces.* Springer, 2003.

[41] J. A. Sethian. *Evolution, Implementation, and Application of Level Set and Fast Marching Methods for Advancing Fronts.* J. Comput. Phys., Vol.169: 503-555, 2001.

[42] B. Devincre. *Three Dimensional Stress Field Expressions for Straight Dislocation Segments.* Solid State Comm., Vol.93: 875-878, 1995.

[43] J. Glimm, M. J. Graham, J. Grove, X. L. Li. *Front Tracking in Two and Three Dimensions.* Computers Math. Applic., Vol.35: 1-11, 1998.

[44] H. Emmerich. *The Diffuse Interface Approach in Materials Science.* Springer, 2003.

[45] Y. R. Tsai. *Rapid and Accurate Computation of the Distance Function Using Grids.* J. Comput. Phys., Vol.178: 175-795, 2002.

[46] J. A. Sethian. *Level Set Methods and Fast Marching Methods.* Cambridge University Press, 1999.

[47] D. Peng, B. Merriman, S. Osher, H. K. Zhao, M. Kang. *A PDE-Based Fast Local Level Set Method.* J. Comput. Phys., Vol.155: 410-438, 1999.

[48] S. Osher, R. P. Fedkiw. *Level Set Method: An Overview and Some Recent Results.* J. Comput. Phys., Vol.169: 463-502, 2001.

[49] S. Osher, L. T. Cheng, M. Kang, H. Shim, Y. H. Tsai. *Geometric Optics in a Phase-space-based Level Set and Eulerian Framework.* J. Comput. Phys., Vol.179: 622-648, 2002.

[50] P. Burchard, L. T. Cheng, B. Merriman, S. Osher. *Motion of Curves in Three Spatial Dimensions using a Level Set Approach.* J. Comput. Phys., Vol.170: 720-741, 2001.

[51] J. A. Sethian, *Fast Marching Methods.* SIAM Review, Vol.41(2): 199-235, 1999.

[52] J. A. Sethian, A. Vladimirsky. *Fast Methods for the Eikonal and Related Hamilton-Jacobi Equations on Unstructured Mesh.* Proceedings of the National Academy of Sciences, Vol.97: 5699-5703, 2000.

[53] J. A. Sethian. *A Fast Marching Level Set Method for Monotonically Advancing Fronts.* Proc. Nat. Acad. Sci., Vol.93(4): 1591-1595, 1996.

[54] E. Rouy, A. Tourin, *A Viscosity Solutions Approach to Shape-from-shading.* SIAM J. Num. Anal, Vol.29(3): 867-884, 1992.

[55] A. Sedgewick. *Algorithms.* Addison-Wesley, 1988.

[56] D. Adalsteinsson, J. A. Sethian. *A Unified Level Set Approach to Etching, Deposition and Lithography I: Algorithms and Two-dimensional Simulations.* J. Comp. Phys., Vol.120(1): 128-144, 1995.

[57] D. Adalsteinsson, J. A. Sethian. *A Unified Level Set Approach to Etching, Deposition and Lithography II: Three-dimensional Simulations.* J. Comp. Phys., Vol.122(2): 348-366, 1995.

[58] D. Adalsteinsson, J. A. Sethian. *A Unified Level Set Approach to Etching, Deposition and Lithography III: Complex Simulations and Multiple Effects.* J. Comp. Phys., Vol.138(1): 193-223, 1997.

[59] Y. C. Chang, T. Y. Hou, B. Merriman, S. J. Osher. A *Level Set Formulation of Eulerian Interface Capturing Methods for Incompressible Fluid Flows.* J. Comp. Phys., Vol.124: 449-464, 1996.

[60] M. Sussman, P. Smereka, S. J. Osher, A *Level Set Method for Computing Solutions to Imcompressible Two-Phase Flow.* J. Comp. Phys., Vol.114: 146-159, 1994.

[61] H. K. Zhao, T. Chan, B. Merriman, S. J. Osher. A *Variational Level Set Approach to Multiphase Motion.* J. Comp. Phys., Vol.127: 179-195, 1996.

[62] D. Adalsteinsson, J. A. Sethian. *The Fast Construction of Extension Velocities in Level Set Methods.* J. Comp. Phys., Vol.148: 2-22, 1999.

[63] L. C. David. *Another Look at Velocity Extensions in the Level Set Method.* SIAM Journal on Scientific Computing, Vol.31(5): 3255-3273, 2009.

[64] L. C. David. *Some Improvements of the Fast Marching Method.* SIAM J. Sci. Comput., Vol.23(1): 230-244, 2001.

[65] K. W. Morton, D. F. Mayers. *Numerical Solution of Partial Differential Equations.* Cambridge University Press, 2005.

[66] J. W. Thomas. *Numerical Partial Differential Equations.* Springer, 1995.

[67] R. J. LeVeque. *Finite Difference Methods for ODEs and PDEs.* SIAM, 2007.

[68] X. D. Liu, S. Osher, T. Chan. *Weighted Essentially Non-oscillatory Schemes.* J. Comput. Phys., Vol.115: 200-212, 1994.

[69] G. S. Jiang, C. W. Shu, *Efficient Inplementation of Weighted ENO Schemes.* J. Comput. Phys., Vol.126: 202-228, 1996.

[70] G. S. Jiang, D. Peng. *Weighted ENO Schemes for Hamilton Jacobi Equations.* SIAM J. Sci. Comput., Vol.21: 2126-2143, 2000.

[71] G. S. Jiang, D. Levy, C. T. Lin, S. Osher, E. Tadmor. *High-resolution Nonoscillatory Central Schemes with Nonstaggered Grids for Hyperbolic Conservation Laws.* SIAM J. Numer. Anal., Vol.35: 2147-2168, 1998.

[72] T. Y. Hou, Z. L. Li, S. Osher, H. K. Zhao. *A Hybrid Method for Moving Interface Problems with Application to the Hele-Shaw Flow.* J. Comput. Phys., Vol.134: 236-252, 1997.

[73] S. Chen, B. Merriman, S. Osher, P. Smereka. *A Simple Level Set Method for Solving Stefan Problems.* J. Comput. Phys., Vol.135:8-29, 1997.

[74] S. J. Ruuth, B. Merriman, J. Xin, S. Osher. *Diffusion-generated Motion by Mean Curvature for Filaments.* J. Nonlinear Sci., Vol.11: 473-493, 2001.

[75] Y. Xiang, L. T. Cheng, D. J. Srolovitz, E. Weinan. *A Level Set Method for Dislocation Dynamics.* Acta Mater., Vol.51: 5499-5518, 2003.

[76] W. Cai, V. V. Bulatob, J. P. Chang, J. Li, S. *Periodic Image Effects in Dislocation Modelling.* Yip. Phil. Mag., Vol.83: 539-567, 2003.

[77] C. R. Weinberger, W. Cai. *Computing Image Stress in An Elastic Cylinder.* J. Mech. Phy. Solid, Vol.55: 2027-2054, 2007.

[78] Y. Xiang, D. J. Scrolovitz, L. T. Cheng, E. Weinan. *Level Set Simulations of Dislocation-Partical Bypass Mechanisms.* Acta Mater., Vol.52: 1745-1760, 2004.

[79] S. S. Quek, Y. Xiang, Y. W. Zhang, D. J. Srolovitz, C. Lu. *Level Set Simulation of Dislocation Dynamics in Thin Films.* Acta Mater., Vol.54: 2371-2381, 2006.

[80] D. Adalsteinsson, J. A. Sethian. *The Fast Construction of Extension Velocities in Level Set Method.* J. Comput. Phys., Vol.148: 2-22, 1999.

[81] D. Adalsteinsson. J. A. Sethian. *A Fast Level Set Method for Propagating Interfaces.* J. Comput. Phys., Vol.118: 269-277, 1995.

[82] C. Rhee, L. Talbot, J. A. Sethian. *Dynamical Study of a Premixed V Flame*. J. Fluid Mech., Vol.300: 87-115, 1995.

[83] R. Malladi, J.A. Sethian, *Image Processing via Level Set Curvature Flow*. Proc. Natl. Acad. Sci., Vol.92(15): 7046-7050, 1995.

[84] J. A. Sethian, J. D. Strain. *Crystal Growth and Dendritic Solidification*. J. Comput. Phys., Vol.98: 231-253, 1992.

[85] H. K. Zhao, *A Fast Sweeping Method for Eikonal Equations*. Methematics of Computation, Vol.74: 603-627, 2004.

[86] Y. R. Tsai, L. T. Cheng, S. Osher, H. K. Zhao. *Fast Sweeping Algorithms for a Class of Hamilton-Jacobi Equations*. SIAM J. Numeri. Anal., Vol.41: 673-694, 2003.

[87] H. T. Zhang, H. K. Zhao, J. L. Qian. *High Order Fast Sweeping Methods for Static Hamilton-Jacobi Equations*. Journal of scientific computing, Vol.29: 2006.

[88] R. W. Lardner. *Mathematical Theory of Dislocations and Fracture*. Toronto and Buffalo: University of Toronto press, 1974.

[89] A. N. Stroh. *Constrictions and Jogs in Extended Dislocations*. Proc. Phys. Soc. B, Vol.67: 427-436, 1954.

[90] P. B. Hirsch. *Extended Jogs in Dislocations in Face-centred Cubic Metals*. Phil. Mag., Vol.7: 67-93, 1962.

[91] D. H. Avery and W. A. Backofen. Trans. Met. Soc. AI ME, Vol.227: 835, 1963.

[92] G. Schoeck, A. Seeger. *Report of the Conference on Defects in Solids*. Physical Society, London, pp.340, 1955.

[93] J. J. Gilman, *Micromechanics of Flows in Solids*. McGraw-Hill, 1969.

[94] P. J. Jackson. *The Role of Cross-slip in the Plastic Deformation of Crystals*. Mater. Sci. Eng., Vol.57: 39-47, 1983.

[95] L. T. Cheng, *The Level Set Method Applied to Geometrically Based Motion, Materials Science, and Image Processing* (Doctoral Dissertation of UCLA), pp.30-88, 2000.

[96] J. Pan, Y. Shibutani. *Internal Stress Field of Double Cross-slip using Level Set Dislocation Dynamics*. Journal of Solid Mechanics and Material Engineering, Vol.6: 61-70, 2012.

[97] S. S. Quek, Y. W. Zhang, Y. Xiang, D. J. Srolovitz. *Dislocation Cross-slip in Heteroepitaxial Multilayer Films*. Acta Materialia, Vol.58: 226-234, 2010.

[98] S. S. Quek, Y. Xiang, D. J. Srolovitz. *Loss of Interface Coherency around a Misfitting Spherical Inclusion*. Acta Materialia, Vol.59: 5398-5410, 2011.

[99] Z. Chen, T. C. Kevin, D. J. Srolovitz, J. M. Rickman, M. P. Haataja1. *Dislocation Climb Strengthening in Systems with Immobile Obstacles: Three-Dimensional Level-Set Simulation Study*. Phy. Rev. B, Vol.81(054104): 1-12, 2010.

[100] D. Kuhlmann-Wilsdorf. *Origin of Dislocations*. Phil. Mag. Vol.3: 125-139, 1958.

[101] J. C. M. Li. *Dislocation Sources Dislocation Modeling of Physical System*. Pergamon, 1981.

[102] T. Tsuru, Y. Shibutani. *Initial Yield Process around a Spherical Inclusion in Single- Crystalline Aluminium*. Journal of Physics D, Vol.40: 2183-2188, 2007.

[103] J. D. Eshelby. *Solid State Physics*. New York: Academic Press, 1956.

[104] P. Veyssiere. *Formation of Prismatic Loop Alignments in Crystals Deformed in Single Slip*. Phi. Mag. Lett., Vol. 81(12): 795-801. 2001.

[105] P. Veyssiere. T*he Annihilation by Glide of Prismatic Loops in Walls*. Phi. Mag. Lett., Vol. 81(11): 733-741, 2001.

[106] P. Smereka, *Spiral Crystal Growth*. Physica D, Vol.138: 282-301, 2000.

Acknowledgements

First I should thank my supervisor and mentor Prof. Shibutani without whose kindly help and patient guidance this thesis could not be fulfilled. Discussing with Prof. Tarumi about the Micromechanics and Elasticity theory facilitated comprehending dislocation theory. Prof. Matsunaka's detailed instructions are also very grateful for me.

Dr. Wakeda, my tutor, told me Japanese culture and helped me releasing the pressures living in a foreign country. The discussions with Dr. Tanaka are great helps for understanding the methodology of Level Set Method, for which I should be very thankful. Even now he's still concerning about my research during his busy teaching and researching time. Dr. Hiroutsi's generous advices and plentiful knowledge are impetuses for me to keep on doing research.

I own my special thanks to Prof. Li-Tien Cheng in UCSD and Dr. Siu Sin Quek in Institute of High Performance Computing, both of who are professional in level set method. Without their specific and comprehensive explanations, I could not solve the Visualization problem and may not acquire a further understanding and knowledge of this theory. Their efforts deserve my highly appreciation.

At last, I should thank my mom and dad who are supporting me mentally all the time and dedicating their efforts to me as much as they can.

Jun Pan

Suita, Osaka
May, 2012

List of Publications

1. Jun Pan, Yoji Shibutani. *Internal Stress Field of Double Cross-slip using Level Set Dislocation Dynamics*. Journal of Solid Mechanics and Materials Engineering, Vol.6: 61-70, 2012.
2. Jun Pan, Yoji Shibutani. *Formation of Prismatic Dislocation Loop Formation around a Spherical Inclusion using Level Set Dislocation Dynamics*. Journal of Solid Mechanics and Materials Engineering, Vol.6, No.8, 2012.

Conference

1. Jun Pan, Yoji Shibutani. *Cross Slip Descriptions using Level Set Dislocation Dynamics*, JSME 23rd Computational Mechanics Division Conference, Sep. 23-25, 2010.
2. Jun Pan, Yoji Shibutani. *Internal Stress Field of Heterogeneous Defect Interactions using Level Set Dislocation Dynamics*, International Symposium on Atomistic Modeling for Mechanics and Multiphysics of Materials (ISAM4), July 20-22, 2011.
3. Jun Pan, Yoji Shibutani. *Prismatic Dislocation Loop Formation by Level Set Dislocation Dynamics*, JSME 25rd Computational Mechanics Division Conference, Oct. 6-9, 2012.